

**Polymer-mediated solubility enhancement and supersaturation
stabilization using various hydroxypropyl cellulose grades within
amorphous solid dispersions**

Dissertation
zur
Erlangung des Doktorgrades (Dr. rer. nat.)
der
Mathematisch-Naturwissenschaftlichen Fakultät
der
Rheinischen Friedrich-Wilhelms-Universität Bonn

vorgelegt von
Florian Pöstges
aus
Hamburg

Bonn 2024

Angefertigt mit Genehmigung der Mathematisch-Naturwissenschaftlichen Fakultät
der Rheinischen Friedrich-Wilhelms-Universität Bonn

1. Gutachter: Prof. Dr. Karl G. Wagner
2. Gutachter: Prof. Dr. Alf Lamprecht

Tag der Promotion: 13.05.2024

Erscheinungsjahr: 2024

Abstract

Solubility enhancement in combination with supersaturation stabilization of poorly soluble drugs is a well-established concept to enhance oral bioavailability. One promising formulation principle to overcome low solubility issues represents the preparation of amorphous solid dispersions (ASDs). With the aid of a polymer, metastable supersaturated drug solutions are generated upon dissolution, that need to be stabilized for a sufficient dissolution time to prevent precipitation towards the equilibrium solubility of the drug.

As both generation and stabilization of supersaturated drug solutions highly depend on specific drug-polymer interactions in liquid-state, a supersaturation assay in pH 6.8 medium for evaluation of the precipitating effects of various polymers on eight drugs was performed, initially. The results revealed that successful drug supersaturation varied and depended on the individually selected drug-polymer system. As single polymers were not always capable of enabling satisfying precipitation inhibition, polymer mixtures of Eudragit® L 100-55 (EL 100-55) and hydroxypropyl cellulose (HPC)-SSL (50:50) were tested. Synergistic interactions between the polymers led to pronounced enhanced supersaturation of celecoxib (CXB), efavirenz (EFV), and clotrimazole (CLT). Using CXB, the liquid-state polymer-polymer interactions of EL 100-55 and HPC were further investigated, by varying the HPC grade (-L, -SSL, -UL) and the polymer mass ratios.

Before designing ASD formulations, the impact of the manufacturing method on polymer mixing and polymer-polymer interactions of EL 100-55: HPC-SSL (50:50) and EL 100-55: HPC-UL (50:50) were investigated via differential scanning calorimetry (DSC), confocal Raman spectroscopy (CRS), and Fourier-transform infrared spectroscopy (FT-IR). While spray-drying (SD) and hot-melt extrusion (HME) led to homogeneous placebos with pronounced interactions, phase separated formulations with weaker interactions were obtained after vacuum compression molding (VCM). However, the lower melt viscosity of HPC-UL compared to HPC-SSL during the VCM melting process enabled higher content of partially miscible phases between EL 100-55 and HPC-UL. By processing the EL 100-55: HPC polymer mixtures with either CXB or EFV for ternary ASDs, homogeneous embedding was observed after HME and SD. In case of the phase separated ternary VCM ASDs, higher kinetic solid-state solubilities of the drugs within the HPC polymers led to preferred drug distribution within the HPC-rich phases. Since homogeneously mixed polymer phases

Abstract

were necessary for optimal dissolution performances, the single-phased ternary ASDs consisting of extruded EL 100-55: HPC-SSL outperformed the heterogeneous ternary ASDs that were solely prepared via VCM. However, the higher content of partially miscible phases within the ternary EL 100-55: HPC-UL VCM ASDs led to no (CXB) or only small differences (EFV) in dissolution compared to the extruded polymer ASDs.

List of publications

Parts of this work have been submitted and published as peer-reviewed research articles or as abstracts for poster presentation. These research articles were published as open access articles under the terms of the Creative Commons Attribution 4.0 International License.

Research articles

- Pöstges, F.; Kayser, K.; Stoyanov, E.; Wagner, K.G. Boost of Solubility and Supersaturation of Celecoxib via Synergistic Interactions of Methacrylic Acid-Ethyl Acrylate Copolymer (1:1) and Hydroxypropyl Cellulose in Ternary Amorphous Solid Dispersions. *Int J Pharm. X* 2022, 4, 100115, doi:10.1016/j.ijpx.2022.100115.
- Pöstges, F.; Lenhart, J.; Stoyanov, E.; Lunter, D.J.; Wagner, K.G. Phase Homogeneity in Ternary Amorphous Solid Dispersions and Its Impact on Solubility, Dissolution and Supersaturation – Influence of Processing and Hydroxypropyl Cellulose Grade. *Int. J. Pharm. X* 2023, 6, 100222, doi:10.1016/j.ijpx.2023.100222.

Conference abstracts for poster presentation.

- Pöstges, F.; Stoyanov, E.; Wagner, K.G. Boost of Solubility and Supersaturation of Celecoxib via Synergistic Interactions of Eudragit L and Hydroxypropyl Cellulose in Ternary Amorphous Solid Dispersions. 13th Pharmaceuticals, Biopharmaceutics and Pharmaceutical Technology World Meeting, 28-31 March 2022, Rotterdam, The Netherlands.
- Pöstges, F.; Stoyanov, E.; Wagner, K.G. Impact of Manufacturing Processes of Supersaturation Optimized Ternary Amorphous Solid Dispersions on Solid State and Dissolution Performance. AAPS PharmSci 360, 16-19 October 2022, Boston, MA, USA.
- Pöstges, F.; Lenhart, J.; Lunter, D.J.; Stoyanov, E.; Wagner, K.G. Investigation of a ternary amorphous solid dispersion via confocal Raman spectroscopy: Where is the drug?. AAPS PharmSci 360, 22-25 October 2023, Orlando, FL, USA.

Additionally, further research articles of the thesis author (Co-author and first author) were published as peer-reviewed research articles which data and experiments are not content of this thesis.

Research articles (no content of this thesis):

- López Mármol, Á.; Denninger, A.; Touzet, A.; Dauer, K.; Becker, T.; Pöstges, F.; Pellequer, Y.; Lamprecht, A.; Wagner, K.G. The Relevance of Supersaturation and Solubilization in the Gastrointestinal Tract for Oral Bioavailability: An in Vitro vs. in Vivo Approach. *Int. J. Pharm.* 2021, 603, 120648, doi:10.1016/j.ijpharm.2021.120648
- Pöstges, F.; Kayser, K.; Appelhaus, J.; Monschke, M.; Gütschow, M.; Steinebach, C.; Wagner, K.G. Solubility Enhanced Formulation Approaches to Overcome Oral Delivery Obstacles of PROTACs. *Pharmaceutics* 2023, 15, 156, doi:10.3390/pharmaceutics15010156.

Acknowledgments

I would like to express my sincere gratitude to my doctoral father Prof. Dr. Karl G. Wagner for giving me the opportunity to conduct my PhD in his workgroup. I am very thankful for his consistent support and great scientific input during the entire time of my doctorate.

I would also like to thank Prof. Dr. Alf Lamprecht for his written report on my doctoral thesis, and Prof. Dr. Günther Weindl and Prof. Dr. Robert Glaum for their kind acceptance to complete my examination committee.

Especially, I would like to thank Nippon Soda GmbH for funding and supporting my doctoral research project. I had the great pleasure of collaborating with Dr. Edmont Stoyanov from Nisso Chemical Europe GmbH, who not only organized financial and material support, but also enabled a very personal and supportive exchange.

I would like to acknowledge Prof. Dr. Dominique J. Lunter for giving me the opportunity to perform experiments with the confocal Raman microscope in her workgroup at the University of Tübingen. In this context, I would also like to thank her PhD student, Jonas Lenhart, for his help in investigating and analyzing the Raman samples.

I would like to acknowledge Kevin Kayser for his support in my first publication by teaching me the process of hot-melt extrusion.

I would like to express my acknowledgment to Prof. Dr. Michael Gütschow and Dr. Christian Steinebach for the excellent in-house cooperation in the development of supersaturating formulations of PROTACs.

Many thanks to Dr. Marius Monschke for his support and motivation in my first year as PhD student, and for sharing his valuable knowledge and expertise about supersaturating formulations.

Of course, I would like to thank all my colleagues from the Department of Pharmaceutics who accompanied me during the last years. The exchange enabled different perspectives and solution approaches to overcome scientific issues. However, especially the private talks and joint activities ensured that the PhD time was an unforgettable experience that

Acknowledgments

I never would like to miss. My special thanks goes to my office crew, Tim Becker, Katharina Dauer, and Karla Viehmeister who became close friends. The short coffee and sport breaks enriched every single day.

At the end, I would like to express my greatest gratitude to Katja and my family, who have always been by my side, celebrating the successful moments and supporting me unconditionally in difficult times.

Table of content

Abstract	I
List of publications	III
Acknowledgments	V
Table of content	VII
List of abbreviations	IX
List of figures	XI
List of tables	XVII
1. General introduction	1
1.1. Challenges in oral drug formulation	1
1.2. The concept of amorphous solid dispersions	2
1.3. Preparation methods of amorphous solid dispersions.....	2
1.3.1. Heat-based preparation methods.....	3
1.3.2. Solvent-based preparation methods	4
2. Evaluation of polymer-mediated supersaturation and precipitation inhibition of poorly soluble drugs	6
2.1. Introduction	6
2.2. Supersaturation screening of various drugs dependent on pre-dissolved polymers	9
2.3. Supersaturation screening of various drugs dependent on pre-dissolved polymer mixtures, comprising Eudragit® L 100-55 and hydroxypropyl cellulose-SSL (50:50).....	22
2.4. Conclusion.....	28
3. Enhancement of supersaturation performance of celecoxib using polymer combinations of Eudragit® L 100-55 and hydroxypropyl cellulose	29
3.1. Introduction	29
3.2. The influence of different hydroxypropyl cellulose grades and polymer ratios with Eudragit® L 100-55 on celecoxib supersaturation.....	31
3.3. Conclusion.....	36
4. Impact of the manufacturing method on the solid-state of polymer placebo mixtures, comprising Eudragit® L 100-55 and hydroxypropyl cellulose	37
4.1. Introduction	37
4.2. Assessment of thermal stability of the polymers for the heat-based preparation methods	40
4.3. Investigation of manufacturing-dependent polymer mixing.....	41
4.4. Investigation of manufacturing-dependent polymer-polymer interactions.....	50
4.5. Conclusion.....	53

5. Interactions between Eudragit® L 100-55 and hydroxypropyl cellulose in solid-state and dissolution of ternary amorphous solid dispersions using celecoxib and efavirenz as model drugs	54
5.1. Introduction	54
5.2. Solid-state characterization of neat drugs prior to amorphous solid dispersions processing	57
5.3. Solid-state characterization of celecoxib and efavirenz amorphous solid dispersions in terms of amorphousness, homogeneity, and drug-polymer interactions	60
5.4. Mechanistical investigation of drug distribution of celecoxib and efavirenz in ternary vacuum compression molded amorphous solid dispersions	78
5.5. Non-sink dissolution testing of heat-based processed amorphous solid dispersions for evaluating the synergistic interactions between Eudragit® L 100-55 and hydroxypropyl cellulose on solubility enhancement and supersaturation of celecoxib and efavirenz	89
5.6. Non-sink dissolution testing of spray-dried ternary amorphous solid dispersions	99
5.7. Conclusion	102
6. Materials and methods	103
6.1. Materials	103
6.1.1. Drug substances	103
6.1.2. Polymer substances	105
6.1.3. Additional chemical substances	107
6.2. Supersaturation assay as fast-screening method	108
6.3. Supersaturation assay using the MiniDissolution apparatus	109
6.4. Preparation of formulations via hot-melt extrusion (HME)	110
6.5. Preparation of formulations via vacuum compression molding (VCM)	110
6.6. Preparation of formulations via spray-drying (SD)	111
6.7. Thermogravimetric analysis (TGA)	111
6.8. Differential scanning calorimetry (DSC)	111
6.9. Confocal Raman spectroscopy (CRS)	112
6.10. Melt rheology of neat polymers	113
6.11. Fourier-transform infrared spectroscopy (FT-IR)	113
6.12. X-Ray powder diffraction (XRPD)	113
6.13. Non-sink dissolution study	114
6.14. Laser diffraction analysis	114
7. Summary and outlook	115
References	118

List of abbreviations

Abbreviation	Definition
ASD	Amorphous solid dispersion
BCS	Biopharmaceutics classification system
CLT	Clotrimazole
CRS	Confocal Raman spectroscopy
CXB	Celecoxib
DMSO	Dimethyl sulfoxide
DNZ	Danazol
DS	Average number of substituent groups per monomer unit
DSC	Differential scanning calorimetry
EFV	Efavirenz
EL 100-55	Eudragit® L 100-55
EPO	Eudragit® EPO
FEN	Fenofibrate
FT-IR	Fourier-transform infrared spectroscopy
HME	Hot-melt extrusion
HPC	Hydroxypropyl cellulose
HPMC	Hydroxypropyl methylcellulose
HPMCAS	Hydroxypropyl methylcellulose acetate succinate
KTZ	Ketoconazole
LPV	Lopinavir
MS	Moles of substituent combined
MW	Molecular weight
PES	Polyethersulfone
PM	Physical mixture
PVA	Polyvinyl alcohol
PVP	Polyvinylpyrrolidone
SD	Spray-drying
TDL	Tadalafil
T _g	Glass transition temperature

List of abbreviations

TGA	Thermogravimetric analysis
T _m	Melting temperature
VA 64	Kollidon® VA 64
VCM	Vacuum compression molding
XRPD	X-Ray powder diffraction

List of figures

Figure 1: Supersaturation assay of 0.2 mg/mL (=100%) ketoconazole (KTZ) in pH 6.8 medium (0.05 M phosphate buffer) at 37 °C in presence of 1.25 mg/mL pre-dissolved single polymers and without polymer.	10
Figure 2: Supersaturation assay of 0.2 mg/mL (=100%) danazol (DNZ) in pH 6.8 medium (0.05 M phosphate buffer) at 37 °C in presence of 1.25 mg/mL pre-dissolved single polymers and without polymer. In case of very low solubilities, concentrations cannot be displayed in this figure and the reader is referred to Table 3.	11
Figure 3: Supersaturation assay of 0.2 mg/mL (=100%) fenofibrate (FEN) in pH 6.8 medium (0.05 M phosphate buffer) at 37 °C in presence of 1.25 mg/mL pre-dissolved single polymers and without polymer. In case of very low solubilities, concentrations cannot be displayed in this figure and the reader is referred to Table 4.	12
Figure 4: Supersaturation assay of 0.2 mg/mL (=100%) tadalafil (TDL) in pH 6.8 medium (0.05 M phosphate buffer) at 37 °C in presence of 1.25 mg/mL pre-dissolved single polymers and without polymer. In case of very low solubilities, concentrations cannot be displayed in this figure and the reader is referred to Table 5.	13
Figure 5: Supersaturation assay of 0.2 mg/mL (=100%) celecoxib (CXB) in pH 6.8 medium (0.05 M phosphate buffer) at 37 °C in presence of 1.25 mg/mL pre-dissolved single polymers and without polymer. In case of very low solubilities, concentrations cannot be displayed in this figure and the reader is referred to Table 6.	15
Figure 6: Supersaturation assay of 0.2 mg/mL (=100%) efavirenz (EFV) in pH 6.8 medium (0.05 M phosphate buffer) at 37 °C in presence of 1.25 mg/mL pre-dissolved single polymers and without polymer.	16
Figure 7: Supersaturation assay of 0.2 mg/mL (=100%) clotrimazole (CLT) in pH 6.8 medium (0.05 M phosphate buffer) at 37 °C in presence of 1.25 mg/mL pre-dissolved single polymers and without polymer. In case of very low solubilities, concentrations cannot be displayed in this figure and the reader is referred to Table 8.	18
Figure 8: Supersaturation assay of 0.2 mg/mL (=100%) lopinavir (LPV) in pH 6.8 medium (0.05 M phosphate buffer) at 37 °C in presence of 1.25 mg/mL pre-dissolved single polymers and without polymer.	19
Figure 9: Supersaturation assay of 0.2 mg/mL (=100%) ketoconazole (KTZ) (A), danazol (DNZ) (B), fenofibrate (FEN) (C), and tadalafil (TDL) (D) in 0.05 M phosphate buffer at pH 6.8, 37 °C, dependent on 1.25 mg/mL pre-dissolved single polymers EL 100-55, HPC-SSL, and the polymer combination EL 100-55: HPC-SSL (50:50). The total polymer concentration in each experiment was 1.25 mg/mL. In case of very low solubilities, concentrations cannot be displayed in this figure and the reader is referred to Table 10.	23
Figure 10: Supersaturation assay of 0.2 mg/mL (=100%) celecoxib (CXB) (A), efavirenz (EFV) (B), clotrimazole (CLT) (C), and lopinavir (LPV) (D) in 0.05 M phosphate buffer at pH 6.8, 37 °C, dependent on 1.25 mg/mL pre-dissolved single polymers EL 100-55, HPC-SSL, and the polymer combination EL 100-55: HPC-SSL (50:50). The total polymer concentration in each experiment was 1.25 mg/mL. In case of very low solubilities, concentrations cannot be displayed in this figure and the reader is referred to Table 10.	25

Figure 11: Potential formation of the selected HPC grades in solution, adapted from Sakamoto and Stoyanov., 2020 [86], licensed under a Creative Commons Attribution 4.0 International License.....	30
Figure 12: Supersaturation assay of 0.2 mg/mL (=100%) celecoxib (CXB) in 0.05 M phosphate buffer at pH 6.8 without pre-dissolved polymers and in presence of 1.25 mg/mL pre-dissolved single polymers. The assay was performed in 20 mL buffer medium at 37 °C and 75 rpm paddle speed. This figure was partially adapted from Pöstges et al., 2022 [83].....	32
Figure 13: Supersaturation assay of 0.2 mg/mL (=100%) celecoxib (CXB) in 0.05 M phosphate buffer at pH 6.8 in presence of 1.25 mg/mL pre-dissolved polymer mixtures, varying the HPC grade (HPC-L, HPC-SSL, and HPC-UL) and the polymer mass ratio: EL 100-55: HPC (75:25) (A), EL 100-55: HPC (50:50) (B) and EL 100-55: HPC (25:75) (C). For every combination the corresponding polymer-polymer mole ratio is given. The assay was performed in 20 mL buffer medium at 37 °C and 75 rpm paddle speed. This figure was partially adapted from Pöstges et al., 2022 [83].	34
Figure 14: Thermogravimetric analysis (TGA) of neat EL 100-55 (A), HPC-SSL (B) and HPC-UL (C). After heating to 160 °C (vacuum compression molding (VCM) processing temperature) with a heating rate of 10 °C/ min, weight loss [%] was determined after 15 min of holding time (VCM processing annealing time).	40
Figure 15: Differential scanning calorimetry (DSC) thermograms (exo up) of the neat polymers and polymer placebo formulations, comprising of EL 100-55 and HPC-SSL (A), and of EL 100-55 and HPC-UL (B). Analyses were conducted in TOPEM- mode with a constant temperature increase of 2 °C/ min from 0 °C to 170 °C. This figure was partially adapted from Pöstges et al., 2022 [83] and Pöstges et al., 2023 [104].	42
Figure 16: Rescaled differential scanning calorimetry (DSC) thermograms (exo up) of EL 100-55: HPC-SSL (VCM) and EL 100-55: HPC-UL (VCM) for highlighting the differences in the solid-state of both formulations. This figure was taken from Pöstges et al., 2023 [104].	43
Figure 17: Single Raman spectra of neat EL 100-55, HPC-SSL, and HPC-UL for identifying characteristic Raman signals for the investigation of the placebo formulations. The utilized wavenumber for detecting the presence of the corresponding substance is presented with an arrow. This figure was adapted from Pöstges et al., 2023 [104].	44
Figure 18: Confocal Raman spectroscopy (CRS) of EL 100-55: HPC-SSL placebo formulations, processed by vacuum compression molding (VCM) (A, B, C) and by hot-melt extrusion (HME) (D, E, F). The intensities at 1730 cm ⁻¹ and 2885 cm ⁻¹ were utilized for detecting the presence of EL 100-55 (red color) and HPC-SSL (blue color), respectively. This figure was taken from Pöstges et al., 2023 [104].	46
Figure 19: Confocal Raman spectroscopy (CRS) of EL 100-55: HPC-UL placebo formulations, processed by vacuum compression molding (VCM) (A, B, C) and by hot-melt extrusion (HME) (D, E, F). The intensities at 1730 cm ⁻¹ and 2885 cm ⁻¹ were utilized for detecting the presence of EL 100-55 (red color) and HPC-UL (blue color), respectively. This figure was taken from Pöstges et al., 2023 [104].	47
Figure 20: Frequency sweeps of the neat polymers EL 100-55, HPC-SSL, and HPC-UL at the vacuum compression molding (VCM) processing temperature of 160 °C. This figure was taken from Pöstges et al., 2023 [104].	49
Figure 21: Fourier-transform infrared (FT-IR) spectra of the placebo formulations EL 100-55: HPC-SSL (50:50), processed via vacuum compression molding (VCM), hot-melt	

extrusion (HME) and spray-drying (SD), in comparison to the corresponding physical mixtures (PMs) and the neat polymers. Framing of specific bands marks region of interests. This figure was partially adapted from Pöstges et al., 2022 [83] and Pöstges et al., 2023 [104].	51
Figure 22: Fourier-transform infrared (FT-IR) spectra of the placebo formulations EL 100-55: HPC-UL (50:50), processed via vacuum compression molding (VCM), hot-melt extrusion (HME) and spray-drying (SD), compared to the corresponding physical mixtures (PMs) and the neat polymers. Framing of specific bands marks region of interests. This figure was partially adapted from Pöstges et al., 2023 [104].	52
Figure 23: X-Ray powder diffraction (XRPD) diffractogram (A) and differential scanning calorimetry (DSC) thermogram (exo up) (B) of neat celecoxib (CXB). Figure A was adapted from Pöstges et al., 2022 [83].	57
Figure 24: X-Ray powder diffraction (XRPD) diffractogram (A) and differential scanning calorimetry (DSC) thermogram (exo up) (B) of neat efavirenz (EFV). This figure was adapted from Pöstges et al., 2023 [104].	58
Figure 25: Thermogravimetric analysis (TGA) of neat celecoxib (CXB) (A) and neat efavirenz (EFV) (B). After heating to 160 °C (vacuum compression molding (VCM) processing temperature) with a heating rate of 10 °C/ min, weight loss [%] was determined after 15 min of holding time (VCM processing annealing time).	59
Figure 26: X-Ray powder diffraction (XRPD) diffractograms of processed celecoxib (CXB) ASDs (10% drug load): Binary and ternary ASDs, using EL 100-55 and/ or HPC-SSL as ASD-forming polymers (A); binary and ternary ASDs, using EL 100-55 and/ or HPC-UL as ASD-forming polymers (B). Figure A was partially adapted from Pöstges et al., 2022 [83].	61
Figure 27: X-Ray powder diffraction (XRPD) diffractograms of processed efavirenz (EFV) ASDs (10% drug load): Binary and ternary ASDs, using EL 100-55 and/ or HPC-SSL as ASD-forming polymers (A); binary and ternary ASDs, using EL 100-55 and/ or HPC-UL as ASD-forming polymers (B). This figure was partially adapted from Pöstges et al., 2023 [104].	62
Figure 28: Differential scanning calorimetry (DSC) thermograms (exo up) of processed celecoxib (CXB) ASDs (10% drug load): Binary and ternary ASDs, using EL 100-55 and/ or HPC-SSL as ASD-forming polymers (A); binary and ternary ASDs, using EL 100-55 and/ or HPC-UL as ASD-forming polymers (B). Analyses were conducted in TOPEM- mode with a constant temperature increase of 2 °C/ min from 0 °C to 170 °C. This figure was partially adapted from Pöstges et al., 2022 [83].	65
Figure 29: Rescaled differential scanning calorimetry (DSC) thermograms (exo up) of CXB: EL 100-55: HPC-SSL (VCM) and CXB: EL 100-55: HPC-UL (VCM) for highlighting the differences in the solid-state of both formulations. This figure was partially adapted from Pöstges et al., 2022 [83].	66
Figure 30: Differential scanning calorimetry (DSC) thermograms (exo up) of processed efavirenz (EFV) ASDs (10% drug load): Binary and ternary ASDs, using EL 100-55 and/ or HPC-SSL as ASD-forming polymers (A); binary and ternary ASDs, using EL 100-55 and/ or HPC-UL as ASD-forming polymers (B). Analyses were conducted in TOPEM- mode with a constant temperature increase of 2 °C/ min from 0 °C to 150 °C. This figure was partially adapted from Pöstges et al., 2023 [104].	68
Figure 31: Rescaled differential scanning calorimetry (DSC) thermograms (exo up) of EFV: EL 100-55: HPC-SSL (VCM) and EFV: EL 100-55: HPC-UL (VCM) for highlighting the differences in the solid-state of both formulations. This figure was taken from Pöstges et al., 2023 [104].	69

- Figure 32:** Fourier-transform infrared (FT-IR) spectra of the binary celecoxib (CXB) formulations: CXB: EL 100-55 (A), CXB: HPC-SSL (B) and CXB: HPC-UL (C). The ASDs are compared to neat CXB, the neat polymers and the corresponding physical mixture (PM). Framing of specific bands marks region of interests. This figure was partially adapted from Pöstges et al., 2022 [83]. 71
- Figure 33:** Fourier-transform infrared (FT-IR) spectra of the differently processed ternary celecoxib (CXB) ASDs via vacuum compression molding (VCM), polymer extrudate VCM, hot-melt extrusion (HME), and spray-drying (SD): CXB: EL 100-55: HPC-SSL (A) and CXB: EL 100-55: HPC-UL (B). The ASDs are compared to neat CXB, the corresponding unprocessed polymer mixture EL 100-55: HPC (50:50) and the corresponding physical mixture (PM) CXB: EL 100-55: HPC (10:45:45). Framing of specific bands marks region of interests. This figure was partially adapted from Pöstges et al., 2022 [83]. 73
- Figure 34:** Fourier-transform infrared (FT-IR) spectra of the binary efavirenz (EFV) formulations: EFV: EL 100-55 (A), EFV: HPC-SSL (B) and EFV: HPC-UL (C). The ASDs are compared to neat EFV, the neat polymers and the corresponding physical mixture (PM). Framing of specific bands marks region of interests. This figure was adapted from Pöstges et al., 2023 [104]. 75
- Figure 35:** Fourier-transform infrared (FT-IR) spectra of the differently processed ternary efavirenz (EFV) ASDs via vacuum compression molding (VCM), polymer extrudate VCM, hot-melt extrusion (HME), and spray-drying (SD): EFV: EL 100-55: HPC-SSL (A) and EFV: EL 100-55: HPC-UL (B). The ASDs are compared to neat EFV, the corresponding unprocessed polymer mixture EL 100-55: HPC (50:50) and the corresponding physical mixture (PM) EFV: EL 100-55: HPC (10:45:45). Framing of specific bands marks region of interests. This figure was partially adapted from Pöstges et al., 2023 [104]. 77
- Figure 36:** Single Raman spectra of the neat polymers (A) and drugs (B) for the investigations of the ternary VCM ASDs. The utilized wavenumber for detecting the presence of the corresponding substance is presented with an arrow. The spectra of the polymers are already presented in Figure 17. This figure was partially adapted from Pöstges et al., 2023 [104]. 79
- Figure 37:** Confocal Raman spectroscopy (CRS) of the CXB: EL 100-55: HPC-SSL ASD (VCM), using the intensities of 1730 cm^{-1} and 2885 cm^{-1} for identifying the polymers EL 100-55 (red color) and HPC-SSL (blue color), respectively. The intensity at 1615 cm^{-1} is used for presenting the distribution of CXB (green color). The Raman spectra A, B and C refer to the spots A, B, and C of the Raman images, respectively, and represent examples of the spectral information. 80
- Figure 38:** Confocal Raman spectroscopy (CRS) of the CXB: EL 100-55: HPC-UL ASD (VCM), using the intensities of 1730 cm^{-1} and 2885 cm^{-1} for identifying the polymers EL 100-55 (red color) and HPC-UL (blue color), respectively. The intensity at 1615 cm^{-1} is used for presenting the distribution of CXB (green color). The Raman spectra A, B and C refer to the spots A, B, and C of the Raman images, respectively, and represent examples of the spectral information. 81
- Figure 39:** Confocal Raman spectroscopy (CRS) of the EFV: EL 100-55: HPC-SSL ASD (VCM), using the intensities of 1730 cm^{-1} and 2885 cm^{-1} for identifying the polymers EL 100-55 (red color) and HPC-SSL (blue color), respectively. The intensity at 2250 cm^{-1} is used for presenting the distribution of EFV (green color). The Raman spectra A, B and C refer to the spots A, B, and C of the Raman images, respectively, and represent examples of the spectral information. This figure was taken from Pöstges et al., 2023 [104]. 82

Figure 40: Confocal Raman spectroscopy (CRS) of the EFV: EL 100-55: HPC-UL ASD (VCM), using the intensities of 1730 cm ⁻¹ and 2885 cm ⁻¹ for identifying the polymers EL 100-55 (red color) and HPC-UL (blue color), respectively. The intensity at 2250 cm ⁻¹ is used for presenting the distribution of EFV (green color). The Raman spectra A, B and C refer to the spots A, B, and C of the Raman images, respectively, and represent examples of the spectral information. This figure was taken from Pöstges et al., 2023 [104].	83
Figure 41: Differential scanning calorimetry (DSC) thermograms (exo up) of highly drug loaded CXB: EL 100-55 (A), CXB: HPC-SSL (B) and CXB: HPC-UL (C) ASDs for determining maximum kinetic solid-state solubility of the drug in each single polymer. Measurements were conducted immediately after VCM processing.	85
Figure 42: Differential scanning calorimetry (DSC) thermograms (exo up) of highly drug loaded EFV: EL 100-55 (A), EFV: HPC-SSL (B) and EFV: HPC-UL (C) ASDs for determining maximum kinetic solid-state solubility of the drug in each single polymer. Measurements were conducted immediately after VCM processing. This figure was taken from Pöstges et al., 2023 [104].	86
Figure 43: Non-sink dissolutions of binary celecoxib (CXB) ASDs (10% drug load) of EL 100-55, HPC-SSL, EL 100-55 in presence of 1.8 mg/mL pre-dissolved HPC-SSL, processed via vacuum compression molding (VCM) (A) and ternary CXB ASDs (10% drug load), comprising of EL 100-55: HPC-SSL (50:50), processed via hot-melt extrusion (HME) and/or VCM (B). The dissolution was performed in 20 mL pH 6.8 medium (0.05 M phosphate buffer) at 37 °C and 75 rpm paddle speed. This figure was partially adapted from Pöstges et al., 2022 [83].	91
Figure 44: Non-sink dissolutions of binary celecoxib (CXB) ASDs (10% drug load) of EL 100-55, HPC-UL, EL 100-55 in presence of 1.8 mg/mL pre-dissolved HPC-UL, processed via vacuum compression molding (VCM) (A) and ternary CXB ASDs (10% drug load), comprising of EL 100-55: HPC-UL (50:50), processed via hot-melt extrusion (HME) and/or VCM (B). The dissolution was performed in 20 mL pH 6.8 medium (0.05 M phosphate buffer) at 37 °C and 75 rpm paddle speed. Figure A was partially adapted from Pöstges et al., 2022 [83].	93
Figure 45: Non-sink dissolutions of binary efavirenz (EFV) ASDs (10% drug load) of EL 100-55, HPC-SSL, EL 100-55 in presence of 1.8 mg/mL pre-dissolved HPC-SSL, processed via vacuum compression molding (VCM) (A) and ternary EFV ASDs (10% drug load), comprising of EL 100-55: HPC-SSL (50:50), processed via hot-melt extrusion (HME) and/or VCM (B). The dissolution was performed in 20 mL pH 6.8 medium (0.05 M phosphate buffer) at 37 °C and 75 rpm paddle speed. This figure was partially adapted from Pöstges et al., 2023 [104].	96
Figure 46: Non-sink dissolutions of binary efavirenz (EFV) ASDs (10% drug load) of EL 100-55, HPC-UL, EL 100-55 in presence of 1.8 mg/mL pre-dissolved HPC-UL, processed via vacuum compression molding (VCM) (A) and ternary EFV ASDs (10% drug load), comprising of EL 100-55: HPC-UL (50:50), processed via hot-melt extrusion (HME) and/or VCM (B). The dissolution was performed in 20 mL pH 6.8 medium (0.05 M phosphate buffer) at 37 °C and 75 rpm paddle speed. This figure was partially adapted from Pöstges et al., 2023 [104].	98
Figure 47: Particle size distribution of ternary spray-dried (SD) ASDs, including the presentation of the respective d ₁₀ , d ₅₀ , d ₉₀ values [µm]: CXB: EL 100-55: HPC-SSL (SD) (A), CXB: EL 100-55: HPC-UL (SD) (B), EFV: EL 100-55: HPC-SSL (SD) (C), EFV: EL 100-55: HPC-UL (SD) (D).	99

Figure 48: Non-sink dissolutions of ternary celecoxib (CXB) ASDs (10% drug load) processed via spray-drying (SD), comprising of EL 100-55 and HPC-SSL (50:50) or EL 100-55 and HPC-UL (50:50). The dissolution was performed in 20 mL pH 6.8 medium (0.05 M phosphate buffer) at 37 °C and 75 rpm paddle speed.100

Figure 49: Non-sink dissolutions of ternary efavirenz (EFV) ASDs (10% drug load) processed via spray-drying (SD), comprising of EL 100-55 and HPC-SSL (50:50) or EL 100-55 and HPC-UL (50:50). The dissolution was performed in 20 mL pH 6.8 medium (0.05 M phosphate buffer) at 37 °C and 75 rpm paddle speed.101

Figure 50: Fixed screw configuration of the twin screw extruder ZE 12 for preparing the HME placebo formulations and the ternary HME ASDs. The conveying elements (grey color) demonstrated 9, 12, and 18 mm pitches. The used kneading elements showed staggering angles of 30° (yellow color), 60° (orange color), and 90° (red color). The temperatures of the segments were selected to be of ambient temperature (segment 1), 40 °C (segment 2), 75 °C (segment 3), 150 °C (segment 4, 5 and 6). This figure was taken from Pöstges et al., 2023 [104].110

List of tables

Table 1: Classification of drugs according to the Biopharmaceutics classification system (BCS) [6].....	1
Table 2: Concentrations of dissolved ketoconazole (KTZ) in 0.05 M phosphate buffer pH 6.8, 37 °C, after 30 min and 60 min, dependent on the pre-dissolved polymer (1.25 mg/mL) and without polymer.....	10
Table 3: Concentrations of dissolved danazol (DNZ) in 0.05 M phosphate buffer pH 6.8, 37 °C, after 30 min and 60 min, dependent on the pre-dissolved polymer (1.25 mg/mL) and without polymer.....	11
Table 4: Concentrations of dissolved fenofibrate (FEN) in 0.05 M phosphate buffer pH 6.8, 37 °C, after 30 min and 60 min, dependent on the pre-dissolved polymer (1.25 mg/mL) and without polymer.....	12
Table 5: Concentrations of dissolved tadalafil (TDL) in 0.05 M phosphate buffer pH 6.8, 37 °C, after 30 min and 60 min, dependent on the pre-dissolved polymer (1.25 mg/mL) and without polymer.....	14
Table 6: Concentrations of dissolved celecoxib (CXB) in 0.05 M phosphate buffer pH 6.8, 37 °C, after 30 min and 60 min, dependent on the pre-dissolved polymer (1.25 mg/mL) and without polymer.....	15
Table 7: Concentrations of dissolved efavirenz (EFV) in 0.05 M phosphate buffer pH 6.8, 37 °C, after 30 min and 60 min, dependent on the pre-dissolved polymer (1.25 mg/mL) and without polymer.....	17
Table 8: Concentrations of dissolved clotrimazole (CLT) in 0.05 M phosphate buffer pH 6.8, 37 °C, after 30 min and 60 min, dependent on the pre-dissolved polymer (1.25 mg/mL) and without polymer.....	18
Table 9: Concentrations of dissolved lopinavir (LPV) in 0.05 M phosphate buffer pH 6.8, 37 °C, after 30 min and 60 min, dependent on the pre-dissolved polymer (1.25 mg/mL) and without polymer.....	19
Table 10: Concentrations of the dissolved drugs after 30 min and 60 min in presence of pre-dissolved EL 100-55, HPC-SSL, and the polymer combination EL 100-55: HPC-SSL (50:50) in 0.05 M phosphate buffer pH 6.8, 37 °C. The total polymer concentration in each experiment was 1.25 mg/mL.	26
Table 11: Physicochemical properties of the investigated HPC grades, including the molecular weights (MWs) [84], the moles of substituent combined (MS), the average number of substituent groups per monomer unit (DS) and the hydroxypropoxy content [%] [77].....	29
Table 12: All investigated polymer combinations, ordered by mole ratio HPC/ EL 100-55 (low -> high): Calculation of mole ratio is based on molecular weights (MWs) of the utilized polymers: EL 100-55 (320,000 g/mol) [85], HPC-L (140,000 g/mol), HPC-SSL (40,000 g/mol), HPC-UL (20,000 g/mol) [84]. C_{max} [%] of EL 100-55: HPC-SSL combinations were obtained from Pöstges et al., 2022 [83].....	35
Table 13: Glass transition temperatures (T_g s) of the neat polymers and all investigated placebo formulations. The values of the T_g s were partially taken from Pöstges et al., 2022 [83] and Pöstges et al., 2023 [104].	43
Table 14: Calculated complex viscosities (Pa*s) at an angular frequency of 1 rad/s for the neat polymers EL 100-55, HPC-SSL, and HPC-UL at the vacuum compression molding	

(VCM) processing temperature of 160 °C. This table was taken from Pöstges et al., 2023 [104].	49
Table 15: Glass transition temperatures (T_g s) of the celecoxib (CXB) ASDs dependent on the selected processing method. The values of the T_g s were partially taken from Pöstges et al., 2022 [83].	64
Table 16: Glass transition temperatures (T_g s) of the efavirenz (EFV) ASDs dependent on the selected processing method. The values of the T_g s were partially taken from Pöstges et al., 2023 [104].	67
Table 17: Overview of highly drug loaded binary ASDs for investigating the kinetic solid-state solubility of the drugs celecoxib (CXB) and efavirenz (EFV) in EL 100-55, HPC-SSL, and HPC-UL. The “X” shows the processed and tested formulations. The green color covers the drug loads that were within the kinetic solid-state solubility, while the color red demonstrates the exceedance of the kinetic solubility. For every tested formulation the detected glass transition temperature (T_g) and melting temperature (T_m) is provided. In case of absence of T_g or T_m the corresponding field is designated with “n/a”. The values of the thermal events of the EFV ASDs were taken from Pöstges et al., 2023 [104].	87
Table 18: Chemical structures, information about the supplier/manufacturer, and relevant physicochemical properties of the investigated drugs. Except the molecular weight (MW), the physicochemical properties refer to predicted values, obtained from DrugBank [130].	103
Table 19: Molecular structures, information about the supplier/ manufacturer, and relevant physicochemical properties of utilized polymers.	105
Table 20: Overview of additional chemical substances that were used for performing the experiments of the thesis.	107
Table 21: Overview of the utilized wavelengths of the drugs for calculation of the dissolved amounts in the supersaturation screening (Chapter 2.).	109

1. General introduction

1.1. Challenges in oral drug formulation

Most drug candidates in early drug discovery and approx. 40% of currently marketed compounds exhibit high hydrophobic molecular structure, leading to poor water solubility [1]. However, the solubility of a drug is a critical factor in obtaining oral exposure, as in most cases the drug must be dissolved to be absorbed and bioavailable. Aside the solubility and dissolution rate, the drug's permeability across biological membranes is decisive for the extent of oral drug absorption [2–4].

The biopharmaceutics classification system (BCS) was implemented to categorize drugs according to the physicochemical properties solubility and permeability and to predict potential limitations in bioavailability. Additional factors that impact bioavailability, as first-pass metabolism or affinity to efflux transports are not considered [5].

Table 1 presents the four classes of the BCS. Drugs, belonging to class I exhibit high solubility and high permeability, thus representing optimal properties for high oral exposure. BCS II drugs demonstrate dissolution rate- limited absorption, as the substances exhibit low solubility, but high permeability. Opposite properties are described for the BCS III drugs (high solubility and poor permeability), leading to permeability-limited bioavailability issues. BCS IV drugs belong to the “worst case” class, as both the solubility and the permeability are low [6]. Consequently, for the drugs that demonstrate limited dissolution rate arising from the poor water solubility (BCS II and BCS IV drugs), several strategies were employed, aiming to increase the solubility or the dissolution rate of the affected drugs [7].

Table 1: Classification of drugs according to the Biopharmaceutics classification system (BCS) [6].

BCS class	Solubility	Permeability
I	High	High
II	Low	High
III	High	Low
IV	Low	Low

1.2. The concept of amorphous solid dispersions

Amorphization is a promising tool to overcome low solubility issues, as amorphous material exhibits higher solubility and faster dissolving compared to the corresponding crystalline molecular composition [8]. In contrast to the crystalline form, dissolving of amorphous material does not require breaking of the crystal lattice structure. This results in enhanced interactions with the solvent molecules and an exceedance of the thermodynamic solubility [9]. Amorphous solids can be obtained by cooling liquids or evaporating solutions, if the procedures occur faster than the reorganization of the molecules into the crystalline state [10]. However, after successful amorphization, the higher chemical potential of the amorphous material implies low physical stability, thus the material tends to recrystallize to the thermodynamic stable form, negating the solubility advantage [11]. In order to prevent rapid recrystallization, the kinetic unstable amorphous form needs to be stabilized by the aid of an inert carrier, mostly a polymer, to form an amorphous solid dispersion (ASD). Stabilization of the amorphous form is enabled via drug-polymer interactions, restricted diffusion of the API molecules by decreasing molecular mobility, and increased energy barrier for crystal nucleation [12–14]. The upper limit of drug load without risk of crystallization is determined by the solid-state solubility of the drug within the polymer matrix. The formulation can be regarded to be stable, as long as the drug content remains below its solubility [15,16]. By exceeding the solid-state solubility, the supersaturated solid polymer solution is only kinetically controlled and the risk of recrystallization and phase separation increases during the storage time [17].

1.3. Preparation methods of amorphous solid dispersions

The aim of all ASD preparation techniques is to convert the drug into the amorphous state and to embed the drug homogeneously into a polymer matrix [18,19]. For enabling the conversion into the amorphous state, the lattice structure of the crystalline drug must be broken via heat or dissolving in a solvent, followed by amorphously embedding of the drug into the matrix via rapid cooling or rapid drying [20]. These manufacturing principles lead to heat-based and solvent-based preparation methods which are presented in the following chapters.

1.3.1. Heat-based preparation methods

Hot-melt extrusion (HME) is one of the most common and popular ASD formulation principle [20]. Simple scale-up and continuous manufacturing make HME attractive for the pharmaceutical industry [21]. As it is a solvent-free preparation method, no additional drying step for removing the residual organic solvent is required [22].

The extrusion process is initiated by feeding the prepared physical mixture (PM) constantly into the actual extruder, which consists of a tempered barrel housing, one or more screws with a defined configuration of conveying elements and kneading elements, and a die for the molten mass to exit the extruder and to cool down rapidly.

To prevent residual crystallinity within the solid dispersion, the processing temperature is often set higher than the melting point of the drug [23], whereby viscous dissipation via the kneading elements allows reduced barrel temperature [24]. In case of melting point depression due to strong interactions between polymer and drug, the extrusion temperature can be further reduced to temperatures below the melting point of the neat drug [25].

Moreover, the selected processing temperatures during the extrusion process must be higher than the glass transition temperature (T_g) or the melting temperature (T_m) of the polymer to realize enough softening of the mass [26]. Otherwise, the melt flow through the barrel is not assured and the drug cannot be embedded homogeneously into the polymer matrix [27].

Consequently, due to the application of heat and shear forces on the molten mass during the process, thermal and mechanical stability of the single components must be assured. In case of polymers, high temperatures and high shearing effects may cause depolymerization of polymer chains and polymer chain breakage, respectively [28]. Thermal degradation with consequence of loss of activity may occur, if too much heat is applied on the drug [26]. Hence, the application of HME is limited to thermal and mechanical stable materials. Aside the thermal and mechanical resistance of the materials, the melt viscosity of the polymer is an additional critical process parameter, as even at temperatures above the T_g too high melt viscosity leads to torque overload of the kneading elements and to an abort of the extrusion process [29]. As most polymers demonstrate reduced viscosity by increasing shear forces or the temperature [16,30], the extrudability can be improved by adapting the processing conditions. Since material

stability do not always allow increasement of temperature and shearing, plasticizers can be utilized which soften the polymer mass by decreasing the T_g and enable lower processing temperatures [31,32].

However, even the small scale extruders require considerable amounts of materials, thus the application is not suitable for new chemical entities, when the drug supply is a cost-intensive and time-consuming factor [33–35]. In order to develop HME based formulation with limited drug quantity, micro- scale (mg-scale) screening tools are desirable. Vacuum compression molding (VCM) was introduced by Treffer et al. and represents a lossless melt-based ASD preparation method, where the molten material is compressed into a solid form under vacuum [36]. The sample size can be chosen, depending on the selected VCM geometry (5 to 25 mm) and on the selected sample height (0.1 to 10 mm), enabling formulations with less than 10 mg. The powdery material is loaded into the sample chamber, completely surrounded by PTFE separation foils. The tool is placed on a pre-heated hot plate, the pressure inside the tool is reduced up to vacuum, and the material is molten for a pre-defined annealing time of 5 to 15 min. Subsequently, the tool is transferred on a cooling plate for enabling rapid solidifying [34,36,37].

In contrast to HME, the VCM process occurs solely under heat, hence no shear forces apply on the molten mass. Therefore, to obtain a homogeneous sample, it is important to have a homogenous starting material in small micrometer range, hence preparation of the PM requires a milling step [34]. Moreover, as the kneading elements in the extruder generate additional heat due to the shear forces, the annealing temperature of the VCM is usually higher to equalize the viscous dissipation [34].

1.3.2. Solvent-based preparation methods

The principle of solvent-based ASD preparation methods bases on rapid evaporation of an organic or aqueous solution in which the polymer and the drug are dissolved, leading to an amorphous product [20]. As the drugs for ASD processing usually reveal low water solubility, the use of organic solvents is required. A common industrial solvent-based preparation method is spray-drying (SD), where the drug- polymer solution is sprayed into fine droplets by the aid of a spraying nozzle into a tempered drying chamber. The generated droplets solidify immediately as a result of rapid removing of the solvent from the liquid droplets [38].

Compared to the melt-based preparation methods, SD enables ASD processing with temperature-sensitive drugs and polymers, as only a minimum heat input is required for evaporating the solvent [39]. Additionally, drugs with very high melting points that are not suitable for HME can be used for ASD preparation [40,41], hence the portfolio of processable drugs is extended. On the other hand, only solutions exhibiting low viscosity are feasible for processing, leading to limited solid load and high consumption of organic solvents [42].

As small amounts of solvent remain in the product after the SD process, a secondary drying of the material is necessary to remove the residual solvent [43]. Nevertheless, for patients and the operator's safety the selected organic solvent should be non-toxic, thus careful selection of the organic solvent must be made prior to the SD process.

2. Evaluation of polymer-mediated supersaturation and precipitation inhibition of poorly soluble drugs

2.1. Introduction

The solubility of a drug is a very important physicochemical property that is determined in the pre-formulation stage, as a solubility issue needs to be considered in the further formulation development [44,45].

The genuine equilibrium solubility describes the maximum quantity of a compound that is dissolved at a given temperature and given pressure in a defined solvent. Thus, the concentration of the drug is saturated and the dissolved particles are in equilibrium with the corresponding solid sediment [46]. With respect to BCS II and BCS IV drugs, oral administration of neat drug leads to high content of undissolved drug particles which are not available for oral exposure [47,48].

As supersaturation is a state where the concentration of the solute exceeds the thermodynamic stable equilibrium solubility of the drug, supersaturating formulations represent promising approaches to increase the absorption flux of poorly soluble drugs [47,49,50]. The degree of supersaturation can be described by the supersaturation factor S :

$$S = \frac{C}{C_{eq}} \quad (\text{Equation 1})$$

whereby C_{eq} is the thermodynamic stable equilibrium solubility and C is the determined supersaturated concentration [51,52].

However, in a supersaturated solution, the solute provides higher free energy than the thermodynamic stable form of the drug in equilibrium. Due to the extent of free energy, the supersaturated state is thermodynamic metastable, thus the solution tends to precipitate towards the equilibrium solubility [53]. Depending on the packing of the solid material, the obtained precipitate provides crystalline or amorphous character [54].

The literature has focused on the description of the crystallization process, however analogous processes occur by amorphous precipitation [55].

The crystallization process is divided into nucleation and crystal growth, whereby both processes generally occur simultaneously. During nucleation, solute molecules form

clusters within the solution. Clusters of insufficient size are not stable and disintegrate, however, after exceeding a critical size, the clusters grow to crystals via diffusion and absorption of solute molecules to energetically favored growth sites [55,56].

However, in order to benefit from supersaturating formulations, preventing nucleation and crystal growth for generating and maintaining the supersaturated state is important. The phenomena of “spring and parachute” describe the optimal progression of supersaturated solutions. The “spring” effect refers to the generation of a supersaturated solution which is mainly attributed to an initial solubility enhancement (e.g., rapid dissolution) and enables the initial prerequisite for supersaturation-driven enhancement of absorption. The further stabilization is described by the “parachute” effect. Without the “parachute” effect, the drug precipitates immediately and the initial effect of solubility enhancement is negated before it even impacts the absorption [57].

Several pharmaceutical excipients are applicable that can act as precipitation inhibitor in order to inhibit nucleation and crystal growth for prolonging the supersaturated state. The precipitation inhibition of polymers are mainly attributed to drug- polymer interactions via hydrogen bonds, polar, or dispersion forces, thus the interactions are highly specific and depend on the molecular structure of both the polymer and the drug [48,53]. Although the mode of precipitation inhibition is assumed to vary with the individual drug polymer system, general assumptions of the potential inhibitory mechanisms are published:

- Adsorption of polymer chains onto the surface of primary nuclei, preventing the formation of crystalline lattice structures [58]
- Reducing nucleation by increasing the cluster-liquid interfacial energy [48]
- Specific interactions between the polymer and the crystal surface forming a mechanical barrier and preventing the introduction of dissolved drugs into the crystal lattice [58,59]
- Eliminating crystal growth spots by interaction with imperfection sites thus flattening the crystal surface [53]
- Increase of viscosity leading to reduced molecular mobility in solution and to delayed induction time of nucleation and crystallization [48,53]

In addition to the reported intermolecular interactions between the various polymers and the drugs, separated amorphous drug colloids, e.g., liquid-liquid phase separation can

occur upon supersaturation that demonstrated to impact the supersaturation performance [60]. The liquid-liquid phase separation describes the separation of the supersaturated solution into a colloidal drug-rich phase, consisting of nanosized amorphous drug species, and into a solvent-rich phase, when the amorphous solubility of a drug is exceeded. The phase-separated colloidal drug phase functions as a drug reservoir and was reported to be responsible for enhanced drug absorption [35,61–63]. Hirlak et al. demonstrated a correlation between the ability of the polymers to stabilize the colloidal phase in terms of size and solid-state, and the ability to stabilize the supersaturated state of the drug [64]. Consequently, polymers which exhibited excellent precipitation inhibition were demonstrated to act as growth inhibitor for the nanosized colloids of the corresponding drugs [65,66].

In order to find the optimal polymer for stabilizing the supersaturated state of an unprocessed drug, so-called supersaturation assays can be performed.

Supersaturation assays investigate the supersaturation behavior of drugs in dependence on various pre-dissolved polymers and can be regarded as preliminary experiments for exploring optimal supersaturation stabilizing polymers before ASD processing [67]. The spring effect of the supersaturation assay is initiated by adding a highly concentrated organic drug solution into the aqueous polymer medium (solvent shift method) [67]. The selected drug dose must be high enough to create pronounced high non-sink conditions for evaluating effectively the impact of precipitation inhibition [68]. Consequently, if the supersaturated state cannot be stabilized, precipitation will occur immediately.

The general purpose of this chapter was to create an overview of the individual supersaturation performance of in total eight drugs in dependence on various commercially available polymers.

To evaluate whether combining polymers would provide synergistic or antagonistic effects on the supersaturation performance of these drugs, the supersaturation testing was extended by investigating the impact of a polymer mixture of Eudragit® L 100-55 (EL 100-55) and hydroxy propyl cellulose (HPC)-SSL (50:50 mass ratio), additionally.

Due to the high number of drug-polymer combinations (eight drugs and eight polymers/polymer combination) it was decided to select two timepoints (30 and 60 min) for the evaluation of the supersaturation performances.

2.2. Supersaturation screening of various drugs dependent on pre-dissolved polymers

The results of the supersaturation assay of each drug in neat 0.05 M phosphate buffer (pH 6.8) and in presence of 1.25 mg/mL pre-dissolved polymers is presented in the Figure 1 - Figure 8 and in the corresponding Table 2 - Table 9. The Y-axis labeling of all figures is chosen from 0-100% of dissolved drug to enable a unified representation among the various drugs. Regarding very small concentrations, the dissolved amounts might be too small to display the results sufficiently. In these cases, the reader is referred to the corresponding table of the figure.

The supersaturation assay of ketoconazole (KTZ) revealed polymer-dependent extent of supersaturation stabilization (Figure 1 and Table 2). Without any polymer, KTZ precipitated within the first 30 min, leading to a concentration of 3.5%. The poly acrylate polymers Eudragit® EPO (EPO) and EL 100-55 were demonstrated to be the most suitable candidates for the stabilization of a supersaturated KTZ solution, as concentrations of 83.0% (EPO) and 69.0% (EL 100-55) were determined after 30 min which did not decrease after 60 min. Using cellulose derivatives the extent of the supersaturated state was clearly reduced. Concentrations of approx. 10% KTZ were obtained after 30 and 60 min utilizing the HPC polymers. The testing with hydroxypropyl methylcellulose acetate succinate (HPMCAS) M revealed time-dependent supersaturation behavior of KTZ within the observation period, as the concentration of 30.2% after 30 min decreased to 18.8% after 60 min. Concentration of 20.0% (30 min) and 14.8% (60 min) were obtained using hydroxypropyl methylcellulose (HPMC) HME 15 LV. Kollidon® VA 64 (VA 64) showed only poor impact on the supersaturated state of KTZ, as concentrations of 8.5% and 7.5% were detected after 30 min and 60 min, respectively.

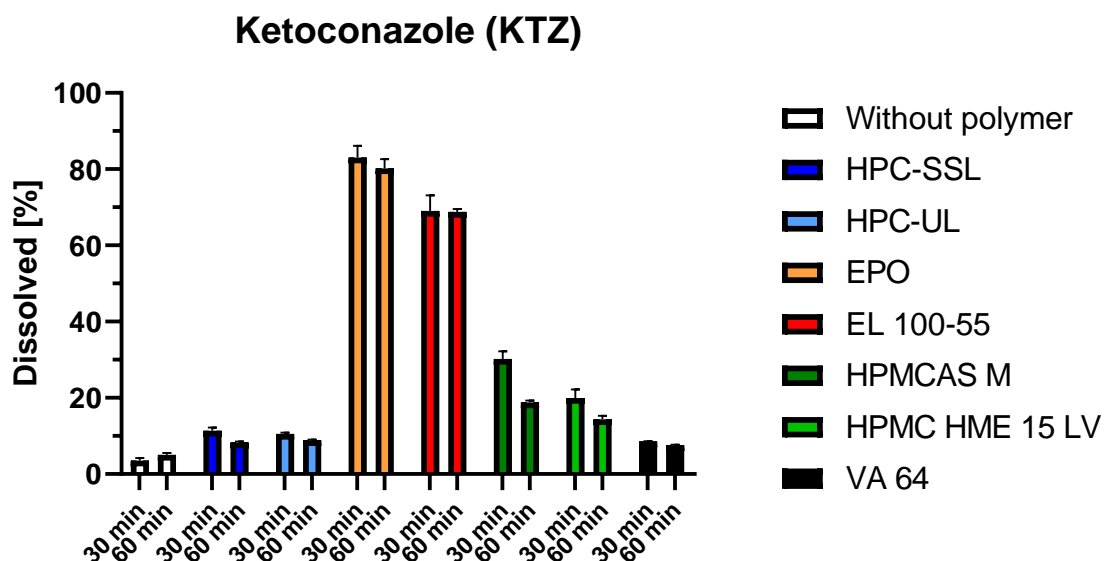


Figure 1: Supersaturation assay of 0.2 mg/mL (=100%) ketoconazole (KTZ) in pH 6.8 medium (0.05 M phosphate buffer) at 37 °C in presence of 1.25 mg/mL pre-dissolved single polymers and without polymer.

Table 2: Concentrations of dissolved ketoconazole (KTZ) in 0.05 M phosphate buffer pH 6.8, 37 °C, after 30 min and 60 min, dependent on the pre-dissolved polymer (1.25 mg/mL) and without polymer.

Polymer	Concentration after	
	30 min [%]	60 min [%]
Without polymer	3.5 ± 0.7	5.1 ± 0.5
HPC-SSL	11.4 ± 0.8	8.3 ± 0.3
HPC-UL	10.5 ± 0.3	8.9 ± 0.1
EPO	83.0 ± 3.1	80.2 ± 2.4
EL 100-55	69.0 ± 4.1	68.8 ± 0.7
HPMCAS M	30.2 ± 2.0	18.8 ± 0.5
HPMC HME 15 LV	20.0 ± 2.3	14.8 ± 0.8
VA 64	8.5 ± 0.1	7.5 ± 0.2

Figure 2 and Table 3 display the supersaturation results of danazol (DNZ). The use of HPC-SSL, HPC-UL, EL 100-55 and VA 64 did not show any decisive improvement on the supersaturation of DNZ after 30 and 60 min compared to the experiment in neat buffer, leading to concentrations of approx. 1%. HPMC AS M was able to maintain 10.6 % of DNZ in solution after 60 min. However, HPMC HME 15 LV and especially EPO seemed to be the

most promising candidates, as final concentrations of 38.9% and 57.3% were determined, respectively.

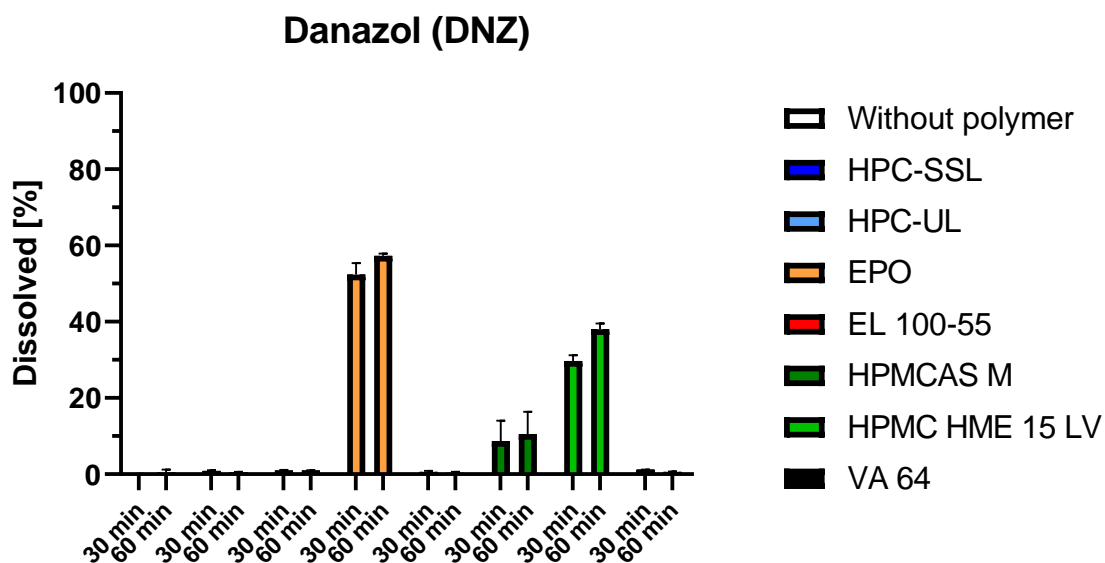


Figure 2: Supersaturation assay of 0.2 mg/mL (=100%) danazol (DNZ) in pH 6.8 medium (0.05 M phosphate buffer) at 37 °C in presence of 1.25 mg/mL pre-dissolved single polymers and without polymer. In case of very low solubilities, concentrations cannot be displayed in this figure and the reader is referred to Table 3.

Table 3: Concentrations of dissolved danazol (DNZ) in 0.05 M phosphate buffer pH 6.8, 37 °C, after 30 min and 60 min, dependent on the pre-dissolved polymer (1.25 mg/mL) and without polymer.

Polymer	Concentration after	
	30 min [%]	60 min [%]
Without polymer	0.1 ± 0.0	0.5 ± 0.7
HPC-SSL	0.8 ± 0.2	0.5 ± 0.1
HPC-UL	1.0 ± 0.2	0.9 ± 0.1
EPO	52.4 ± 3.0	57.3 ± 0.5
EL 100-55	0.6 ± 0.3	0.3 ± 0.3
HPMCAS M	8.7 ± 5.3	10.6 ± 5.8
HPMC HME 15 LV	29.7 ± 1.4	38.9 ± 0.4
VA 64	1.2 ± 0.0	0.63 ± 0.1

Regarding the investigation of fenofibrate (FEN), the pre-dissolved polymers were not capable of maintaining the supersaturated state, as pronounced precipitation within the first 30 min occurred (Figure 3 and Table 4). EPO was representing an exception, as more

than 60 % of FEN was dissolved after 30 min. The supersaturated state was stabilized for at least 60 min with only a slight decrease in concentration, leading to 57.1% of dissolved FEN.

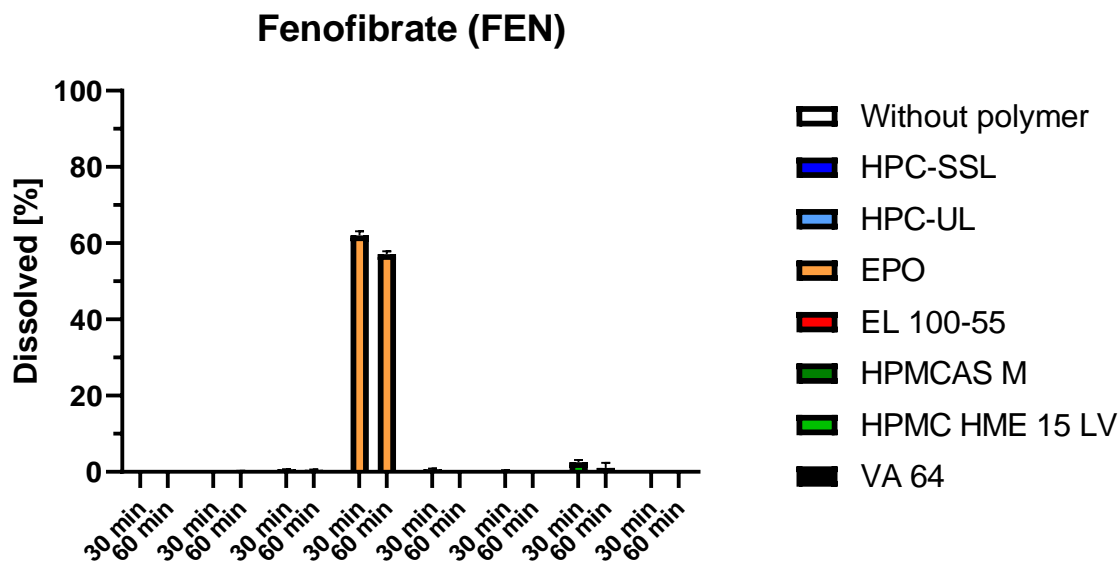


Figure 3: Supersaturation assay of 0.2 mg/mL (=100%) fenofibrate (FEN) in pH 6.8 medium (0.05 M phosphate buffer) at 37 °C in presence of 1.25 mg/mL pre-dissolved single polymers and without polymer. In case of very low solubilities, concentrations cannot be displayed in this figure and the reader is referred to Table 4.

Table 4: Concentrations of dissolved fenofibrate (FEN) in 0.05 M phosphate buffer pH 6.8, 37 °C, after 30 min and 60 min, dependent on the pre-dissolved polymer (1.25 mg/mL) and without polymer.

Polymer	Concentration after	
	30 min [%]	60 min [%]
Without polymer	n/a	n/a
HPC-SSL	0.2 ± 0.0	0.3 ± 0.0
HPC-UL	0.7 ± 0.1	0.5 ± 0.1
EPO	62.1 ± 1.1	57.1 ± 0.7
EL 100-55	0.7 ± 0.2	n/a
HPMCAS M	0.4 ± 0.1	n/a
HPMC HME 15 LV	2.6 ± 0.5	1.1 ± 1.3
VA 64	0.2 ± 0.0	0.1 ± 0.0

Figure 4 and Table 5 reveal the supersaturation assay of tadalafil (TDL). By pre-dissolving HPC-SSL and HPC-UL 26.0% and 20.7% of dissolved TDL were determined after 30 min, respectively. These concentrations plummeted to approx. 10% after 60 min, indicating the inability of the HPC polymers of maintaining a supersaturated solution of TDL for more than one hour. The alternative cellulose derivates HPMCAS M and HPMC HME 15 LV demonstrated slightly improved supersaturation effect on TDL compared to the HPC polymers after 30 min. Additionally, the concentrations were maintained, leading to concentrations of 30.8% (HPMCAS M) and 28.0% (HPMC HME 15 LV) after 60 min. While the presence of EL 100-55 showed only poor impact on TDL supersaturation, more than 70% of dissolved TDL was kept in solution by using EPO. In addition, VA 64 seemed to be a suitable polymer to maintain TDL in solution, as concentrations of 40.3% and 41.3% were detected after 30 and 60 min, respectively.

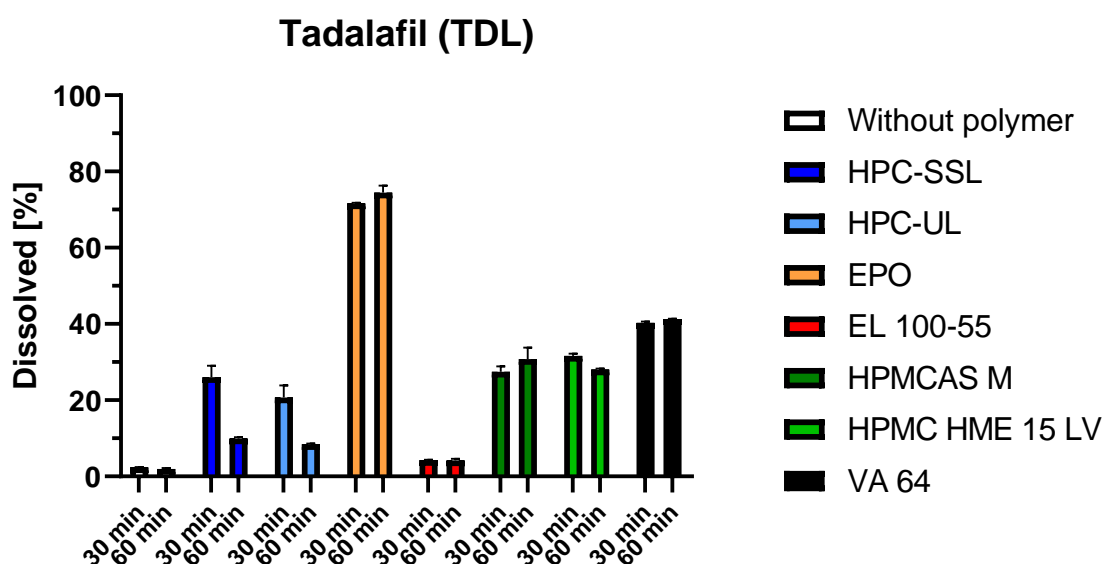


Figure 4: Supersaturation assay of 0.2 mg/mL (=100%) tadalafil (TDL) in pH 6.8 medium (0.05 M phosphate buffer) at 37 °C in presence of 1.25 mg/mL pre-dissolved single polymers and without polymer. In case of very low solubilities, concentrations cannot be displayed in this figure and the reader is referred to Table 5.

Table 5: Concentrations of dissolved tadalafil (TDL) in 0.05 M phosphate buffer pH 6.8, 37 °C, after 30 min and 60 min, dependent on the pre-dissolved polymer (1.25 mg/mL) and without polymer.

Polymer	Concentration after	Concentration after
	30 min [%]	60 min [%]
Without polymer	2.3 ± 0.1	2.0 ± 0.2
HPC-SSL	26.0 ± 3.0	10.0 ± 0.3
HPC-UL	20.7 ± 3.2	8.5 ± 0.2
EPO	71.6 ± 0.2	74.5 ± 1.8
EL 100-55	4.3 ± 0.2	4.2 ± 0.4
HPMCAS M	27.4 ± 1.4	30.8 ± 2.9
HPMC HME 15 LV	31.7 ± 0.5	28.0 ± 0.3
VA 64	40.3 ± 0.3	41.3 ± 0.1

Similar to the prior investigated drugs, the absence of any polymer led to almost complete precipitation of celecoxib (CXB), as a concentration of 1.1% was measured after 30 min (Figure 5 and Table 6). While EPO demonstrated high capability of stabilizing a supersaturated solution of CXB, EL 100-55 did not show a beneficial impact on supersaturation stabilization, as a concentration of 2.2% was obtained after 30 min. Comparable to EPO, HPMCAS M showed high potential in stabilizing a supersaturated CXB solution for at least 60 min, as concentrations of approx. 75% were detected after 30 and 60 min. Compared to HPMCAS M, HPMC HME 15 LV also appeared to be a suitable supersaturation stabilizing polymer, as only slightly decreased concentrations of approx. 60% were obtained. In contrast, HPC-SSL and HPC-UL showed decreased impact on the extent of the solubility, as concentrations of 23.8% and 32.2% were measured after 30 min, respectively. However, the HPCs, especially HPC-UL, prevented further precipitation as comparable concentrations were obtained after 60 min. In contrast, pronounced precipitation was observed using pre-dissolved VA 64, as only approx. 5% dissolved CXB was detected after 30 and 60 min.

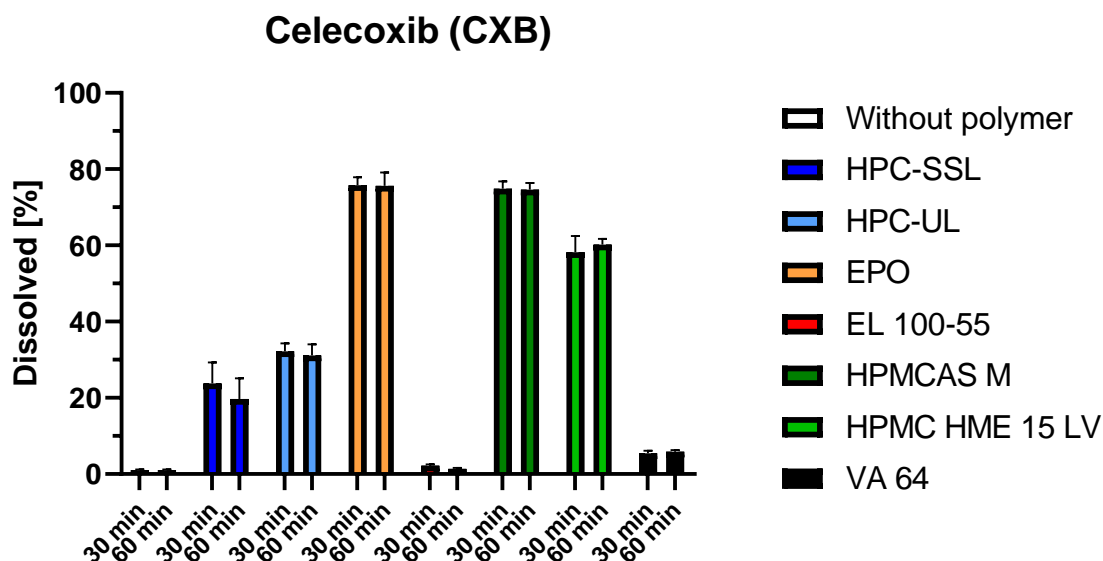


Figure 5: Supersaturation assay of 0.2 mg/mL (=100%) celecoxib (CXB) in pH 6.8 medium (0.05 M phosphate buffer) at 37 °C in presence of 1.25 mg/mL pre-dissolved single polymers and without polymer. In case of very low solubilities, concentrations cannot be displayed in this figure and the reader is referred to Table 6.

Table 6: Concentrations of dissolved celecoxib (CXB) in 0.05 M phosphate buffer pH 6.8, 37 °C, after 30 min and 60 min, dependent on the pre-dissolved polymer (1.25 mg/mL) and without polymer.

Polymer	Concentration after	
	30 min [%]	60 min [%]
Without polymer	1.1 ± 0.1	1.0 ± 0.2
HPC-SSL	23.8 ± 5.5	19.7 ± 5.4
HPC-UL	32.2 ± 2.0	31.1 ± 3.0
EPO	75.8 ± 2.1	75.6 ± 3.5
EL 100-55	2.2 ± 0.3	1.4 ± 0.2
HPMCAS M	74.9 ± 1.9	74.6 ± 1.8
HPMC HME 15 LV	58.2 ± 4.2	60.2 ± 1.5
VA 64	5.4 ± 0.7	5.9 ± 0.4

The supersaturation assay of efavirenz (EFV) revealed moderate impact of the HPC polymers on the extent of the supersaturated solution, as concentrations of approx. 30% were obtained after 30 min (Figure 6 and Table 7). Precipitation was prevented for at least further 30 min, as the concentrations did not decrease after 60 min. Compared to the pre-

dissolved HPC polymers, HPMCAS M and HPMC HME 15 LV enabled higher extent of supersaturation, leading to concentrations of 74.6% and 70.8% after 60 min, respectively. In case of pre-dissolved EPO approx. 85% of the added EFV was dissolved after 30 and 60 min. Instead, EL 100-55 was not capable of stabilizing the supersaturated solution, as the concentration of EFV decreased from 25.1% to 10.2% within the two measuring time points. Only little impact of VA 64 on EFV supersaturation was revealed, as concentrations between approx. 10 and 15% were detected.

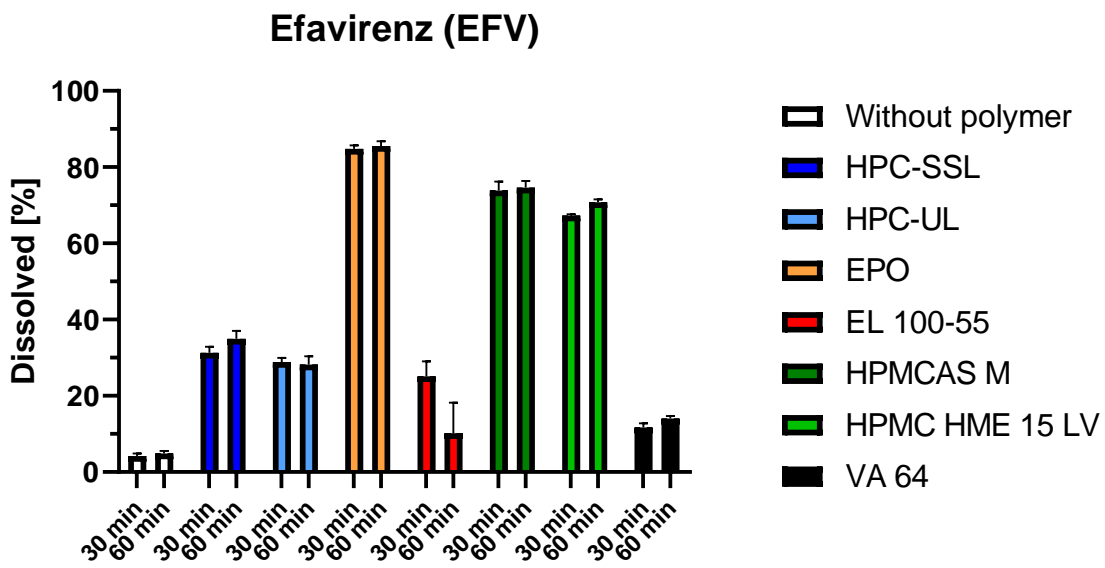


Figure 6: Supersaturation assay of 0.2 mg/mL (=100%) efavirenz (EFV) in pH 6.8 medium (0.05 M phosphate buffer) at 37 °C in presence of 1.25 mg/mL pre-dissolved single polymers and without polymer.

Table 7: Concentrations of dissolved efavirenz (EFV) in 0.05 M phosphate buffer pH 6.8, 37 °C, after 30 min and 60 min, dependent on the pre-dissolved polymer (1.25 mg/mL) and without polymer.

Polymer	Concentration after	Concentration after
	30 min [%]	60 min [%]
Without polymer	4.2 ± 0.7	4.9 ± 0.6
HPC-SSL	31.3 ± 1.5	35.0 ± 2.1
HPC-UL	28.8 ± 1.2	28.2 ± 2.1
EPO	84.8 ± 0.9	85.5 ± 1.2
EL 100-55	25.1 ± 3.9	10.2 ± 8.0
HPMCAS M	73.9 ± 2.3	74.6 ± 1.8
HPMC HME 15 LV	67.3 ± 0.4	70.8 ± 0.8
VA 64	11.7 ± 1.1	14.0 ± 0.7

Figure 7 and Table 8 represent the results of the supersaturation assay of clotrimazole (CLT). The concentrations of dissolved CLT were too low to be detectable, performing the testing in neat buffer and in presence of pre-dissolved HPC polymers and VA 64. Consequently, these polymers did not show a beneficial impact on the supersaturation of CLT. In contrast, pre-dissolved EPO demonstrated the highest benefit in terms of supersaturation stabilization, as more than 80% dissolved CLT was detected after 60 min. Utilizing EL 100-55, concentrations of 22.3% and 28.1% were obtained. Despite the pronounced impact of HPMC HME 15 LV on the solubility of CLT (64.8% after 30 min and 62.8% after 60 min), the concentration of dissolved drug was distinctly reduced using HPMCAS M, as concentrations of approx. 10% were measured.

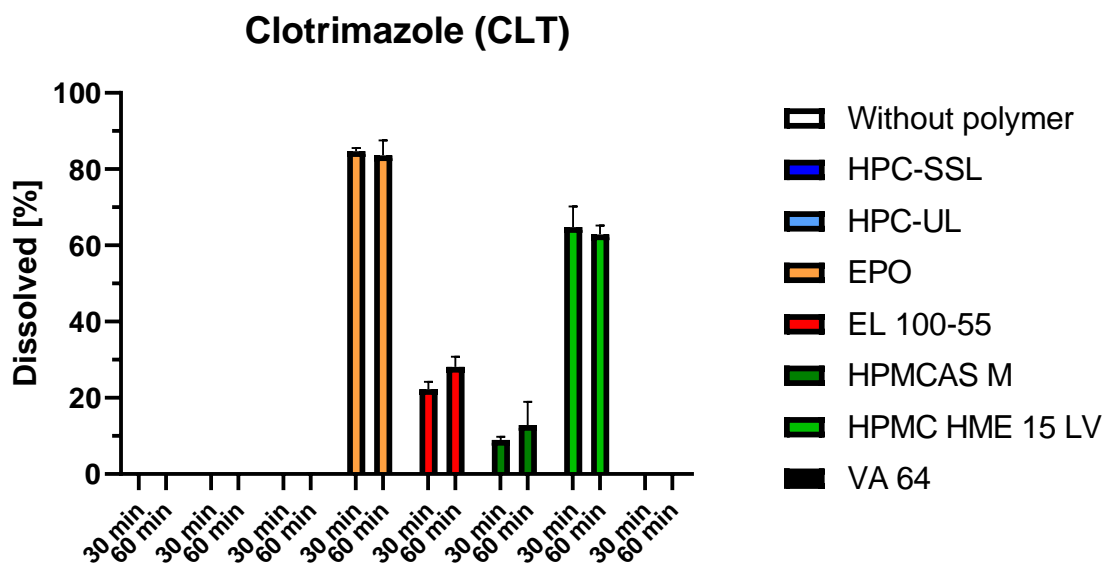


Figure 7: Supersaturation assay of 0.2 mg/mL (=100%) clotrimazole (CLT) in pH 6.8 medium (0.05 M phosphate buffer) at 37 °C in presence of 1.25 mg/mL pre-dissolved single polymers and without polymer. In case of very low solubilities, concentrations cannot be displayed in this figure and the reader is referred to Table 8.

Table 8: Concentrations of dissolved clotrimazole (CLT) in 0.05 M phosphate buffer pH 6.8, 37 °C, after 30 min and 60 min, dependent on the pre-dissolved polymer (1.25 mg/mL) and without polymer.

Polymer	Concentration after	
	30 min [%]	60 min [%]
Without polymer	n/a	n/a
HPC-SSL	n/a	n/a
HPC-UL	n/a	0.1 ± 0.1
EPO	84.7 ± 0.9	83.6 ± 3.9
EL 100-55	22.3 ± 1.9	28.1 ± 2.6
HPMCAS M	8.9 ± 0.9	12.9 ± 6.1
HPMC HME 15 LV	64.8 ± 5.4	62.8 ± 2.3
VA 64	n/a	n/a

Figure 8 and Table 9 reveal the supersaturation assay of lopinavir (LPV). Comparable to the supersaturation assay of FEN, only EPO showed pronounced impact on supersaturation stabilization of LPV. Pre-dissolving the alternative polymers did not lead to decisive higher LPV concentrations compared to the testing in neat buffer.

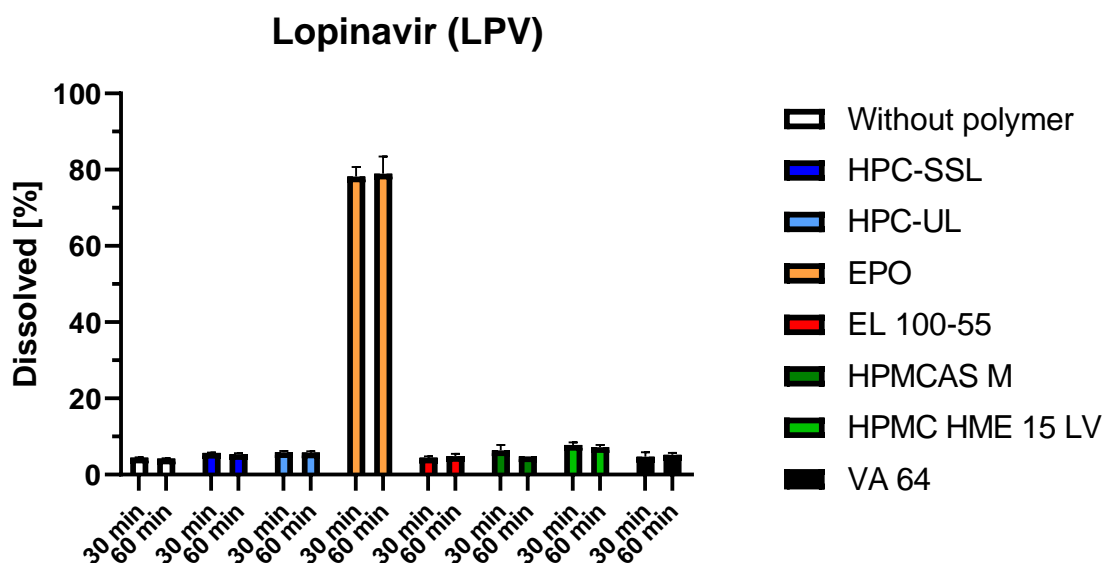


Figure 8: Supersaturation assay of 0.2 mg/mL (=100%) lopinavir (LPV) in pH 6.8 medium (0.05 M phosphate buffer) at 37 °C in presence of 1.25 mg/mL pre-dissolved single polymers and without polymer.

Table 9: Concentrations of dissolved lopinavir (LPV) in 0.05 M phosphate buffer pH 6.8, 37 °C, after 30 min and 60 min, dependent on the pre-dissolved polymer (1.25 mg/mL) and without polymer.

Polymer	Concentration after	Concentration after
	30 min [%]	60 min [%]
Without polymer	4.4 ± 0.1	4.2 ± 0.1
HPC-SSL	5.7 ± 0.1	5.4 ± 0.2
HPC-UL	5.9 ± 0.3	5.8 ± 0.3
EPO	78.2 ± 2.5	79.0 ± 4.5
EL 100-55	4.5 ± 0.3	4.9 ± 0.5
HPMCAS M	6.3 ± 1.5	4.8 ± 0.0
HPMC HME 15 LV	7.8 ± 0.6	7.2 ± 0.6
VA 64	4.7 ± 1.2	5.2 ± 0.5

Regarding all investigated drugs the supersaturation screening demonstrated that the extent and stabilization of supersaturation of poorly soluble drugs highly dependent on the individual drug-polymer combination. Accordingly, the structures of drugs and of the polymers (hydrophobicity and functional groups) play a decisive role in generating and stabilizing the supersaturated state of the drugs [35,69,70].

Surprisingly, EPO always showed high impact on the supersaturation level of the drugs, although it is regarded to be not soluble in pH 6.8 medium. Even supersaturated solutions of FEN and of LPV were obtained, which demonstrated fast-precipitating behavior in presence of all other pre-dissolved polymers. Apparently, a sufficient amount of EPO was dissolved to enable drug-polymer interaction and to maintain the supersaturated states. Higashi et al. reported drug- polymer interactions, observed via NMR spectroscopy by dispersing a mefenamic acid: EPO ASD in aqueous medium (pH 5.5), whereby hydrophobic and ionic interactions between drug and polymer under participation of the amino groups of EPO were detected [71].

Although the supersaturation results of this thesis are mechanistically interesting, dissolving EPO ASDs in pH 6.8 medium would not lead to comparable concentrations, as EPO ASDs would not demonstrate fast-dissolving characteristics. This assumption was confirmed by Lee et al. who investigated the dissolutions and supersaturation potentials of cilostazol using different types of polymers. Although EPO demonstrated high potential in generating and stabilizing a supersaturated solution of cilostazol in pH 6.8 medium, the corresponding ASDs (10 and 33% drug load) did not lead to satisfied dissolution performances [72]. In order to increase the solubility of the polymer and to enable faster dissolution rate, several studies neutralized EPO using hydrochloric acid [72–75]. Although further experiments using EPO as ASD-forming polymer were not conducted in this thesis, the neutralization of EPO for the investigated drugs seems to be an interesting approach. The alternative poly acrylate derivate EL 100-55 provides carboxylic acid groups and esterified carboxyl groups; thus EL 100-55 belongs to the pH-dependent soluble polymers above pH 5.5. The acidic functional groups for intermolecular interactions were discussed as the predominate precipitation mechanism for poorly soluble drugs [76]. The effect of EL 100-55 on the supersaturation of the investigated drugs was observed to be very variable, as in many cases the precipitation was not prevented. However, EL 100-55 demonstrated pronounced impact on the supersaturation of KTZ. Accordingly, investigations of KTZ supersaturating formulations using EL 100-55 as ASD-forming polymer were already published previously, demonstrating successful KTZ supersaturation stabilization for at least 180 min [29].

The HPC polymers demonstrated only little or moderate effect on the supersaturation stabilization of the investigated drugs. Niederquell et al. investigated the impact of different HPC grades on drug precipitation inhibition and proposed dispersive interactions, polar interactions, and hydrogen bonding as potential interactions mechanisms for stabilizing supersaturated drug solutions [77].

However, comparing the group of the cellulose-based polymers, HPMCAS M and HPMC HME 15 LV provided higher impact on the supersaturation of the drugs than the HPC polymers. For cellulose derivatives, moderate hydrophobic properties were demonstrated to be important for inhibiting precipitation [65,78,79]. Due to the additional methylation of the basic structure of cellulose, HPMC provides a more hydrophobic character than the HPC polymers [80]. In case of HPMCAS M, the moderate hydrophobic properties and additional functional groups (acetyl and succinyl substitution) offer promising interactions spots for inhibiting drugs precipitation [35].

Next to the polyacrylate and cellulose derivatives, the capability of VA 64 in maintaining the supersaturated state of poorly soluble drugs was investigated. Although VA 64 is a commonly used polymer for ASD processing, the polymer did not demonstrate promising capability in maintaining the supersaturated state of the drugs (except for TDL). As VA 64 exhibits high hydrophilic character [81], the pre-dissolved polymer potentially interacted preferably with water than with the drug. Chen et al. observed that by pre-dissolving the related hydrophilic polymer polyvinylpyrrolidone (PVP) K30 the supersaturated state of the subsequent added drug dropped immediately. As the pre-dissolved polymer already formed hydrogen bonding with the water molecules, only reduced capability for forming interactions with the added drug was provided [82].

2.3. Supersaturation screening of various drugs dependent on pre-dissolved polymer mixtures, comprising Eudragit® L 100-55 and hydroxypropyl cellulose-SSL (50:50)

Since the supersaturation potential of the drugs in dependence on pre-dissolved single polymers were investigated, the effect of a polymer mixture, consisting of EL 100-55: HPC-SSL (50:50 mass ratio), on maintaining the supersaturated states was evaluated and compared to the supersaturation results of the corresponding single polymers (chapter 2.2.). For a direct evaluation of the effect of the polymer combination, the total polymer concentration of 1.25 mg/mL was equal to the supersaturation testing of the single polymers. For better visualization, the results of the eight drugs are presented in two figures (KTZ, DNZ, FEN, TDL in Figure 9 and CXB, EFV, CLT, LPV in Figure 10). Similar to the presentation of the supersaturation results of all single polymers in chapter 2.2., the Y-axes of the figures demonstrate the dissolved amount of the drugs from 0 to 100%. In case of very small concentrations, the reader is referred to Table 10, where the concentrations of all supersaturation results using the polymer mixture EL 100-55: HPC-SSL and the corresponding single polymers are provided.

Regarding KTZ (Figure 9A), the combination of EL 100-55: HPC-SSL led to a comparable supersaturation extent after 30 min compared to single EL 100-55, as concentrations of 69.0% and 73.7% were determined, respectively. However, while EL 100-55 alone successfully stabilized the supersaturated after 60 min, the reduced KTZ concentration and the high standard deviation ($35.4 \pm 32.5\%$) for the polymer mixture demonstrated instability of the supersaturated state. Consequently, the addition of HPC-SSL to EL 100-55 impaired the supersaturation performance of KTZ.

Comparable to the supersaturation results of the single polymers the combination EL 100-55 and HPC-SSL did not lead to improved solubility of DNZ (Figure 9B) and FEN (Figure 9C).

In case of TDL (Figure 9D), combining the polymers did not demonstrate a beneficial effect neither, as HPC-SSL as single polymer revealed superiority with respect to the measured concentrations after 30 min. While pre-dissolved HPC-SSL alone enabled 26.0% of dissolved TDL, only 7.7% were determined for the polymer mixture.

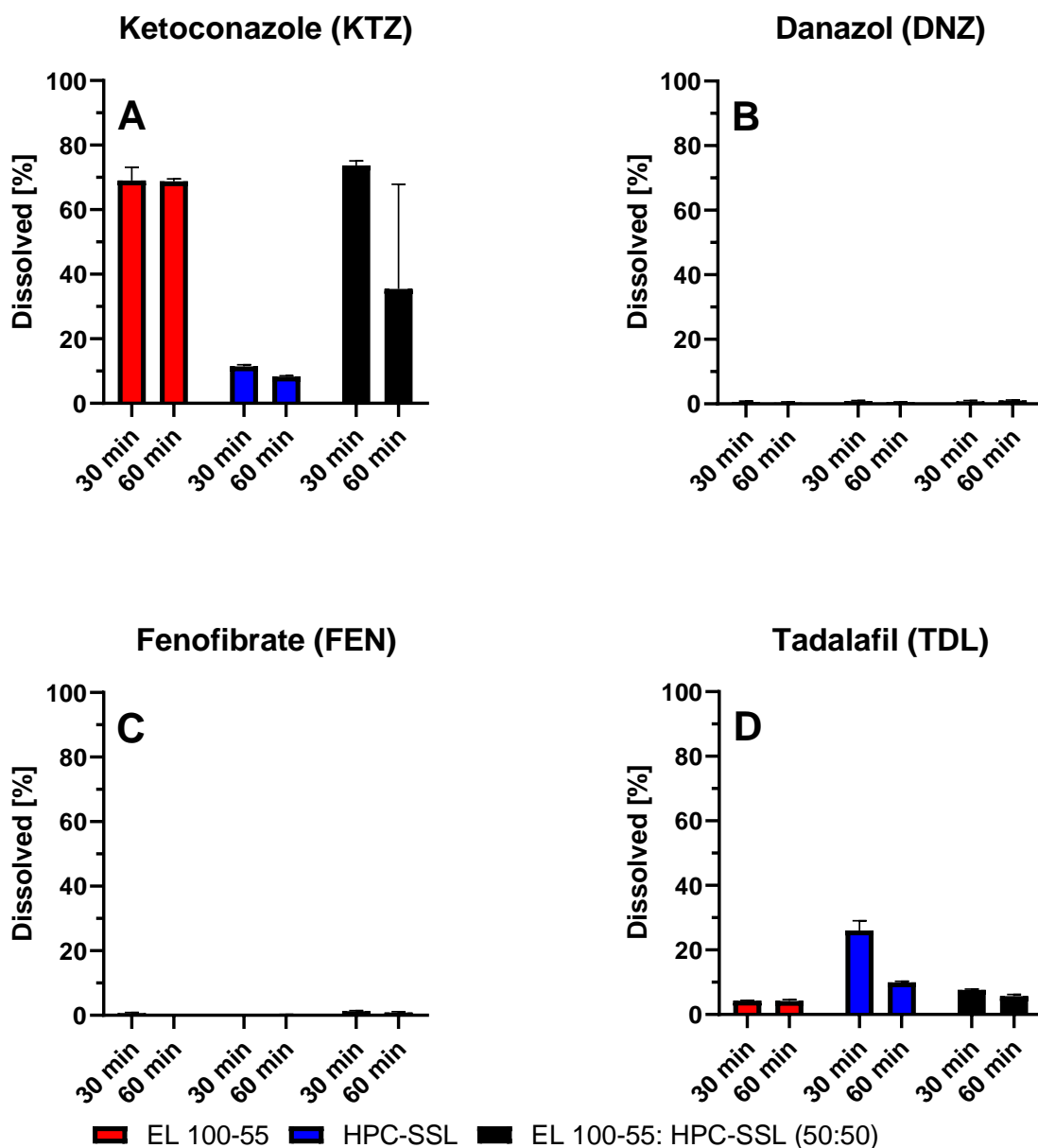


Figure 9: Supersaturation assay of 0.2 mg/mL (=100%) ketoconazole (KTZ) (A), danazol (DNZ) (B), fenofibrate (FEN) (C), and tadalafil (TDL) (D) in 0.05 M phosphate buffer at pH 6.8, 37 °C, dependent on 1.25 mg/mL pre-dissolved single polymers EL 100-55, HPC-SSL, and the polymer combination EL 100-55: HPC-SSL (50:50). The total polymer concentration in each experiment was 1.25 mg/mL. In case of very low solubilities, concentrations cannot be displayed in this figure and the reader is referred to Table 10.

However, a synergistic interplay between EL 100-55 and HPC-SSL was observed for the supersaturation of CXB (Figure 10A). While pre-dissolving EL 100-55 alone did not lead to increased solubility values of CXB and HPC-SSL alone demonstrated only moderate impact on CXB supersaturation (23.8% after 30 min and 19.7% after 60 min), the polymer

combination stabilized almost 70% of dissolved CXB after 30 and 60 min. The synergistic interplay between EL 100-55 and HPC-SSL were also clearly visible in the supersaturation assay of EFV and CLT. In presence of single EL 100-55, the concentration of dissolved EFV decreased during the assay from 25.1% (30 min) to 10.2% (60 min), indicating the inability to maintain the supersaturated system successfully. While HPC-SSL alone was able to maintain a supersaturated concentration of 35.0% after 60 min, 55.2% and 50.9% dissolved EFV was detected after 30 min and 60 min, using the mixture of EL 100-55 and HPC-SSL (Figure 10B). In case of the supersaturation assay of CLT (Figure 10C) no detectable drug concentration was obtained by pre-dissolving HPC-SSL, while EL 100-55 enabled only moderate CLT concentrations of 22.3% after 30 min and 28.1% after 60 min. However, the polymer combination of EL 100-55 and HPC-SSL demonstrated a pronounced impact on the supersaturation of CLT, as concentrations of 54.5% and 60.3% were obtained after 30 and 60 min, respectively. Regarding LPV (Figure 10D), both the single polymers and the polymer combination were not suitable for sufficient generation and stabilization of a supersaturated state of the drug.

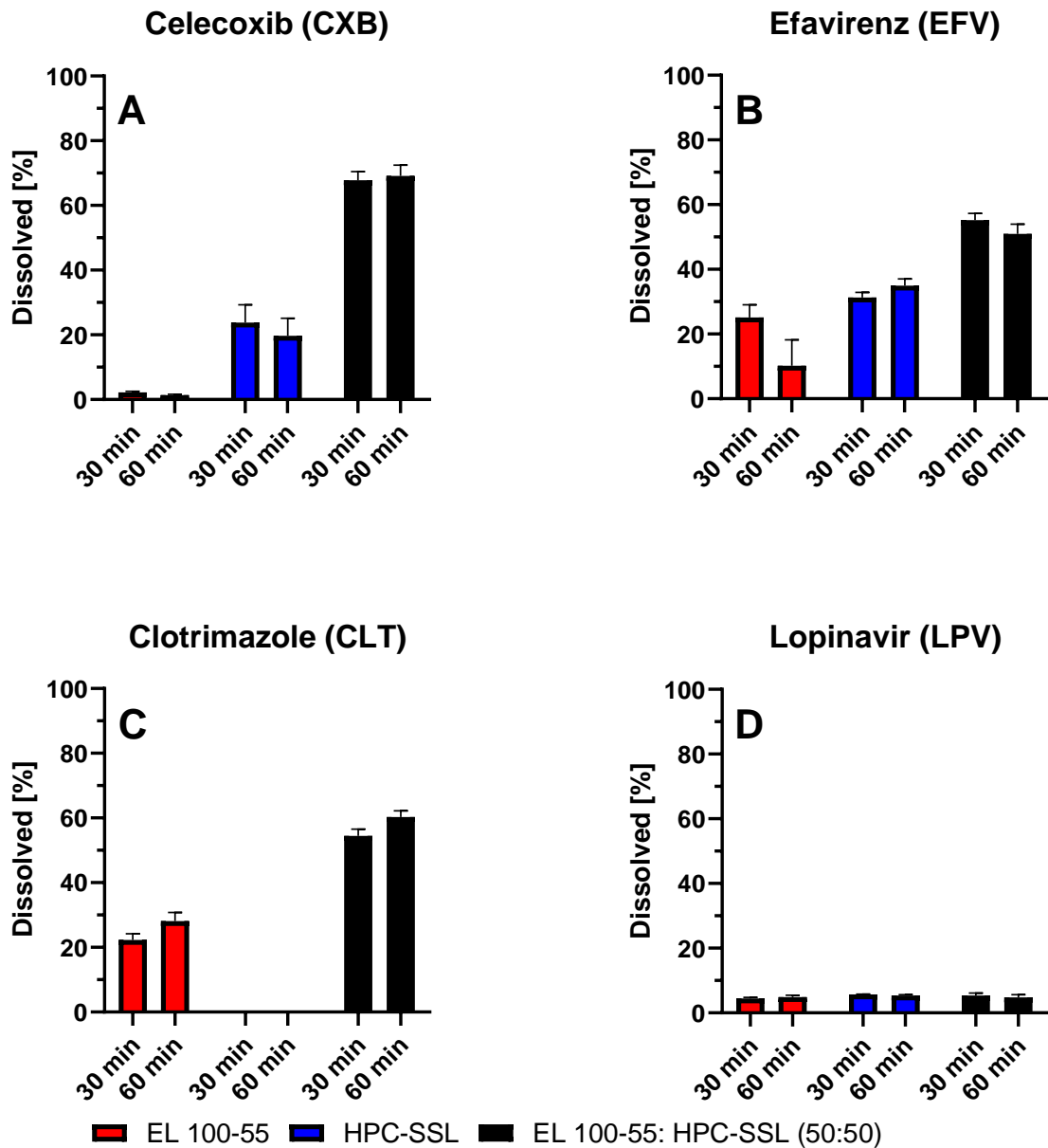


Figure 10: Supersaturation assay of 0.2 mg/mL (=100%) celecoxib (CXB) (A), efavirenz (EFV) (B), clotrimazole (CLT) (C), and lopinavir (LPV) (D) in 0.05 M phosphate buffer at pH 6.8, 37 °C, dependent on 1.25 mg/mL pre-dissolved single polymers EL 100-55, HPC-SSL, and the polymer combination EL 100-55: HPC-SSL (50:50). The total polymer concentration in each experiment was 1.25 mg/mL. In case of very low solubilities, concentrations cannot be displayed in this figure and the reader is referred to Table 10.

Table 10: Concentrations of the dissolved drugs after 30 min and 60 min in presence of pre-dissolved EL 100-55, HPC-SSL, and the polymer combination EL 100-55: HPC-SSL (50:50) in 0.05 M phosphate buffer pH 6.8, 37 °C. The total polymer concentration in each experiment was 1.25 mg/mL.

Drug	Polymer	Concentration after 30 min [%]	Concentration after 60 min [%]
Ketoconazole (KTZ)	EL 100-55	69.0 ± 4.1	68.8 ± 0.7
	HPC-SSL	11.4 ± 0.8	8.3 ± 0.3
	EL 100-55: HPC-SSL (50:50)	73.7 ± 1.5	35.4 ± 32.5
Danazol (DNZ)	EL 100-55	0.6 ± 0.3	0.3 ± 0.3
	HPC-SSL	0.8 ± 0.2	0.5 ± 0.1
	EL 100-55: HPC-SSL (50:50)	0.8 ± 0.2	1.1 ± 0.2
Fenofibrate (FEN)	EL 100-55	0.7 ± 0.2	n/a
	HPC-SSL	0.2 ± 0.0	0.3 ± 0.0
	EL 100-55: HPC-SSL (50:50)	1.3 ± 0.2	0.9 ± 0.3
Tadalafil (TDL)	EL 100-55	4.3 ± 0.1	4.2 ± 0.4
	HPC-SSL	26.0 ± 3.0	10.0 ± 0.4
	EL 100-55: HPC-SSL (50:50)	7.7 ± 0.2	5.7 ± 0.5
Celecoxib (CXB)	EL 100-55	2.2 ± 0.3	1.4 ± 0.2
	HPC-SSL	23.8 ± 5.5	19.7 ± 5.4
	EL 100-55: HPC-SSL (50:50)	67.8 ± 2.7	69.1 ± 3.4
Efavirenz (EFV)	EL 100-55	25.1 ± 3.9	10.2 ± 8.0
	HPC-SSL	31.3 ± 1.5	35.0 ± 2.1
	EL 100-55: HPC-SSL (50:50)	55.2 ± 2.1	50.9 ± 3.1

Evaluation of polymer-mediated supersaturation and precipitation inhibition of poorly soluble drugs

Drug	Polymer	Concentration after 30 min [%]	Concentration after 60 min [%]
Clotrimazole (CLT)	EL 100-55	22.3 ± 1.9	28.1 ± 2.6
	HPC-SSL	n/a	n/a
	EL 100-55: HPC-SSL (50:50)	54.5 ± 2.1	60.3 ± 1.9
Lopinavir (LPV)	EL 100-55	4.5 ± 0.3	4.9 ± 0.5
	HPC-SSL	5.7 ± 0.1	5.4 ± 0.2
	EL 100-55: HPC-SSL (50:50)	5.3 ± 0.8	4.8 ± 0.8

2.4. Conclusion

The results of the supersaturation assay revealed the variability of supersaturation stabilization in dependence on the individual selected drug-polymer system.

As general superiority of specific pre-dissolved individual polymers was not revealed, the importance of performing supersaturation experiments as preliminary experiments for focusing on best supersaturation-stabilizing polymer for further formulation development was underlined.

Noticeably, EPO represents an exception. Despite an actual insoluble character in pH 6.8 medium, suspended EPO demonstrated overall superior precipitation inhibiting impact on the supersaturated drugs. Although these results provided interesting mechanistic insights into the liquid-state interactions, structural changes of EPO to increase polymer solubility would be necessary to enable promising dissolution rate of EPO ASDs in pH 6.8 medium.

Aside the investigations of the single polymers, the combination of EL 100-55 and HPC-SSL (50:50) revealed the potential of polymer mixtures for extending the selection of polymers in terms of choosing the correct polymer for supersaturation of each drug. By investigating eight drugs, both the positive and the negative effects of polymer combinations were illustrated. Impaired effects were documented for supersaturating KTZ and TDL. However, for CXB, EFV, and CLT, synergistic interactions of EL 100-55 and HPC-SSL enabled supersaturated drug concentrations that went beyond the effect of the individual polymers. For these drugs, the single polymers demonstrated only moderate/poor impact on the individual supersaturated state, thus alone they would not be further considered for processing supersaturating formulations. Combined, new possibilities in terms of solubility increasement and supersaturation stabilization were offered.

3. Enhancement of supersaturation performance of celecoxib using polymer combinations of Eudragit® L 100-55 and hydroxypropyl cellulose

3.1. Introduction

The supersaturation screening method of chapter 2.3. revealed synergistic interplay between EL 100-55 and HPC-SSL for maintaining the supersaturated state of three drugs (CXB, EFV, and CLT) for at least 60 min.

For further characterization of the synergistic interactions between these polymers in liquid-state, the supersaturation potential of CXB, as selected model drug, was investigated in detail for 180 min utilizing the MiniDissolution apparatus for enabling a more precious investigation of the supersaturation. In addition, different HPC grades were utilized, examining not only HPC-SSL, but also HPC-UL and HPC-L as polymer partner of EL 100-55.

Moreover, the impact of different polymer-polymer mass ratios (25:75, 50:50, 75:25) on the extent and stabilization of the supersaturated state of CXB was explored [83].

Table 11: Physicochemical properties of the investigated HPC grades, including the molecular weights (MWs) [84], the moles of substituent combined (MS), the average number of substituent groups per monomer unit (DS) and the hydroxypropoxy content [%] [77].

Physicochemical properties	HPC-L	HPC-SSL	HPC-UL
Molecular weight (MW) [g/mol]	140,000	40,000	20,000
Moles of substituent combined (MS)	3.8	3.6	3.4
Average number of substituent groups per monomer unit (DS)	2.8	2.2	1.8
Hydroxypropoxy content [%]	74.7	73.2	70.6

As depicted in Table 11, the three HPC grades (HPC-L, -SSL, and -UL) differ in molecular weight (MW) [84], thus at fixed mass ratio, the molar ratios between EL 100-55 (MW of 320,000 g/mol [85]) and HPC change dependent on the selected grade. Aside the MW, the HPC grades also differ slightly in further structural aspects, as the lower MW polymers reveal lower molecular substitution (MS), lower average number of substituent groups per monomer unit (DS), and a lower hydroxypropoxy content [77] (Table 11). Moreover, as illustrated by Figure 11, low MW HPC-UL exhibits a more linear polymer structure in

aqueous medium with lower strength of intramolecular interactions. Instead, the higher MW HPC grade HPC-L form a more tangled molecule with twisted and bended structure, as consequence of closer distance between the propoxyl groups and the cellulose skeleton [86].

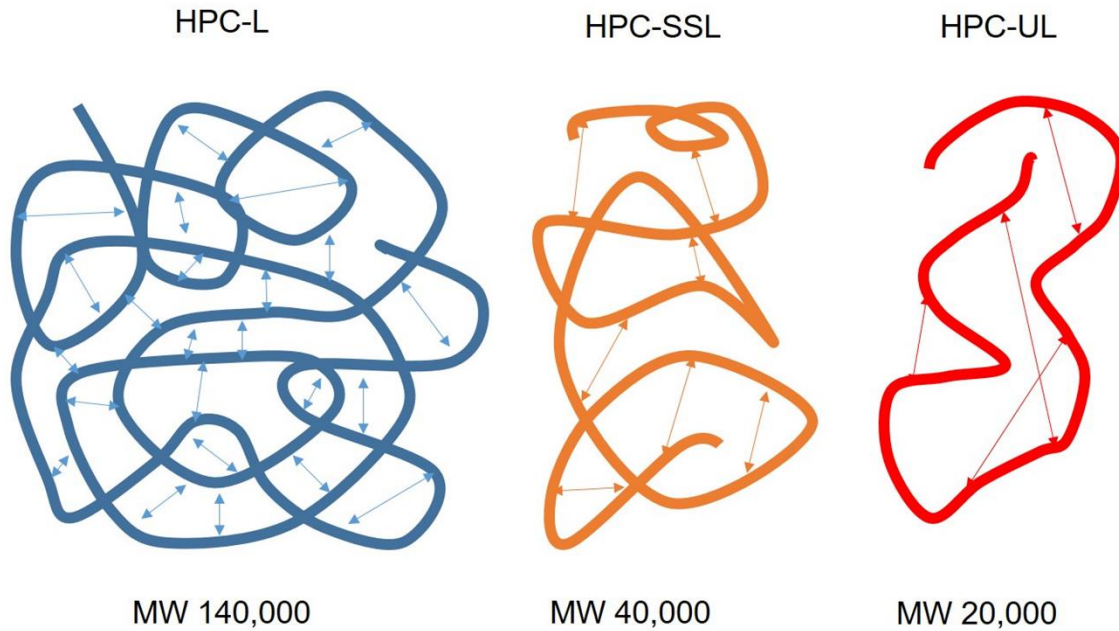


Figure 11: Potential formation of the selected HPC grades in solution, adapted from Sakamoto and Stoyanov., 2020 [86], licensed under a Creative Commons Attribution 4.0 International License.

3.2. The influence of different hydroxypropyl cellulose grades and polymer ratios with Eudragit® L 100-55 on celecoxib supersaturation

Parts of this chapter have been published in a peer-reviewed research article [83]. Each figure was created by the thesis author. Taking or adapting of figures is marked in the corresponding figure.

The supersaturation results of CXB in neat buffer and in presence of pre-dissolved single polymers (EL 100-55, HPC-L, HPC-SSL, and HPC-UL) are presented in Figure 12. In neat buffer, a maximum CXB concentration of 16% was determined after 6 min, followed by a sudden drop to less than 1% due to precipitation. By pre-dissolving EL 100-55, the solubility of CXB was slightly improved, as an initial supersaturation of 27% CXB was generated that however, also collapsed completely after 7 min. Instead, by pre-dissolving the HPC polymers the generated supersaturation of CXB was stabilized for more than 120 min, independently on the selected HPC grade. Differences between the HPC grades were observed in terms of supersaturation extent. While HPC-L and HPC-SSL showed a maximum CXB solubility of 23%, pre-dissolved HPC-UL enabled a supersaturated state of 33%. The differences between HPC-SSL and HPC-UL were already observed in the supersaturation screening of CXB (chapter 2.2.) and corresponded well to the detected concentrations of this study. The more linear structure of the lowest MW HPC grade -UL could be favorable for intermolecular interactions with CXB. As consequence of the more linear structure, HPC-UL exhibits the lowest extent of intramolecular interactions [86], thus enabling more potential interaction spots with CXB.

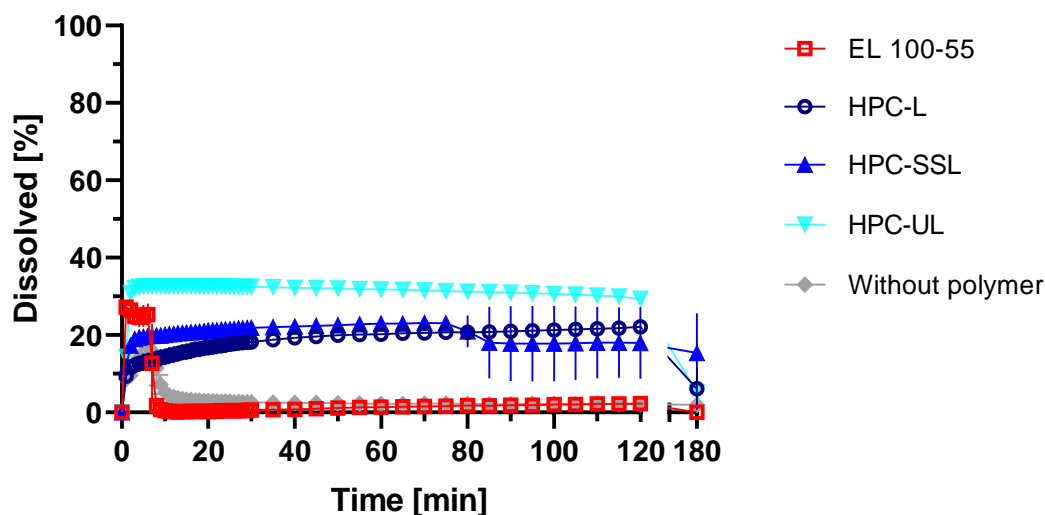


Figure 12: Supersaturation assay of 0.2 mg/mL (=100%) celecoxib (CXB) in 0.05 M phosphate buffer at pH 6.8 without pre-dissolved polymers and in presence of 1.25 mg/mL pre-dissolved single polymers. The assay was performed in 20 mL buffer medium at 37 °C and 75 rpm paddle speed. This figure was partially adapted from Pöstges et al., 2022 [83].

Figure 13 represents the supersaturation assay of CXB in presence of pre-dissolved polymer combinations, by varying the HPC grade (HPC-L, HPC-SSL, HPC-UL) and the EL 100-55: HPC polymer mass ratio (75:25, 50:50, 25:75). Independent on the selected HPC grade and polymer mass ratio, all combinations of EL 100-55: HPC led to remarkable initial supersaturation of CXB and outperformed the single polymers decisively.

By varying the HPC grades and the EL 100-55: HPC ratios, slight differences in maximum supersaturation extent were observed (Table 12). The highest amount of dissolved CXB ($81.3 \pm 0.3\%$) was achieved by pre-dissolving EL 100-55: HPC-L (75:25) (Figure 13A), while the lowest C_{\max} ($70.2 \pm 0.9\%$) was measured using the combination EL 100-55: HPC-UL (25:75) (Figure 13C). As HPC-L showed the highest MW (140,000 g/mol), the combination EL 100-55: HPC-L (75:25) was the only polymer combination with a molecular excess of EL 100-55 (mole ratio HPC/ EL 100-55: 0.76). HPC-UL showed the smallest MW (20,000 g/mol), thus the polymer combination EL 100-55: HPC-UL (25:75) represented the combination with the highest molecular excess of HPC (mole ratio HPC/ EL 100-55: 48.00). However, a sound correlation between mole ratio and C_{\max} for all investigated polymer mixtures was not feasible.

Moreover, differences in terms of supersaturation stabilization were observed. Independent on the HPC grade, a mass excess of EL 100-55 led to earlier collapse of CXB

supersaturation compared to the 50:50 ratios or to the excesses of HPC. By pre-dissolving the polymer mixture EL 100-55: HPC-UL (75:25) the supersaturation of CXB was maintained for only 20 min. Pre-dissolved EL 100-55: HPC-SSL (75:25) and EL 100-55: HPC-L (75:25) stabilized the supersaturation for 30 min and 35 min, respectively. Best results in terms of maintaining the supersaturation (70 min) were achieved utilizing EL 100-55 and HPC-SSL in a ratio of 50:50 (Figure 13B). EL 100-55: HPC-L (50:50) and EL 100-55: HPC-UL (50:50) showed a slight reduced maintenance with a stabilization time of about 60 min. The most pronounced difference between the HPC grades was observed pre-dissolving a polymer ratio of EL 100-55: HPC (25:75). While the use of HPC-SSL and HPC-L led to a CXB supersaturation stabilization of 60 min, the combination with the lowest molecular weight polymer HPC-UL led to an early collapse of solubility after 20 min.

Enhancement of supersaturation performance of celecoxib using polymer combinations of Eudragit® L 100-55 and hydroxypropyl cellulose

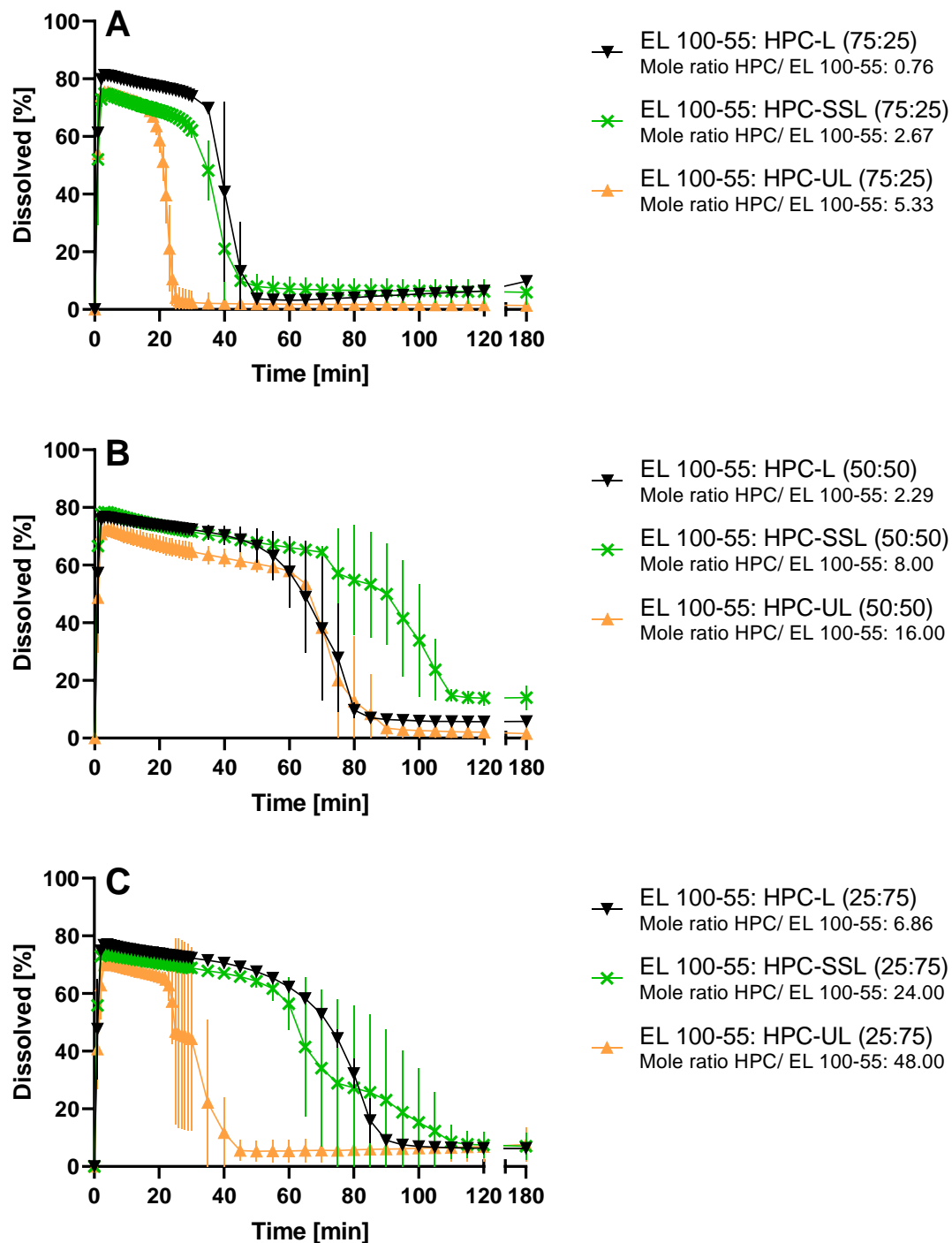


Figure 13: Supersaturation assay of 0.2 mg/mL (=100%) celecoxib (CXB) in 0.05 M phosphate buffer at pH 6.8 in presence of 1.25 mg/mL pre-dissolved polymer mixtures, varying the HPC grade (HPC-L, HPC-SSL, and HPC-UL) and the polymer mass ratio: EL 100-55: HPC (75:25) (A), EL 100-55: HPC (50:50) (B) and EL 100-55: HPC (25:75) (C). For every combination the corresponding polymer-polymer mole ratio is given. The assay was performed in 20 mL buffer medium at 37 °C and 75 rpm paddle speed. This figure was partially adapted from Pöstges et al., 2022 [83].

Table 12: All investigated polymer combinations, ordered by mole ratio HPC/ EL 100-55 (low -> high): Calculation of mole ratio is based on molecular weights (MWs) of the utilized polymers: EL 100-55 (320,000 g/mol) [85], HPC-L (140,000 g/mol), HPC-SSL (40,000 g/mol), HPC-UL (20,000 g/mol) [84]. C_{max} [%] of EL 100-55: HPC-SSL combinations were obtained from Pöstges et al., 2022 [83].

Mole ratio HPC/ EL 100-55	Polymer combination	C_{max} [%] of supersaturation assay
0.76	EL 100-55: HPC-L (75:25)	81.3 ± 0.3
2.29	EL 100-55: HPC-L (50:50)	76.7 ± 1.1
2.67	EL 100-55: HPC-SSL (75:25)	74.9 ± 2.0
5.33	EL 100-55: HPC-UL (75:25)	75.5 ± 0.1
6.86	EL 100-55: HPC-L (25:75)	77.0 ± 0.8
8.00	EL 100-55: HPC-SSL (50:50)	78.4 ± 1.3
16.00	EL 100-55: HPC-UL (50:50)	72.4 ± 2.5
24.00	EL 100-55: HPC-SSL (25:75)	73.7 ± 0.8
48.00	EL 100-55: HPC-UL (25:75)	70.2 ± 0.9

3.3. Conclusion

While neither EL 100-55 nor HPC-SSL alone demonstrated promising impact on extent and stabilization of the supersaturated state of CXB, the combinations of EL 100-55 and HPC led to remarkable increase of CXB solubility and supersaturation. Differences in supersaturation performances were observed dependent on the polymer ratio and on the HPC grade. The highest initial supersaturation was measured using EL 100-55: HPC-L (75:25), the only combination with molecular excess of EL 100-55. Presence of sufficient EL 100-55 molecules was important for maximum initial CXB concentrations. On the other hand, HPC was crucial for the supersaturation maintenance, as 50:50 ratios or excesses of HPC led to promising stabilization results independent on HPC grade. However, the low supersaturation stabilization capability of EL 100-55: HPC-UL (25:75) represents an exception. The very pronounced molecular excess of the low MW HPC-UL led to earlier collapse, indicating reduced synergistic interactions.

4. Impact of the manufacturing method on the solid-state of polymer placebo mixtures, comprising Eudragit® L 100-55 and hydroxypropyl cellulose

4.1. Introduction

The supersaturation assay of the previous chapters underlined the importance of the correct polymer selection to successfully stabilize individual supersaturated systems in liquid-state.

To extend the opportunities in the selection of polymers, there is great interest in developing new polymers with optimized material properties. However, as the development of new polymers is usually cost-intensive and the successful establishment on the market requires many years, polymer blending has gained much attention. Blending two or more commercially available polymers enables an easy and cost-effective opportunity to create new material with different physicochemical properties [87–89]. In this context, the supersaturation assay (chapter 2.3. and 3.2.) already revealed the superiority of the polymer mixture EL 100-55: HPC for enabling higher supersaturations of CXB, EFV and CLT compared to the utilization of the single polymers.

Processing two polymers for the manufacturing of solid formulations leads to a homogeneous or a heterogeneous polymer blend, depending on miscibility of both polymers. Homogeneous polymer blends are characterized by complete mixing and form a single phase [90]. Heterogeneous polymer blends are considered to be either partially miscible or complete immiscible [91].

However, preparing homogeneous polymer mixtures is quite challenging, not only due to high melt viscosity of the polymers, but also due to thermodynamic reasons [92].

Whether polymers mix spontaneously or not depends on the value of the Gibbs free energy ΔG_m of mixing [93]:

$$\Delta G_m = \Delta H_m - T\Delta S_m \quad (\text{Equation 2})$$

To obtain a homogeneous and single-phased system, ΔG_m must be necessarily negative [94]. As mixing of two components causes disorder, the entropy ΔS_m always increases, hence the entropic contributions would facilitate homogeneous mixing of both polymers. However, for high molecular molecules like polymers the entropic contribution for mixing

is quite small [92]. Therefore, the enthalpic component ΔH_m of the free energy is decisive, whether mixing occurs or not, whereby the Flory-Huggins interaction parameter between both polymers is a determining factor [94]. The interaction parameter can be calculated on a theoretical approach. From the enthalpic perspective, a positive interaction parameter would indicate unfavorable mixing, while a negative value implies stronger adhesive than cohesive forces, facilitating polymer mixing [94].

Previous studies demonstrated the influence of polymer mixing on the extent of interactions between the polymers and the processed drug in so-called ternary ASDs [95,96]. Therefore, before embedding a drug into the polymer matrix, polymer mixing and polymer-polymer interactions in placebo formulations were investigated in this chapter.

Several methods for investigating polymer mixing and polymer-polymer interactions are applicable. In this study, the T_g , as a characteristic property of each polymer, was utilized to evaluate polymer mixing. The T_g describes the thermal transition from a brittle and rigid character to a soft and leathery state and can be measured via differential scanning calorimetry (DSC). The DSC is an analytical tool for determining the difference of the heat flow between a sample and a reference as a function of temperature. Thermal events are indicated by a change of the heat flow, resulting in an endothermic peak in case of melting of crystalline material or in a step-like signal at the glass transition of amorphous material [45].

Depending on the mixing behavior, the single polymers of a polymer blend change the T_g after processing [97,98]. In case of complete mixing, the polymers form a homogeneous and single phase, resulting in a single T_g at an intermediate value. If the polymers are completely immiscible, the polymer phases do not interact with each other, leading to two unchanged T_g s. Partially miscible phases are typically characterized by two slightly changed T_g s, depending on the extent of mixing [91]. However, the DSC is limited in distinguishing between nanosized phase separated domains [99].

Confocal Raman spectroscopy (CRS) represents an additional analytical tool to verify and deepen the solid-state phases by visualizing distributions of the substances [100,101].

As the single compounds exhibit different Raman intensities at specific wavenumbers, the characteristic Raman shifts can be utilized to image the presence or absence of the corresponding substance.

However, limited spatial resolution of the optics or the potential strong fluorescence signals of the single components may restrict the usage of the tool [99,102].

For elucidating solid-state interactions between two components, e.g., two polymers, Fourier-transform infrared spectroscopy (FT-IR) is a common and suitable analytical tool. Interactions between two substances are indicated by shifts or reduction in intensity of characteristic FT-IR bands in comparison to the unprocessed single polymers and PMs [103]. As the FT-IR bands are assigned to specific functional groups or atomic bonds, the involved chemical moieties can be identified easily.

As different manufacturing methods for ASD processing are applicable, placebo formulations of EL 100-55: HPC-SSL (50:50) and EL 100-55: HPC-UL (50:50) were processed via the heat-based preparation methods VCM (non-shear method) and HME (heat + shear method), and via the solvent-based preparation method SD. The different processing principles were already presented in chapter 1.3. of this thesis. Regarding the heat-based preparation methods, the individual thermal stability of the single polymers must be considered, thus thermogravimetric analysis (TGA) of the single polymers were conducted prior to the processing.

The impact of the different manufacturing methods on polymer mixing and polymer-polymer interactions were investigated via DSC, CRS and FT-IR [83,104].

4.2. Assessment of thermal stability of the polymers for the heat-based preparation methods

Preparations of formulations via VCM and HME require thermostability of the processed substances. Therefore, thermal stability as consequence of degradation processes were investigated via TGA. As the maximum thermal exposure of the processed polymers was the VCM processing conditions of 160 °C for 15 min, weight losses [%] of the neat polymers during a heating period of 160 °C for 15 min were determined.

During the isocratic heating period, EL 100-55, HPC-SSL and HPC-UL demonstrated a weight loss of 0.21%, 0.29% and 0.53%, respectively (Figure 14). Accordingly, the selected VCM processing conditions of 160 °C for 15 min, and the maximum HME temperature of 150 °C seemed to be suitable temperatures for processing the placebo formulations.

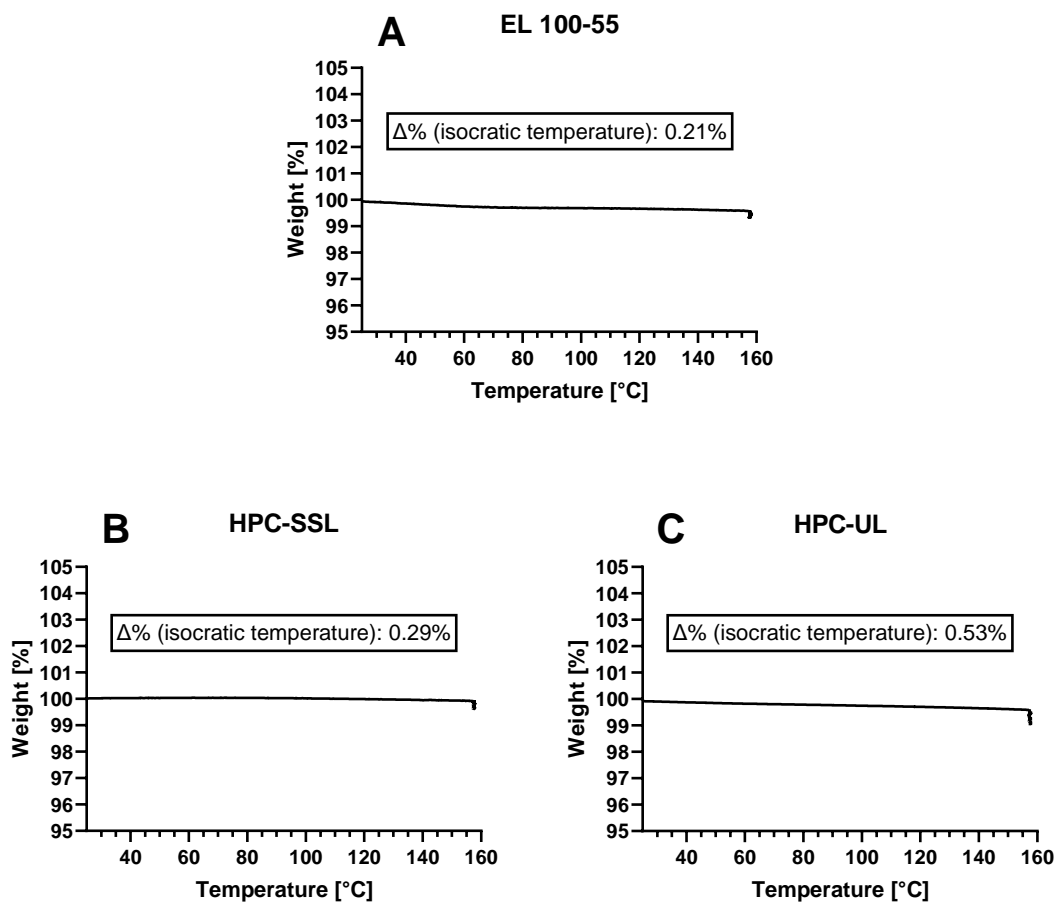


Figure 14: Thermogravimetric analysis (TGA) of neat EL 100-55 (A), HPC-SSL (B) and HPC-UL (C). After heating to 160 °C (vacuum compression molding (VCM) processing temperature) with a heating rate of 10 °C/ min, weight loss [%] was determined after 15 min of holding time (VCM processing annealing time).

4.3. Investigation of manufacturing-dependent polymer mixing

Parts of this chapter have been published in peer-reviewed research articles [83,104]. Each figure was created by the thesis author. Taking or adapting of figures is marked in the corresponding figure.

The manufacturing-dependent polymer mixing of EL 100-55: HPC-SSL (50:50) and EL 100-55: HPC-UL (50:50) was investigated by determining the T_g s of the single polymers and of the polymer blends that were obtained via VCM, HME, or SD. An overview of all measured T_g s is presented in Table 13. The DSC thermograms of the prepared EL 100-55: HPC-SSL placebo formulations, and of the neat polymers are depicted in Figure 15A. Figure 15B reveals the formulations, using HPC-UL instead of HPC-SSL, in comparison to the unprocessed single polymers.

EL 100-55 demonstrated a single and sharp T_g at 118.0 ± 0.1 °C, while in case of HPC-SSL our DSC method was not able to detect a T_g (Figure 15A). This is a well-known issue for the HPC polymers, since the very low step height of the reversing heat flow at the glass transition makes it very difficult to determine the T_g . Therefore, this investigation refers to a predicted T_g of HPC-SSL which was published to be 81.8 °C [84]. Nevertheless, the DSC thermogram of HPC-UL revealed a T_g at 81.1 ± 0.2 °C which corresponds well to the predicted T_g of 81.6 °C [84] (Figure 15B).

Regarding the processed placebo formulations, EL 100-55 and the HPC polymers demonstrated manufacturing-dependent polymer mixing.

The EL 100-55: HPC-SSL HME polymer extrudate and the EL 100-55: HPC-SSL SD demonstrated a single T_g at 88.3 ± 0.3 °C and 91.1 ± 0.8 °C, respectively. The formation of a new and intermediate T_g compared to the neat polymers indicated the formation of single-phased systems and complete polymer mixing (Figure 15A). However, the corresponding VCM formulation revealed a single T_g at 117.8 ± 0.8 °C. As this T_g was very close to the T_g of neat EL 100-55, EL 100-55-rich phases were apparently detected and a phase separated polymer blend was obtained.

By exchanging HPC-SSL with HPC-UL, the HME and SD placebo formulations demonstrated comparable polymer mixing, as single T_g s at 90.1 ± 0.6 °C (HME) and 91.7 ± 0.3 °C (SD) indicated the formation of homogeneous blends (Figure 15B). Interestingly, the DSC thermogram of the EL 100-55: HPC-UL VCM formulation showed neither the homogeneous T_g around 90 °C, nor the T_g of neat EL 100-55 around 118 °C. Instead, a

broad temperature window of the glass transition was detected and the T_g determined to be 106.1 ± 2.6 °C. Apparently, neither a pronounced immiscibility, nor a formation of a single-phased homogenous system was obtained. Lyu et al. reported shifts of the T_g s of unprocessed polymers in case of partial mixing [91]. Consequently, the DSC investigations indicated higher content of miscible phases between VCM processed EL 100-55: HPC-UL compared to VCM processed EL 100-55: HPC-SSL.

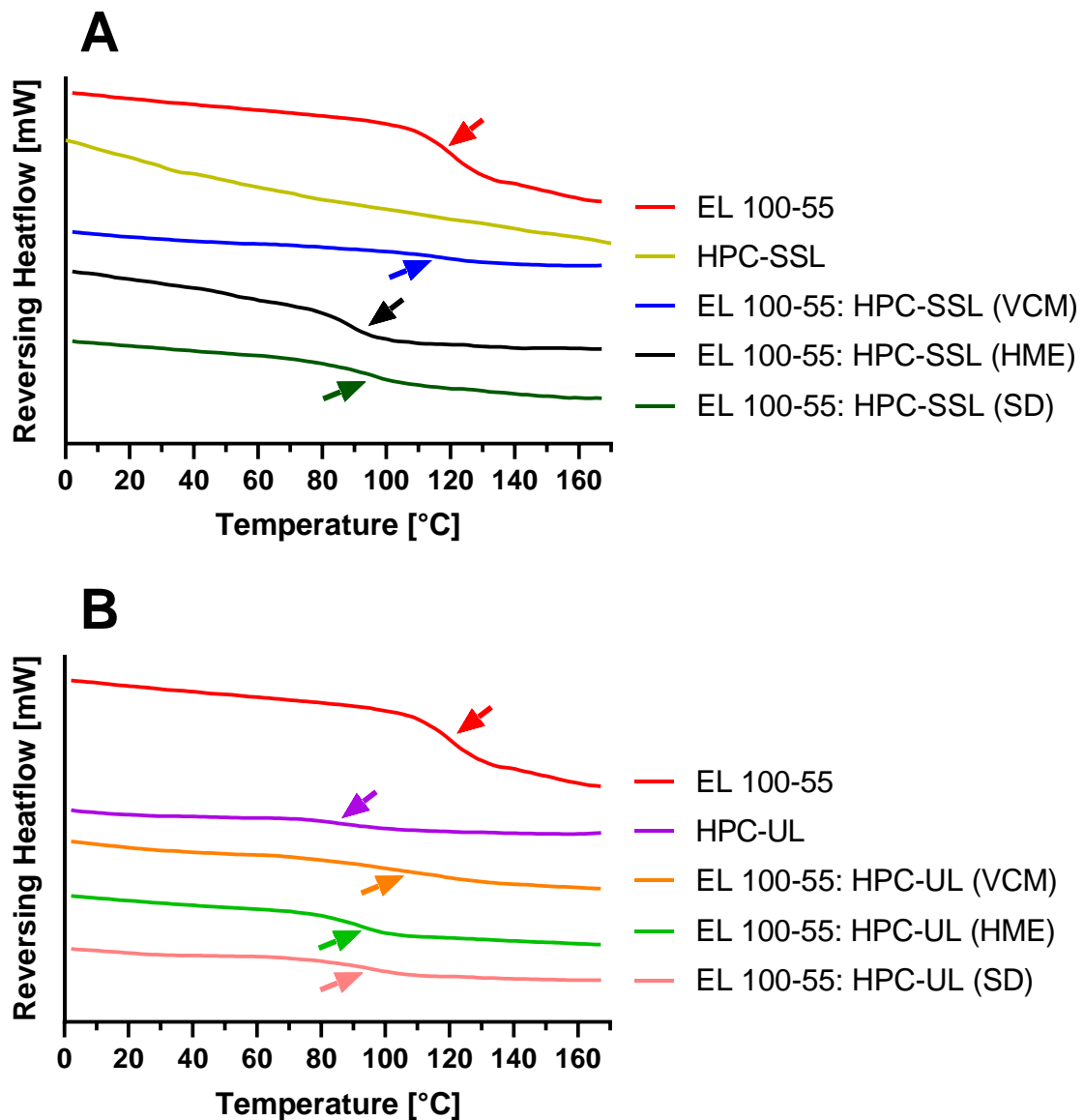


Figure 15: Differential scanning calorimetry (DSC) thermograms (exo up) of the neat polymers and polymer placebo formulations, comprising of EL 100-55 and HPC-SSL (A), and of EL 100-55 and HPC-UL (B). Analyses were conducted in TOPEM- mode with a constant temperature increase of 2 °C/ min from 0 °C to 170 °C. This figure was partially adapted from Pöstges et al., 2022 [83] and Pöstges et al., 2023 [104].

To underline the differences in phase behavior of the polymer mixture in dependence on the selected HPC grade after VCM processing, the corresponding DSC thermograms are presented rescaled, additionally in Figure 16.

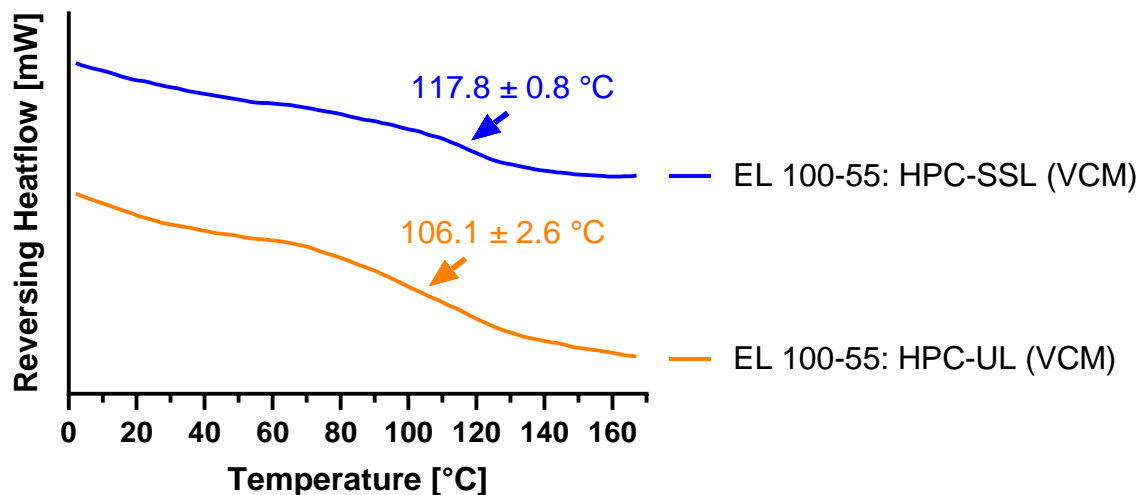


Figure 16: Rescaled differential scanning calorimetry (DSC) thermograms (exo up) of EL 100-55: HPC-SSL (VCM) and EL 100-55: HPC-UL (VCM) for highlighting the differences in the solid-state of both formulations. This figure was taken from Pöstges et al., 2023 [104].

Table 13: Glass transition temperatures (T_g s) of the neat polymers and all investigated placebo formulations. The values of the T_g s were partially taken from Pöstges et al., 2022 [83] and Pöstges et al., 2023 [104].

Polymers	Preparation method				T_g s [°C]
	unprocessed	VCM	HME	SD	
EL 100-55	X				118.0 ± 0.1
HPC-SSL	X				n/a
EL 100-55: HPC-SSL		X			117.8 ± 0.8
EL 100-55: HPC-SSL			X		88.3 ± 0.3
EL 100-55: HPC-SSL				X	91.1 ± 0.8
HPC-UL	X				81.1 ± 0.2
EL 100-55: HPC-UL		X			106.1 ± 2.6
EL 100-55: HPC-SSL			X		90.1 ± 0.6
EL 100-55: HPC-UL				X	91.7 ± 0.3

In order to confirm the results of the DSC investigations and to visualize the phase behavior of the placebo formulations, the HME formulations, as homogenous polymer blends, and

the VCM formulations, as heterogeneous polymer blends, were further characterized via CRS. Before analyzing the placebo formulations, the Raman spectra of the neat polymers were collected to identify characteristic Raman signals for distinguishing EL 100-55 and the HPC polymers in the formulations (Figure 17).

In contrast to the HPC polymers, EL 100-55 showed a characteristic peak at 1730 cm^{-1} (red arrow), hence this wavenumber was used for identifying the presence of EL 100-55. Additionally, the Raman spectra of the HPC polymers demonstrated a double peak between 2885 and 2937 cm^{-1} , whereby the front peak was suitable for imaging the distribution of HPC (blue arrows).

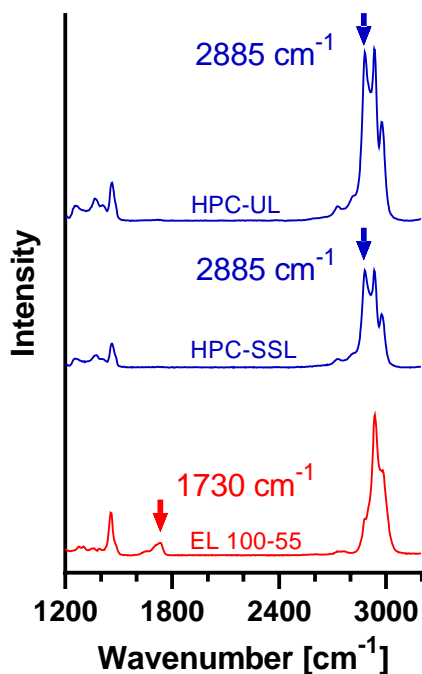


Figure 17: Single Raman spectra of neat EL 100-55, HPC-SSL, and HPC-UL for identifying characteristic Raman signals for the investigation of the placebo formulations. The utilized wavenumber for detecting the presence of the corresponding substance is presented with an arrow. This figure was adapted from Pöstges et al., 2023 [104].

Figure 18 shows arbitrary selected investigated areas of the EL 100-55: HPC-SSL formulations ($50 \times 50\ \mu\text{m}$). The images on the left side represent the EL 100-55: HPC-SSL VCM formulation and the images on the right side represent the corresponding HME placebo extrudate. In the upper images, the intensity of the peak at 1730 cm^{-1} was used for identifying the presence of EL 100-55. The color red represents high Raman intensity

at 1730 cm^{-1} and thus demonstrated the distribution of EL 100-55. Instead, the blue-colored images shows the distribution of HPC-SSL, as the intensity at 2885 cm^{-1} was used for creating the blue-colored Raman images.

Regarding the EL 100-55: HPC-SSL VCM formulation, the inconsistent red and blue color distributions as results of various Raman intensities at 1730 cm^{-1} and 2885 cm^{-1} , respectively, indicated heterogenous polymer phases. Some local areas demonstrated high content of EL 100-55, indicated by intensive red color (Figure 18A). Referring to the blue-colored image, the same areas lacked in high intensity at 2885 cm^{-1} , revealing low content of HPC-SSL, instead. The representative Raman spectrum A demonstrated similar spectral information in comparison to the Raman spectrum of neat EL 100-55 (Figure 17), indicating pronounced phase separation of EL 100-55 and HPC-SSL.

In contrast, low content of EL 100-55 was detected, when the Raman intensity at 2885 cm^{-1} for visualizing the distribution of HPC-SSL was higher, as depicted by intensive blue color (Figure 18B and Figure 18C). Interestingly, partially miscible phases were also detected, as moderate intensities at 1730 cm^{-1} and 2885 cm^{-1} were detected. Accordingly, despite the decisive phase separation of both polymers in spot A, no sharp phase separation of the polymers was detected. This could have been assumed just regarding the DSC thermograms, since the EL 100-55: HPC-SSL VCM formulation revealed a similar T_g compared to neat EL 100-55 (Figure 15).

In case of the EL 100-55: HPC-SSL HME formulation, the formation of a single-phased and homogeneous polymer mixture was confirmed. As depicted by the similar color intensities, and the representative Raman spectra (Figure 18D, Figure 18E, and Figure 18F), the consistent intensities at 1730 cm^{-1} and 2885 cm^{-1} , demonstrated complete polymer mixing and the formation of a single-phased system.

Impact of the manufacturing method on the solid-state of polymer placebo mixtures, comprising Eudragit® L 100-55 and hydroxypropyl cellulose

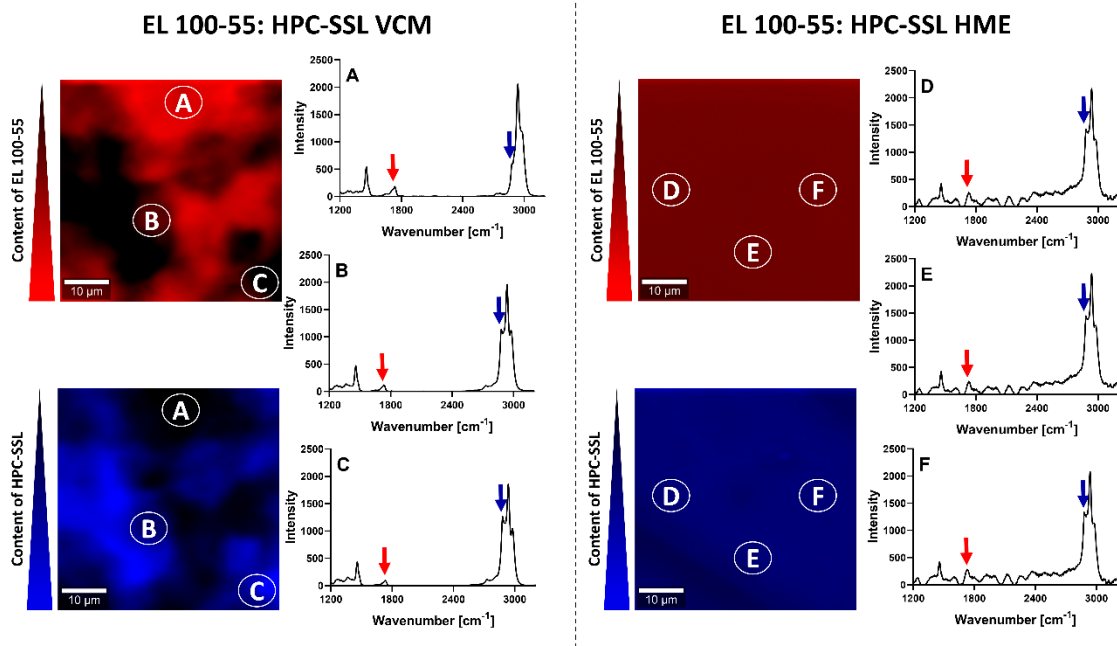


Figure 18: Confocal Raman spectroscopy (CRS) of EL 100-55: HPC-SSL placebo formulations, processed by vacuum compression molding (VCM) (A, B, C) and by hot-melt extrusion (HME) (D, E, F). The intensities at 1730 cm⁻¹ and 2885 cm⁻¹ were utilized for detecting the presence of EL 100-55 (red color) and HPC-SSL (blue color), respectively. This figure was taken from Pöstges et al., 2023 [104].

The polymer formulations, consisting of EL 100-55 and HPC-UL, revealed comparable distribution behavior compared to the EL 100-55: HPC-SSL formulations (Figure 19).

In case of VCM processed EL 100-55: HPC-UL, heterogeneous polymer phases were detected, as illustrated by the inconsistent red and blue color distribution. Aside the EL 100-55-rich phases (Figure 19A) and the HPC-UL-rich phases (Figure 19C), partially miscible phases (Figure 19B) were obtained.

The EL 100-55: HPC-UL HME formulation demonstrated comparable Raman spectra within the entire investigated area (Figure 19D, Figure 19E, Figure 19F) indicating the formation of a single-phased and homogeneous polymer mixture.

Impact of the manufacturing method on the solid-state of polymer placebo mixtures, comprising Eudragit® L 100-55 and hydroxypropyl cellulose

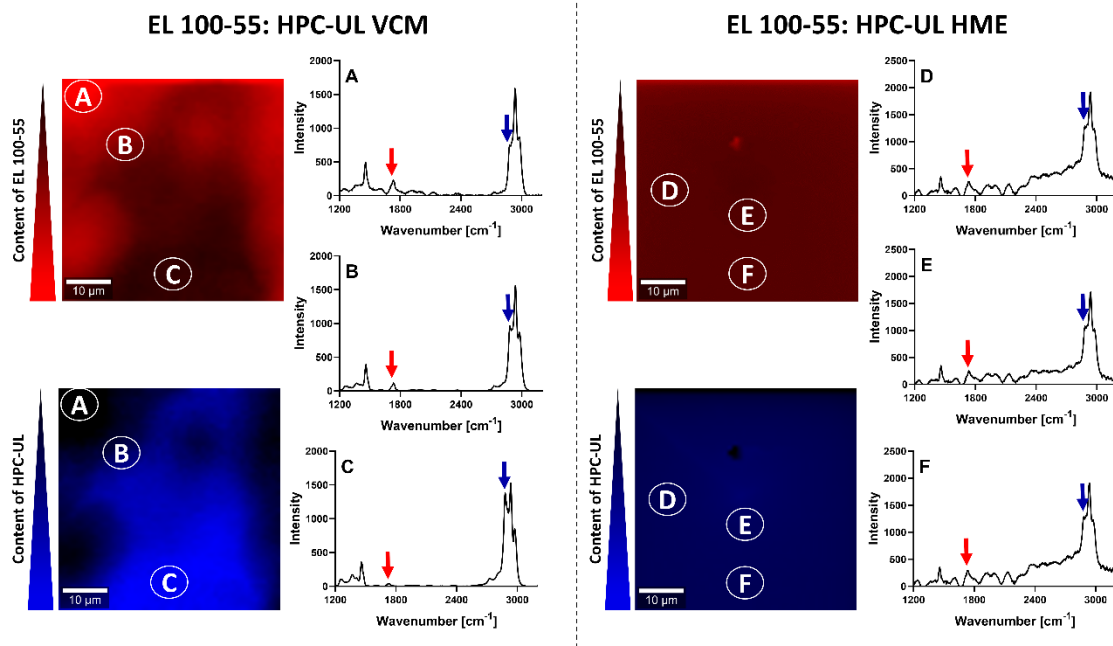


Figure 19: Confocal Raman spectroscopy (CRS) of EL 100-55: HPC-UL placebo formulations, processed by vacuum compression molding (VCM) (A, B, C) and by hot-melt extrusion (HME) (D, E, F). The intensities at 1730 cm^{-1} and 2885 cm^{-1} were utilized for detecting the presence of EL 100-55 (red color) and HPC-UL (blue color), respectively. This figure was taken from Pöstges et al., 2023 [104].

Regarding all DSC and CRS investigations of the EL 100-55: HPC polymer blends, manufacturing-dependent solid-state mixing was observed. While the solvent-based preparation method SD led to homogenous and single-phased polymer mixtures, differences between the heat-based preparation methods VCM and HME were observed. Compared to the HME process, no shear forces were applied on the molding polymer blend during VCM, thus the shear forces generated by the kneading elements in the extrusion process were apparently necessary for enabling a complete homogeneous system.

Regarding the EL 100-55: HPC VCM formulations, slight differences in the polymer mixing were observed, depending on the selection of the HPC grade. Although CRS was not able to depict differences between the ternary VCM formulations, the DSC revealed higher content of partially miscible phases in the EL 100-55: HPC-UL formulation compared to the EL 100-55: HPC-SSL formulation. Quantifying the partially miscible phases via CRS is very difficult, as the selected size of the scan might be too small and the evaluation of the color intensities for a reliable determination too inaccurate.

To find a potential explanation for the differences in the partial polymer mixing of the VCM formulations, the melt viscosities of the neat polymer at the VCM processing temperature of 160 °C were investigated.

As VCM is a non-shear method, the complex viscosities at minimal shear rate (1 rad/s) were calculated (Table 14) after performing frequency sweeps from 62.83 rad/s (10 Hz) to 0.63 rad/s (0.1 Hz) (Figure 20). All polymers demonstrated shear-thinning behavior that is a common property of polymer melts [105], as the viscosities were increased by reducing the angular frequency.

Regarding high angular frequencies EL 100-55 and HPC-SSL showed comparable complex viscosities. However, as HPC-SSL exhibited more pronounced shear-thinning character, the complex viscosities of both polymers differed decisively by decreasing the angular frequency. While EL 100-55 showed a calculated viscosity of 299,406 Pa*s at 1 rad/s, HPC-SSL exhibited a viscosity of 1,287,189 Pa*s at the same frequency (Table 14).

HPC-UL revealed a comparable shear-thinning behavior compared to HPC-SSL. However, the complex viscosities were significantly reduced for the entire frequency range, leading a calculated complex viscosity of 213,085 Pa*s at 1 rad/s. The lower MW of HPC-UL (20,000 g/mol) compared to HPC-SSL (40,000 g/mol) was likely the reason for the reduced melt viscosity, as it is well-known that the melt viscosity of one polymer group decreases with decreasing MW [106–108].

Potentially, due to the lower melt viscosity of HPC-UL compared to HPC-SSL at the VCM processing condition, higher content of partially miscible phases/ local homogeneous polymer phases between EL 100-55 and HPC were formed using the HPC grade -UL.

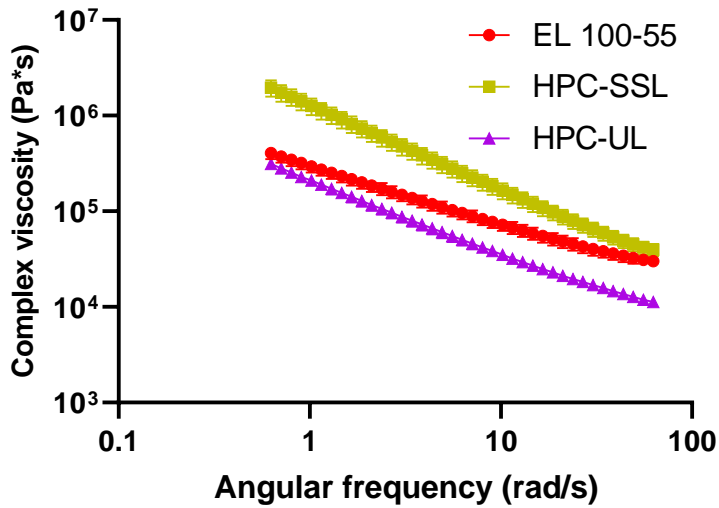


Figure 20: Frequency sweeps of the neat polymers EL 100-55, HPC-SSL, and HPC-UL at the vacuum compression molding (VCM) processing temperature of 160 °C. This figure was taken from Pöstges et al., 2023 [104].

Table 14: Calculated complex viscosities (Pa*s) at an angular frequency of 1 rad/s for the neat polymers EL 100-55, HPC-SSL, and HPC-UL at the vacuum compression molding (VCM) processing temperature of 160 °C. This table was taken from Pöstges et al., 2023 [104].

Polymer	Complex viscosity (Pa*s) at 1 rad/s
EL 100-55	299,406 ± 41,635
HPC-SSL	1,287,189 ± 252,153
HPC-UL	213,085 ± 23,830

4.4. Investigation of manufacturing-dependent polymer-polymer interactions

Parts of this chapter have been published in peer-reviewed research articles [83,104]. Each figure was created by the thesis author. Taking or adapting of figures is marked in the corresponding figure.

As the polymer blends EL 100-55: HPC-SSL (50:50) and EL 100-55: HPC-UL (50:50) revealed manufacturing-dependent polymer mixing, the polymer-polymer interactions as consequence of the different processing techniques (VCM, HME, and SD) were investigated via FT-IR. Prior to the examination of the placebo formulations, the FT-IR spectra of the neat polymers were collected. The FT-IR spectra of the processed EL 100-55: HPC-SSL polymer mixtures in comparison to the untreated PM and the single polymers are presented in Figure 21. Figure 22 depicts the FT-IR spectra of the differently processed placebo mixture, comprising EL 100-55 and HPC-UL, in comparison to the corresponding PM and neat polymers. For better visualization of the data, the spectra are split into two graphs, the lefts presenting the wavenumber from 2500 – 4000 cm^{-1} , and the rights presenting the wavenumbers from 1200 – 1800 cm^{-1} . No relevant spectral information was detected between 1800 cm^{-1} and 2500 cm^{-1} .

Regarding Figure 21, EL 100-55 demonstrated CH stretching vibrations, indicated by the peak at 2930 cm^{-1} . The double peak at 1701 cm^{-1} and 1719 cm^{-1} were attributed to the C=O stretching vibrations of the carboxylic acid groups and to the esterified carboxyl groups, respectively, whereby the peak for the carboxylic acid groups was more pronounced. The peaks between 1350 cm^{-1} and 1500 cm^{-1} corresponded to further CH vibrations.

Regarding HPC-SSL, OH vibrations led to a broad peak at 3430 cm^{-1} . The peaks at 2970 cm^{-1} were attributed to OCHX and CH vibrations.

The PM of EL 100-55: HPC-SSL revealed characteristic peaks of each polymer, as the C=O double peak of EL 100-55 and the broad OH stretching vibrations were identified in the spectrum.

Regarding the FT-IR spectra of the processed polymer blends, differences in shape and intensity of the characteristic FT-IR bands were observed. While for the VCM formulation the OH stretching vibrations of HPC-SSL were clearly visible, the intensity of the OH bands decreased distinctly after HME or SD processing.

Moreover, the C=O double peak of EL 100-55 changed in shape and intensity, dependent on the processing technique. In case of EL 100-55: HPC-SSL VCM, the peak at 1726 cm^{-1} intensified compared to the one at 1701 cm^{-1} . These observations indicated specific interactions between the carbonyl groups of EL 100-55 and HPC-SSL, but apparently without involvement of the hydroxy moiety of HPC-SSL.

Regarding the HME and SD processed EL 100-55: HPC-SSL polymer blends, changes of the bands corresponding to carbonyl moiety were more pronounced, as the peak intensities at 1701 cm^{-1} were more reduced compared to the VCM placebo. Apparently, EL 100-55 interacted strongly with HPC-SSL, whereas in contrast to the VCM formulation the hydroxy groups of HPC-SSL were involved, and the carbonyl moiety of EL 100-55 interacted even stronger.

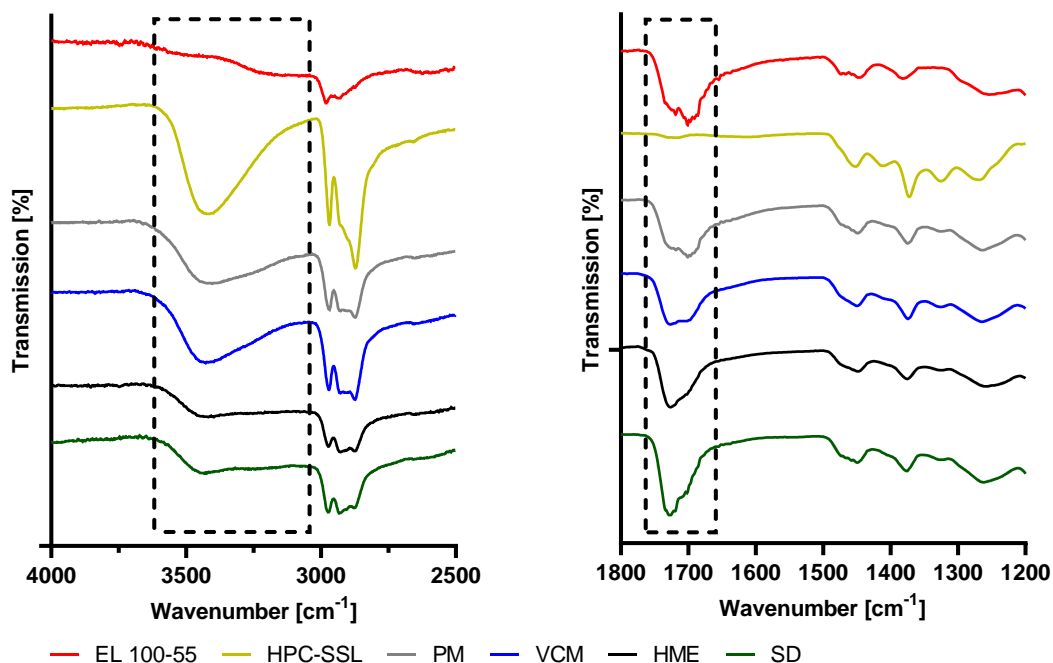


Figure 21: Fourier-transform infrared (FT-IR) spectra of the placebo formulations EL 100-55: HPC-SSL (50:50), processed via vacuum compression molding (VCM), hot-melt extrusion (HME) and spray-drying (SD), in comparison to the corresponding physical mixtures (PMs) and the neat polymers. Framing of specific bands marks region of interests. This figure was partially adapted from Pöstges et al., 2022 [83] and Pöstges et al., 2023 [104].

Compared to EL 100-55: HPC-SSL, the placebo formulations, consisting of EL 100-55 and HPC-UL, demonstrated comparable polymer-polymer interactions (Figure 22).

Again, the PM of EL 100-55: HPC-UL demonstrated the characteristic double peak for the carbonyl moiety of EL 100-55 at 1701 cm^{-1} and 1728 cm^{-1} . The OH vibrations of the hydroxy groups of HPC-UL were detected at 3430 cm^{-1} .

The polymer blends that were obtained via HME and SD, revealed stronger interactions under participation of the functional groups compared to the VCM placebo. The HME and SD processed formulations demonstrated pronounced interactions under participation of the hydroxy groups of HPC-UL and of the carbonyl groups of EL 100-55, as the intensity of the OH band at 3430 cm^{-1} was strongly decreased and the shape of the double peak changed, respectively. Instead, the FT-IR spectrum of the EL 100-55: HPC-UL VCM formulation revealed weaker polymer-polymer interaction, as the shape of the C=O band of EL 100-55 underwent smaller change and participation of the OH groups of HPC-UL could not be observed.

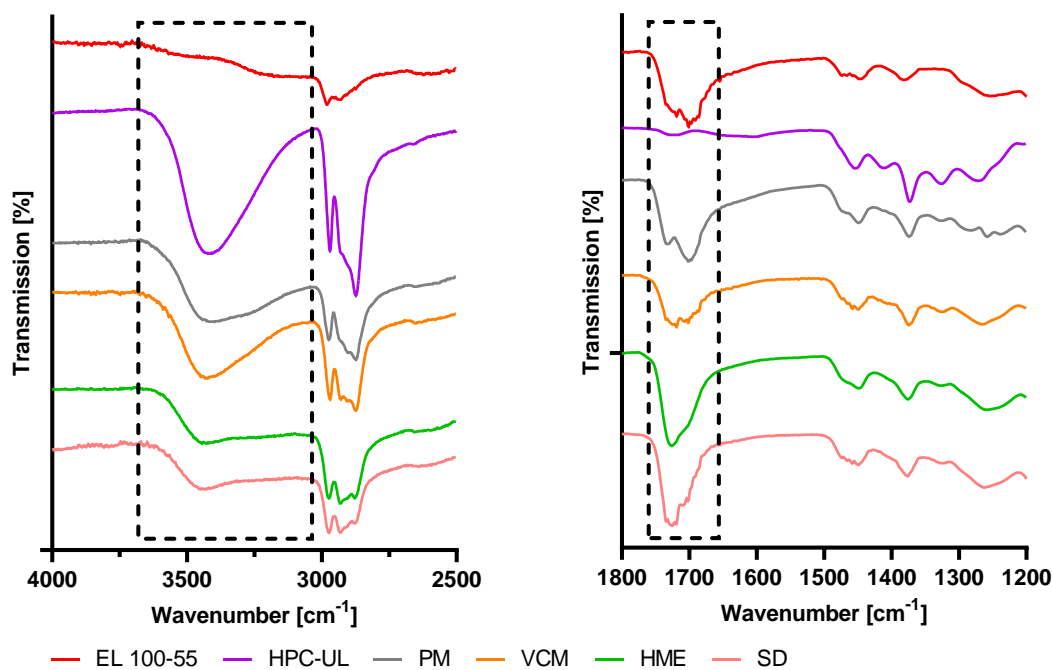


Figure 22: Fourier-transform infrared (FT-IR) spectra of the placebo formulations EL 100-55: HPC-UL (50:50), processed via vacuum compression molding (VCM), hot-melt extrusion (HME) and spray-drying (SD), compared to the corresponding physical mixtures (PMs) and the neat polymers. Framing of specific bands marks region of interests. This figure was partially adapted from Pöstges et al., 2023 [104].

4.5. Conclusion

Investigating the solid-state characteristics of the VCM, HME, and SD processed polymer mixtures of EL 100-55 and HPC (50:50), manufacturing-dependent differences in polymer mixing and polymer-polymer interactions were revealed.

Single-phased and homogeneous polymer systems were obtained after the HME and SD process. Instead, due to the missing shear forces, the VCM processed polymer formulations revealed heterogeneous character, whereby the combination including HPC-SSL demonstrated more pronounced phase separation compared to the combination including the HPC grade -UL. Apparently, the lower melt viscosity of HPC-UL under the selected VCM processing facilitated easier formation of local partially miscible phases.

As consequence of the manufacturing-dependent polymer mixing, differences in extent of polymer-polymer interactions between EL 100-55 and HPC were detected. Strongest intermolecular interactions under participation of the hydroxy groups of HPC and the carbonyl moiety of EL 100-55 were revealed in case of single-phased polymer mixing, when the polymers were processed via HME or SD. Weaker polymer-polymer interactions were determined within the phase-separated VCM processed formulations, instead.

5. Interactions between Eudragit® L 100-55 and hydroxypropyl cellulose in solid-state and dissolution of ternary amorphous solid dispersions using celecoxib and efavirenz as model drugs

5.1. Introduction

In early ASD formulation development, the optimal ASD-forming polymer needs to be selected, carefully [19]. One of the main goals is to enable excellent dissolution performance of the poorly soluble drug for maximum benefit in bioavailability enhancement [20,109].

The supersaturation assay, as promising preliminary tool for first insights into the precipitation inhibiting effects of polymers on the supersaturated state of drugs in liquid-state, was already presented in detail (chapter 2.1.). Besides the challenge to find a suitable polymer for supersaturation stabilization, it must be considered that the ideal polymer to maintain supersaturation in aqueous medium is not necessarily the optimal polymer to form a homogeneous and stable ASD. In this context Wlodarski et al. identified polyvinyl alcohol (PVA) as promising precipitation inhibitor of the poorly soluble drug itraconazole. However, due to limited miscibility of the drug and PVA in solid-state, the dissolution of the processed ASDs did not lead to the desirable solubility enhancement of the drug [110].

Moreover, for an optimal dissolution performance, the polymer should not only be capable to stabilize the supersaturation state successfully over a long period of time, but also generate rapidly the supersaturated solution [111]. If the dissolution of the processed ASD provides insufficient dissolution rate, the capability for precipitation inhibition is negligible. The drug-polymer combination CXB: HPMCAS is a representative example for this issue. As already demonstrated in the chapter of the supersaturation screening (chapter 2.2.) HPMCAS revealed high potential in stabilizing a supersaturated solution of CXB. This observation corresponds well to an investigation of Monschke et al. However, despite the pronounced potential, the authors observed low concentrations of CXB upon dissolution of processed HPMCAS ASDs. Potentially, due to high degree of swelling and decreased drug-polymer interactions as result of water-induced phase separation, the full potential of this drug-polymer system could not be realized. Instead, Monschke et al. observed fast dissolution rate of CXB when processed with PVA. However, using this

polymer, the supersaturated state could not be stabilized sufficiently, leading to early precipitation [65].

Consequently, in some cases, as either a high initial dissolution rate or a promising precipitation inhibition cannot be achieved upon dissolution, one single polymer is not able to fulfill both requirements for being an ideal supersaturating ASD-forming polymer [112,113].

To overcome this challenge, a current trend is the combination of two polymers, leading to ternary systems. Such ternary systems can be obtained by embedding the drug into the supersaturation generating polymer and adding externally the precipitation inhibiting polymer to the processed solid dispersion [114,115].

In case of the prior mentioned study of Monschke et al., superior dissolution results were obtained by processing the fast-dissolving binary CXB: PVA ASD and adding externally the precipitation inhibitor HPMCAS [65].

Another possibility is to prepare ternary ASDs by incorporating the second polymer into the ASD matrix, hence both polymers are used as ASD-forming polymers [114–116]. Previous investigations on ternary ASDs demonstrated the benefit of ternary ASDs in terms of solubility improvement and supersaturation stabilization compared to the corresponding binary formulations [117–119].

Butreddy et al. observed high initial drug release by dissolving a binary nifedipine: HPMCAS L ASD. However, HPMCAS L was not suitable to prevent rapid precipitation, thus optimization of the formulation was required. By processing ternary ASDs, including either additional HPMCAS H or Eudragit® FS100, the supersaturated state of nifedipine was maintained for a significant longer time, without decisive reduction of initial dissolution rate [120].

Zecevic et al. demonstrated the benefit of adding HPC-SSL to a dipyridamole HPMCAS ASD for enabling enhanced dissolution. Fast drug release of dipyridamole at low pH was controlled by HPC-SSL, while HPMCAS prevented precipitation of the supersaturated state after pH change to 5.5 and 6.8 [121].

However, an explicit assignment of the single polymers in ternary mixtures to be either responsible for the initial release or the inhibition of precipitation is not applicable for all systems. Prasad et al. reported synergistic interactions between EPO and PVP K90 for the

low soluble drug indomethacin, resulting in increased concentrations of the dissolved drug for approx. 2 h compared to the corresponding binary ASDs [122].

The synergistic interactions between EL 100-55 and HPC in liquid-state for enhanced extent and stabilization of supersaturation of CXB, EFV, and CLT was already revealed in chapter 2.3. and 3.2. Consequently, the aim of this study was to extend the investigations of the synergistic interactions by processing the polymers (EL 100-55 combined with HPC-SSL or HPC-UL in a 50:50 mass ratio) with either CXB or EFV to ternary ASDs.

In a first step, binary CXB and EFV ASDs (10% drug load) were obtained by processing the drugs with the single polymers via VCM. As chapters 4.3. and 4.4. demonstrated manufacturing-dependent polymer mixing and polymer-polymer interactions between EL 100-55 and HPC-SSL / -UL, ASDs of the same compositions (10% drug load and 50:50 polymer mass ratio) were prepared via VCM, HME and SD. To combine both heat-based preparation methods, additional ternary ASDs were processed via VCM, whereby the pre-extruded polymer placebo formulations EL 100-55: HPC-SSL HME (50:50) and EL 100-55: HPC-UL HME (50:50) were used as ASD-forming polymers. Solid-state of binary and ternary ASDs were investigated via X-Ray powder diffraction (XRPD), DSC and IR. Drug distributions in phase separated ternary ASDs were examined via CRS. Explanations for the observed drug distributions were found via determining the maximum kinetic solid-state solubilities of the drugs within the single polymers. Finally, non-sink dissolution testing was performed to evaluate the potential benefit of ternary ASDs compared to the corresponding binary ASDs. Furthermore, the impact of the manufacturing method of the ternary ASDs on the dissolution performance was elucidated [83,104].

5.2. Solid-state characterization of neat drugs prior to amorphous solid dispersions processing

Parts of this chapter have been published in peer-reviewed research articles [83,104]. Each figure was created by the thesis author. Taking or adapting of figures is marked in the corresponding figure.

Prior to the investigations of the ASDs, the crystalline nature of neat CXB and EFV were examined via XRPD and DSC.

The XRPD diffractogram of unprocessed CXB demonstrated sharp reflection peaks (Figure 23A) and the DSC thermogram revealed a sharp melting peak at 162.0 ± 0.3 °C (Figure 23B), confirming the crystalline character of the unprocessed drug.

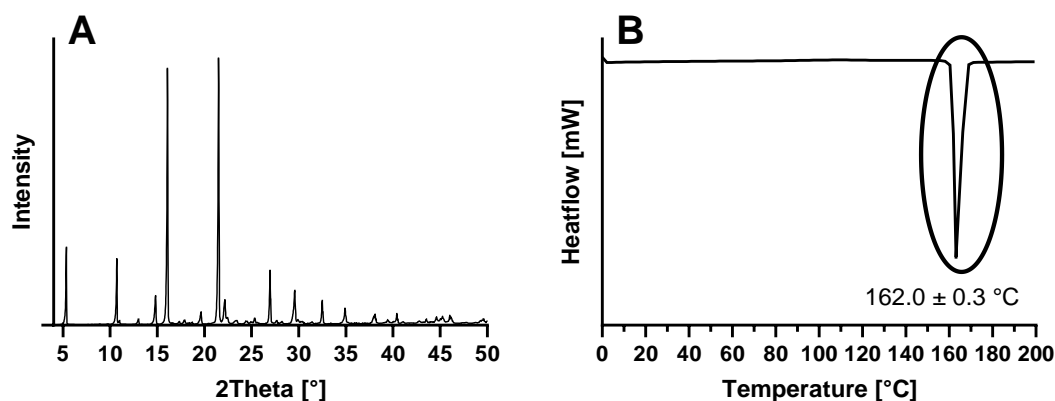


Figure 23: X-Ray powder diffraction (XRPD) diffractogram (A) and differential scanning calorimetry (DSC) thermogram (exo up) (B) of neat celecoxib (CXB). Figure A was adapted from Pöstges et al., 2022 [83].

Similar results were obtained for neat EFV, as the crystalline material caused sharp reflection peaks in the XRPD (Figure 24A). The melting point of unprocessed EFV was determined to be 137.8 ± 0.1 °C (Figure 24B).

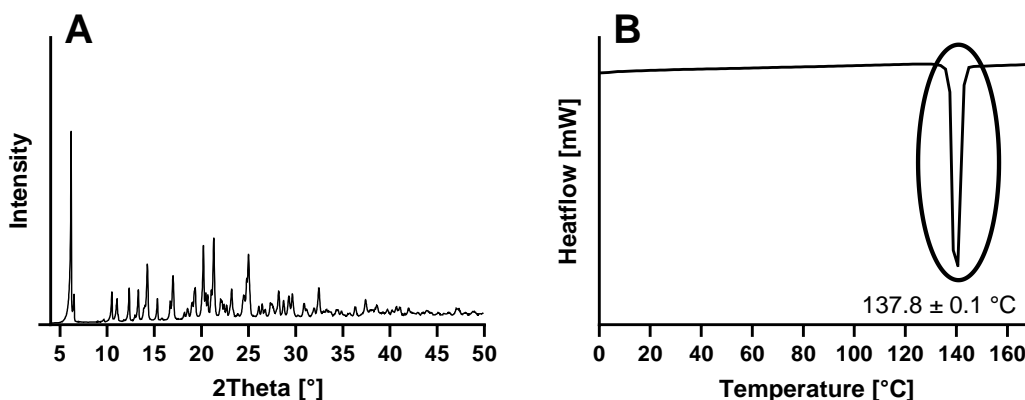


Figure 24: X-Ray powder diffraction (XRPD) diffractogram (A) and differential scanning calorimetry (DSC) thermogram (exo up) (B) of neat efavirenz (EFV). This figure was adapted from Pöstges et al., 2023 [104].

Providing drug-polymer miscibility, the selected processing conditions for VCM (160 °C for 15 min) and HME (maximum barrel temperature of 150 °C) that have already been used for processing of the polymer placebo formulations (chapter 4.) seemed to be suitable for the amorphous conversion and embedding of the drugs into the polymer matrices.

Depending on the extent of melting point depression of the processed drug, processing temperatures below the drug's melting point still lead to complete amorphous systems [25,123]. Additionally, shear forces and viscous dissipation during the HME process enables intensive distributive mixing even at lower barrel temperature [24]. Therefore, the slightly higher melting point of CXB should not cause residual crystallinity. In order to assure the avoidance of decompensation processes, thermostability of the drugs for the maximum temperature exposure of 160 °C for 15 min was investigated.

Interactions between Eudragit® L 100-55 and hydroxypropyl cellulose in solid-state and dissolution of ternary amorphous solid dispersions using celecoxib and efavirenz as model drugs

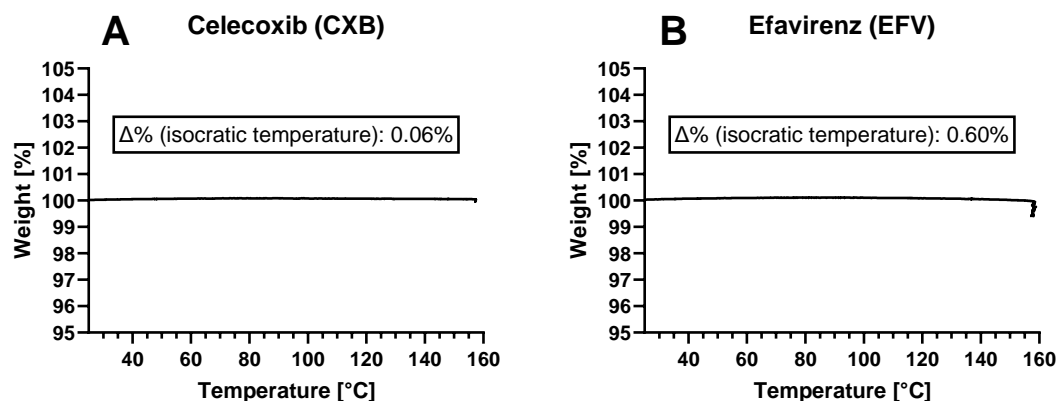


Figure 25: Thermogravimetric analysis (TGA) of neat celecoxib (CXB) (A) and neat efavirenz (EFV) (B). After heating to 160 °C (vacuum compression molding (VCM) processing temperature) with a heating rate of 10 °C/ min, weight loss [%] was determined after 15 min of holding time (VCM processing annealing time).

As presented in Figure 25, both CXB and EFV demonstrated only a minimum weight loss of 0.06% and 0.60%. As thermal stability of the polymers was confirmed in chapter 4.2., adaption of the VCM (160 °C for 15 min) and HME (maximum barrel temperature of 150 °C) processing conditions compared to the polymer placebo formulations was not required.

5.3. Solid-state characterization of celecoxib and efavirenz amorphous solid dispersions in terms of amorphousness, homogeneity, and drug-polymer interactions

Parts of this chapter have been published in peer-reviewed research articles [83,104]. Each figure was created by the thesis author. Taking or adapting of figures is marked in the corresponding figure.

After confirming the crystalline structure of the unprocessed drugs, the binary and ternary processed ASDs (10%) that were processed via VCM, HME, or SD were investigated via XRPD to detect potential residual crystallinity or to confirm the complete conversion of the drugs into the amorphous polymorph.

The XRPD diffractograms of the binary and ternary CXB ASDs (10% drug load), comprising of EL 100-55 and/ or HPC-SSL, are depicted in Figure 26A, and the CXB ASDs, comprising of EL 100-55 and/ or HPC-UL are presented in Figure 26B.

For all investigated CXB ASDs, the reflection peaks vanished. Since amorphous materials do not provide long range order for causing reflection peaks, the results underlined the successful transformation of crystalline CXB into amorphous CXB.

Interactions between Eudragit® L 100-55 and hydroxypropyl cellulose in solid-state and dissolution of ternary amorphous solid dispersions using celecoxib and efavirenz as model drugs

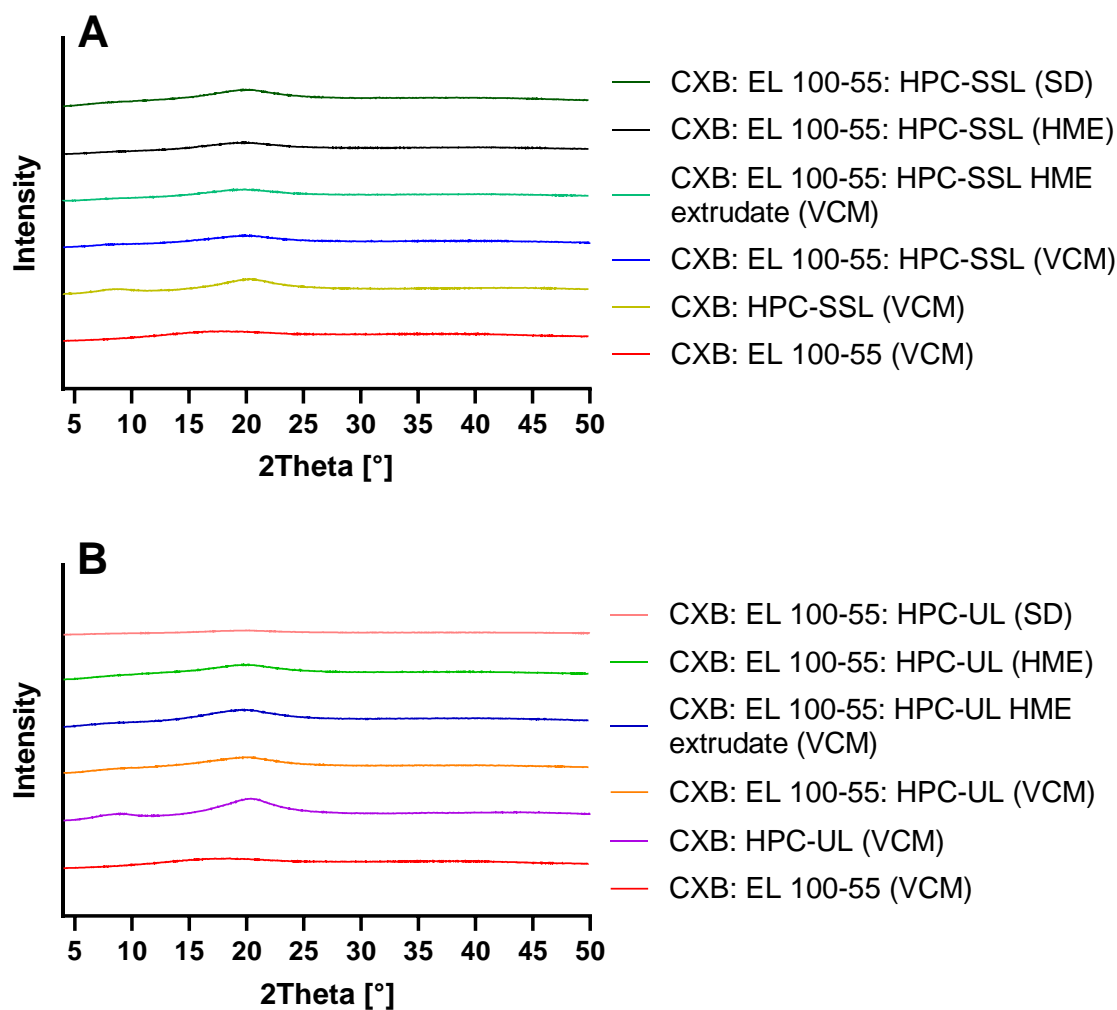


Figure 26: X-Ray powder diffraction (XRPD) diffractograms of processed celecoxib (CXB) ASDs (10% drug load): Binary and ternary ASDs, using EL 100-55 and/ or HPC-SSL as ASD-forming polymers (**A**); binary and ternary ASDs, using EL 100-55 and/ or HPC-UL as ASD-forming polymers (**B**). Figure A was partially adapted from Pöstges et al., 2022 [83].

Similar results were obtained for the EFV ASDs (10% drug load) that are depicted in Figure 27A (EL 100-55 and/ or HPC-SSL as ASD forming polymer(s)) and Figure 27B (EL 100-55 and/ or HPC-UL as ASD forming polymer(s)). In contrast to the sharp reflection peaks of unprocessed EFV (chapter 5.2.), the investigated ASDs demonstrated amorphous halo and the absence of any residual EFV crystallinity.

Interactions between Eudragit® L 100-55 and hydroxypropyl cellulose in solid-state and dissolution of ternary amorphous solid dispersions using celecoxib and efavirenz as model drugs

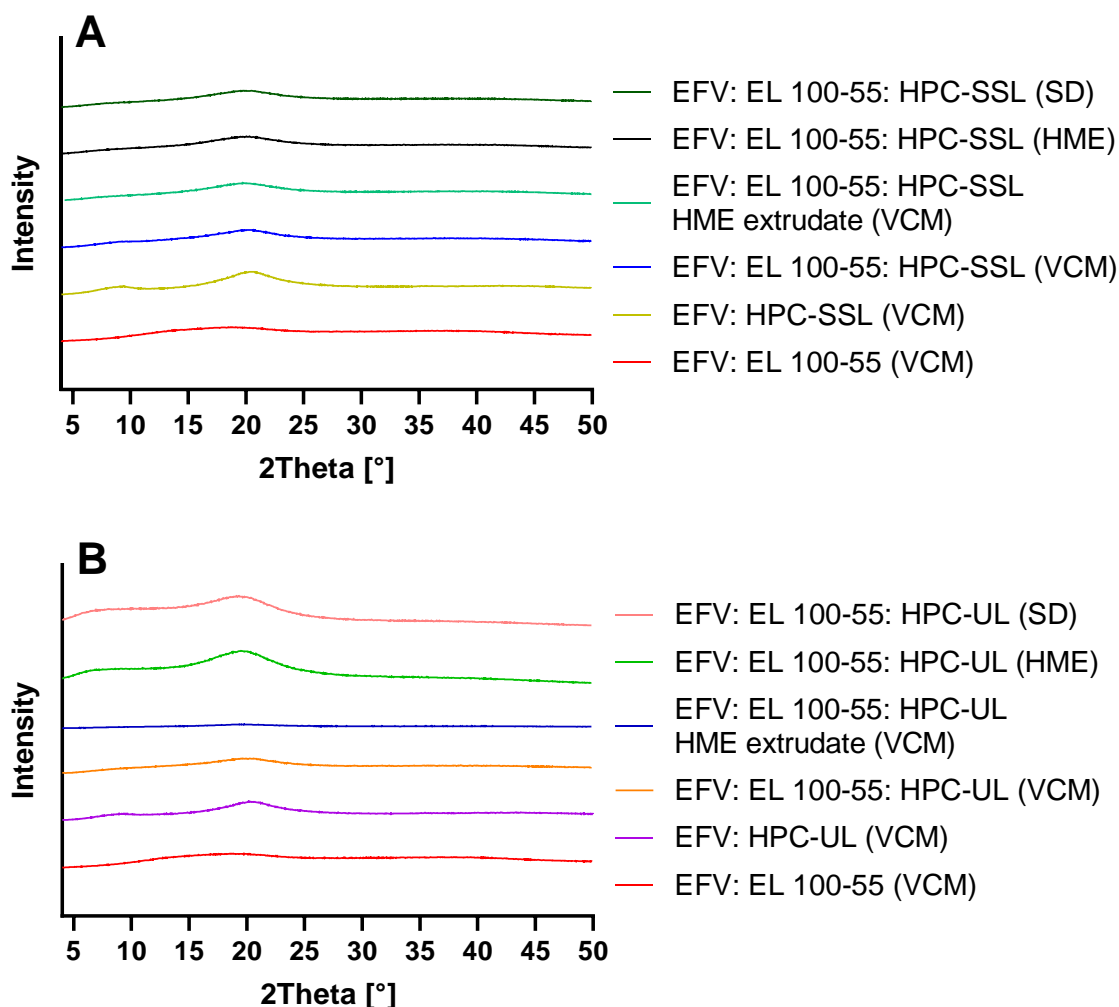


Figure 27: X-Ray powder diffraction (XRPD) diffractograms of processed efavirenz (EFV) ASDs (10% drug load): Binary and ternary ASDs, using EL 100-55 and/ or HPC-SSL as ASD-forming polymers (A); binary and ternary ASDs, using EL 100-55 and/ or HPC-UL as ASD-forming polymers (B). This figure was partially adapted from Pöstges et al., 2023 [104].

In addition to the XRPD investigations, the processed binary and ternary CXB and EFV ASDs (10% drug load) were investigated via DSC. DSC thermograms do not only provide information about residual crystallinity, but also about the phase homogeneity, depending on the appearance of the T_g s. This is especially interesting for investigating polymer mixing in ternary ASDs, as shown for the polymer placebo formulations (chapter 4.).

An overview of all detected T_g s of the investigated CXB ASDs (10% drug load) is provided in Table 15.

Figure 28A presents the DSC thermograms of the ternary CXB: EL 100-55: HPC-SSL ASDs, in comparison to the binary CXB: EL 100-55 and CXB: HPC-SSL ASDs. Due to the absence

of melting peaks, the DSC investigations confirmed the complete amorphous character of processed CXB. The T_g of the binary CXB: EL 100-55 ASD was determined to be 107.4 ± 1.1 °C. Due to the detection of only one T_g , the formation of a homogeneous and single-phased system was indicated. Similar to the DSC investigation of neat HPC-SSL, the glass transition of the CXB: HPC-SSL ASD could not be determined, as the step height of the reversing heat flow at the glass transition was too small. The investigations of the ternary ASD formulations revealed the manufacturing-dependent polymer mixing that has already been observed for the polymer placebo formulations (chapter 4.3.). For the CXB: EL 100-55: HPC-SSL ASD that was processed solely via VCM, a single T_g at 108.6 ± 1.3 °C was determined. As this T_g was very close to the T_g of the binary CXB: EL 100-55 ASD, the formation of a pronounced phase separated ternary ASD was assumed. Partially miscible phases could not be determined, as this would have caused a slight reduction of the glass transition. Instead, for the ternary VCM ASD that was prepared using the pre-extruded polymers, the T_g of processed EL 100-55 disappeared and a new single T_g at 86.1 ± 0.9 °C was detected. This indicated the formation of a homogeneous and single-phased ternary ASD. Apparently, during the molten state of the VCM process, the polymers did not segregate and remained homogeneous. The CXB: EL 100-55: HPC-SSL ASD that was solely prepared via HME showed a comparable glass transition at 86.2 ± 0.7 °C, thus the preparation of a single-phased ternary ASD was demonstrated. Regarding the CXB: EL 100-55: HPC-SSL SD ASD, the SD process also led to a single-phased and homogeneous ternary ASD, as one single T_g at 84.2 ± 0.5 °C was detected.

Figure 28B demonstrates the DSC thermograms of the binary and ternary CXB ASDs, comprising of EL 100-55 and HPC-UL, instead of HPC-SSL.

Despite the detection of a T_g for neat HPC-UL (81.1 ± 0.2 °C in chapter 4.3.), our DSC method was not able to detect the glass transition of the binary CXB: HPC-UL ASD. Regarding the ternary ASDs the manufacturing-dependent differences in polymer mixing for forming a homogeneous or heterogeneous ASD were revealed again. The ternary ASDs that consisted of extruded polymers (CXB: EL 100-55: HPC-UL HME extrudate VCM and CXB: EL 100-55: HPC-UL HME) demonstrated single T_g s at 84.3 ± 0.3 °C and 84.4 ± 0.9 °C, respectively, indicating that the exposure of heat and shear stress on the polymers via HME led to single-phased ternary ASDs. A comparable glass transition was observed for the CXB: EL 100-55: HPC-UL SD ASD (T_g of 85.8 ± 0.9 °C), demonstrating the successful

formation of a homogeneous and single-phased ternary ASD. However, regarding the CXB: EL 100-55: HPC-UL ASD that was solely prepared via VCM, evaluating the phase behavior was more challenging. The VCM ASD with the untreated polymers showed neither the T_g of the single-phased ternary ASDs around 86 °C, nor the T_g of the binary CXB: EL 100-55 around 118 °C that would indicate a complete phase separated ternary ASD. As both homogeneity and complete phase separation were not indicated, partial polymer mixing of EL 100-55 and HPC-UL was assumed. This corresponds well to the results of the polymer placebo formulations (chapter 4.3.), where the DSC also revealed higher content of partially miscible phases between EL 100-55 and the lower melt viscosity HPC grade HPC-UL, compared to EL 100-55 and HPC-SSL.

Table 15: Glass transition temperatures (T_g s) of the celecoxib (CXB) ASDs dependent on the selected processing method. The values of the T_g s were partially taken from Pöstges et al., 2022 [83].

ASD formulation (10% drug load)	Preparation method				T_g s [°C]
	VCM	VCM (HME polymers)	HME	SD	
CXB: EL 100-55	X				107.4 ± 1.1
CXB: HPC-SSL	X				n/a
CXB: EL 100-55: HPC-SSL	X				108.6 ± 1.3
CXB: EL 100-55: HPC-SSL		X			86.1 ± 0.9
CXB: EL 100-55: HPC-SSL			X		86.2 ± 0.7
CXB: EL 100-55: HPC-SSL				X	84.2 ± 0.5
CXB: HPC-UL	X				n/a
CXB: EL 100-55: HPC-UL	X				96.8 ± 1.3
CXB: EL 100-55: HPC-UL		X			84.3 ± 0.3
CXB: EL 100-55: HPC-UL			X		84.4 ± 0.9
CXB: EL 100-55: HPC-UL				X	85.8 ± 0.9

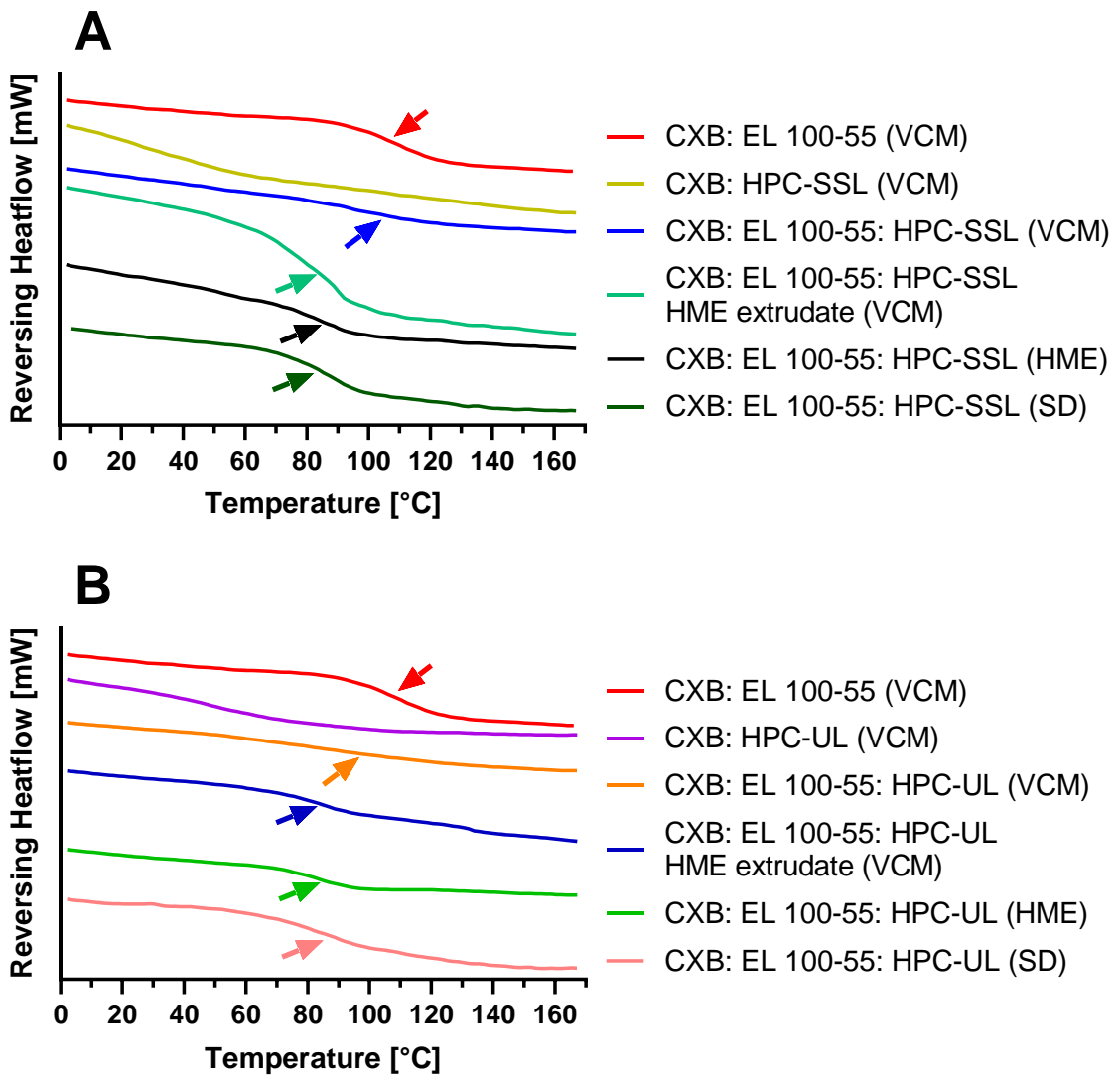


Figure 28: Differential scanning calorimetry (DSC) thermograms (exo up) of processed celecoxib (CXB) ASDs (10% drug load): Binary and ternary ASDs, using EL 100-55 and/ or HPC-SSL as ASD-forming polymers (A); binary and ternary ASDs, using EL 100-55 and/ or HPC-UL as ASD-forming polymers (B). Analyses were conducted in TOPEM- mode with a constant temperature increase of 2 °C/ min from 0 °C to 170 °C. This figure was partially adapted from Pöstges et al., 2022 [83].

For enhanced visualization between the glass transitions of the heterogeneous ternary VCM ASDs, comprising of either HPC-SSL or HPC-UL, the corresponding DSC thermograms are depicted rescaled additionally in Figure 29.

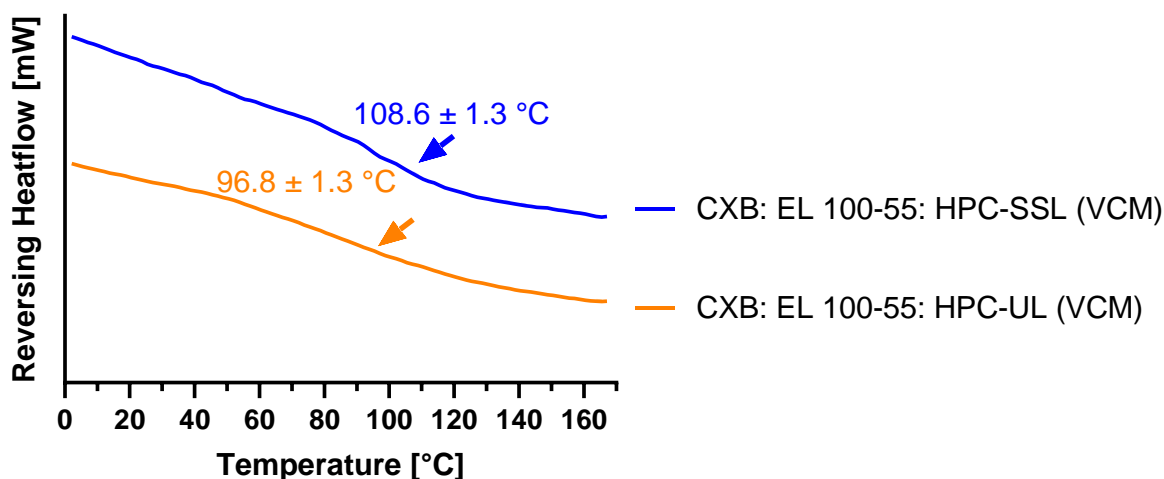


Figure 29: Rescaled differential scanning calorimetry (DSC) thermograms (exo up) of CXB: EL 100-55: HPC-SSL (VCM) and CXB: EL 100-55: HPC-UL (VCM) for highlighting the differences in the solid-state of both formulations. This figure was partially adapted from Pöstges et al., 2022 [83].

Figure 30 reveals the DSC thermograms of the binary and ternary EFV ASDs (10% drug load). An overview of the detected glass transitions within the EFV ASDs is given in Table 16. For all investigated ASDs, the melting peak of processed EFV was not visible, indicating the complete conversion from the crystalline structure into the amorphous form. For the binary EFV: EL 100-55, homogeneous and single-phased embedding of processed EFV was demonstrated, as one single T_g at 107.3 ± 0.5 °C was detected. Glass transitions of both the binary EFV: HPC-SSL ASD and the EFV: HPC-UL ASD could not be measured. Therefore, except the absence of residual crystallinity, no further assertion about the solid-states could be made.

Comparable to the ternary CXB ASDs, the selected manufacturing method and the selected HPC grade influenced the solid-states of the ternary EFV ASDs. For the EFV: EL 100-55: HPC-SSL HME ASD and the EFV: EL 100-55: HPC-UL HME ASD, single T_g s at 79.2 ± 1.0 °C and 79.6 ± 0.5 were detected, respectively, indicating single-phased ternary ASDs. Similar T_g s were obtained for the VCM ASDs with pre-extruded polymers (78.8 ± 0.3 °C for the EFV: EL 100-55: HPC-SSL HME extrudate VCM and 80.0 ± 0.6 °C for the EFV: EL 100-55: HPC-UL HME extrudate VCM), indicating similar phase behavior compared to the ASDs that were solely extruded.

However, comparable to the placebo formulations (chapter 4.3.) and the CXB ASDs, the ternary VCM ASDs with untreated polymers demonstrated different solid-states. In case of the EFV: EL 100-55: HPC-SSL VCM ASD, a similar glass transition (T_g of 107.0 ± 0.5 °C) compared to the binary EFV: EL 100-55 ASD was detected, indicating pronounced phase separation between EL 100-55 and HPC-SSL. In contrast by exchanging HPC-SSL with HPC-UL, the T_g around 107 °C disappeared, and a broad temperature window of the glass transition was revealed, instead. As the T_g was determined to be 96.8 ± 1.3 °C, neither a homogeneous, nor a pronounced phase separated system was detected, indicating the formation of additional partially miscible polymer phases. To highlight the HPC grade-dependent phase behavior of the ternary VCM ASDs, the corresponding DSC thermograms are depicted rescaled in Figure 31, additionally.

Instead, the SD process enabled the formation of single-phased ternary ASDs, as single T_g s at 80.1 ± 0.7 °C and 82.1 ± 0.5 °C were observed for EFV: EL 100-55: HPC-SSL SD and EFV: EL 100-55: HPC-UL, respectively (Figure 30).

Table 16: Glass transition temperatures (T_g s) of the efavirenz (EFV) ASDs dependent on the selected processing method. The values of the T_g s were partially taken from Pöstges et al., 2023 [104].

ASD formulation (10% drug load)	Preparation method				T_g s [°C]
	VCM	VCM (HME polymers)	HME	SD	
EFV: EL 100-55	X				107.3 ± 0.5
EFV: HPC-SSL	X				n/a
EFV: EL 100-55: HPC-SSL	X				107.0 ± 0.5
EFV: EL 100-55: HPC-SSL		X			78.8 ± 0.3
EFV: EL 100-55: HPC-SSL			X		79.2 ± 1.0
EFV: EL 100-55: HPC-SSL				X	80.1 ± 0.7
EFV: HPC-UL	X				n/a
EFV: EL 100-55: HPC-UL	X				97.7 ± 1.2
EFV: EL 100-55: HPC-UL		X			80.0 ± 0.6
EFV: EL 100-55: HPC-UL			X		79.6 ± 0.5
EFV: EL 100-55: HPC-UL				X	82.1 ± 0.5

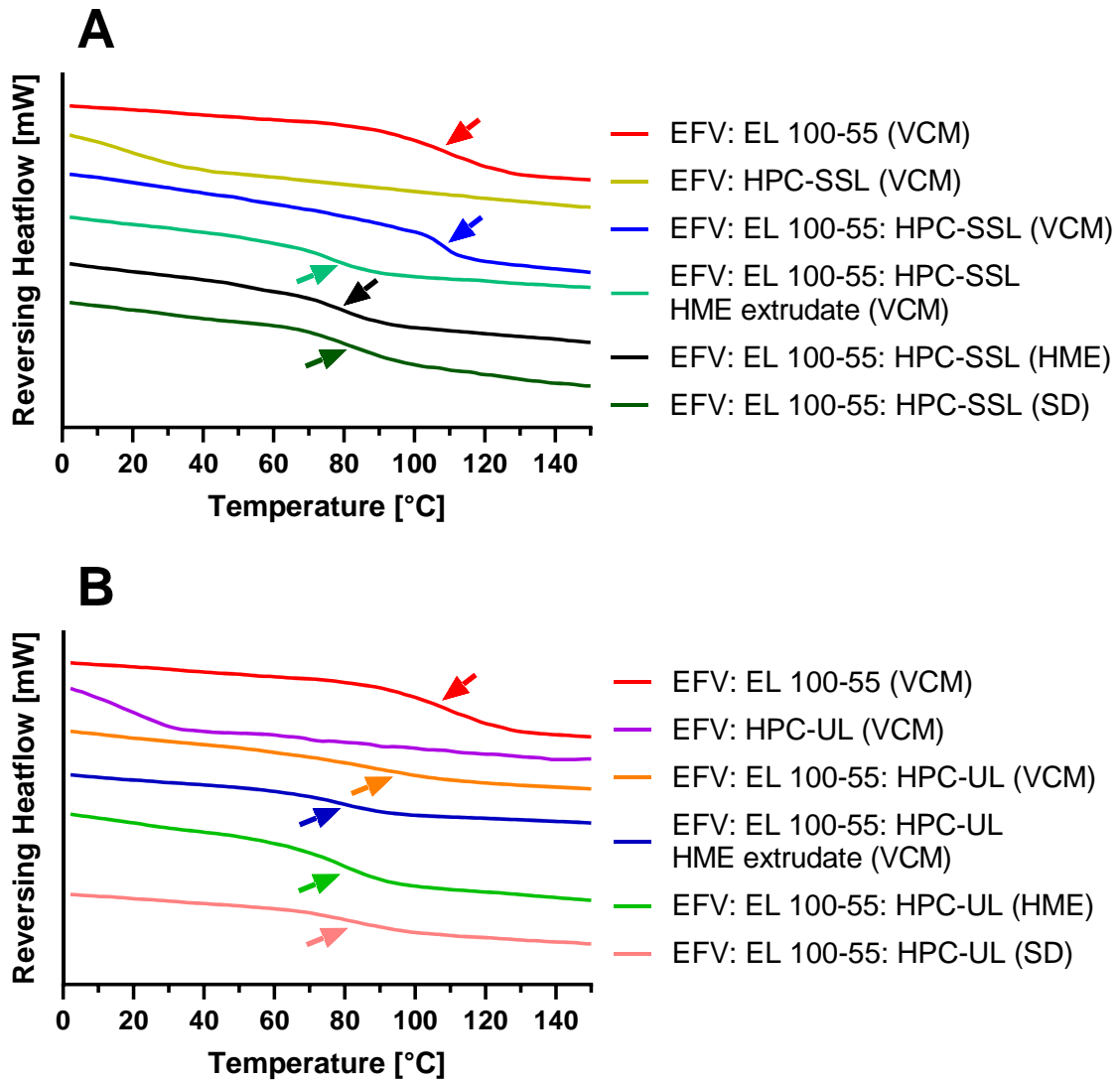


Figure 30: Differential scanning calorimetry (DSC) thermograms (exo up) of processed efavirenz (EFV) ASDs (10% drug load): Binary and ternary ASDs, using EL 100-55 and/ or HPC-SSL as ASD-forming polymers (**A**); binary and ternary ASDs, using EL 100-55 and/ or HPC-UL as ASD-forming polymers (**B**). Analyses were conducted in TOPEM- mode with a constant temperature increase of 2 °C/ min from 0 °C to 150 °C. This figure was partially adapted from Pöstges et al., 2023 [104].

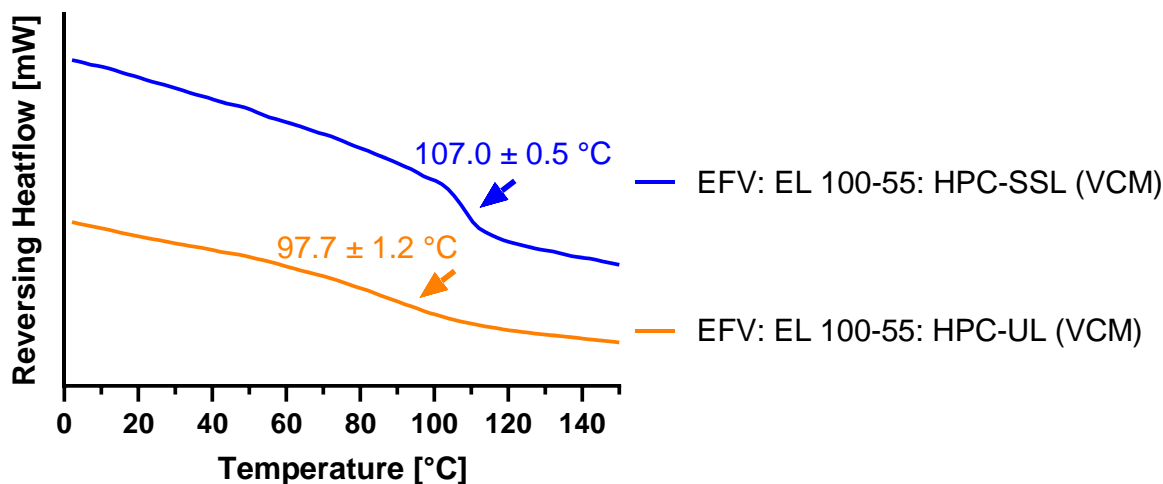


Figure 31: Rescaled differential scanning calorimetry (DSC) thermograms (exo up) of EFV: EL 100-55: HPC-SSL (VCM) and EFV: EL 100-55: HPC-UL (VCM) for highlighting the differences in the solid-state of both formulations. This figure was taken from Pöstges et al., 2023 [104].

In order to investigate drug-polymer interactions between the processed drugs and the ASD forming polymers, FT-IR measurements were conducted.

Figure 32 represents the FT-IR spectra of the binary CXB ASDs compared to the unprocessed components and the corresponding PMs. For enhanced visualization, the spectra are split, presenting the spectral range from 2500 cm^{-1} to 4000 cm^{-1} on the left side and the range from 1200 cm^{-1} to 1800 cm^{-1} on the right side of the figure. No relevant spectral information was detected between 1800 cm^{-1} and 2500 cm^{-1} .

The FT-IR spectrum of unprocessed CXB revealed NH stretching vibrations at 3333 cm^{-1} and 3227 cm^{-1} and S=O stretching vibrations at 1346 cm^{-1} , allocating to the sulfonamide structure (Figure 32). Regarding the PM of CXB: EL 100-55, the C=O stretching vibrations of the carboxylic acid groups and of the esterified carboxyl groups of EL 100-55 were observed at 1701 cm^{-1} and 1719 cm^{-1} , respectively, whereby the band at 1701 cm^{-1} was more intensified (Figure 32A). After processing the PM to an ASD, the NH bands and S=O bands of CXB completely disappeared, indicating the presence of intermolecular interactions between EL 100-55 and CXB under participation of the sulfonamide structure of CXB. However, the shape of the C=O double band did not change and only shifted slightly from 1701 cm^{-1} to 1698 cm^{-1} and from 1719 cm^{-1} to 1727 cm^{-1} . Apparently, the drug-polymer interactions occurred under only negligible participation of the carbonyl moiety of EL 100-55.

Regarding the FT-IR spectra of CXB: HPC-SSL (Figure 32B) and CXB: HPC-UL (Figure 32C), both PMs showed the broad OH band of HPC at around 3430 cm^{-1} in combination with the NH stretching vibrations of the unprocessed CXB. While the NH stretching vibrations of CXB vanished after VCM processing, the OH band did not change in shape and intensity. As the S=O bands of CXB could also not be detected in the FT-IR spectra of the HPC VCM formulations, the results indicated specific drug-polymer interactions between CXB and HPC, under strong participation of the sulfonamide structure of CXB, whereby the hydroxy groups of the HPC polymers were not involved.

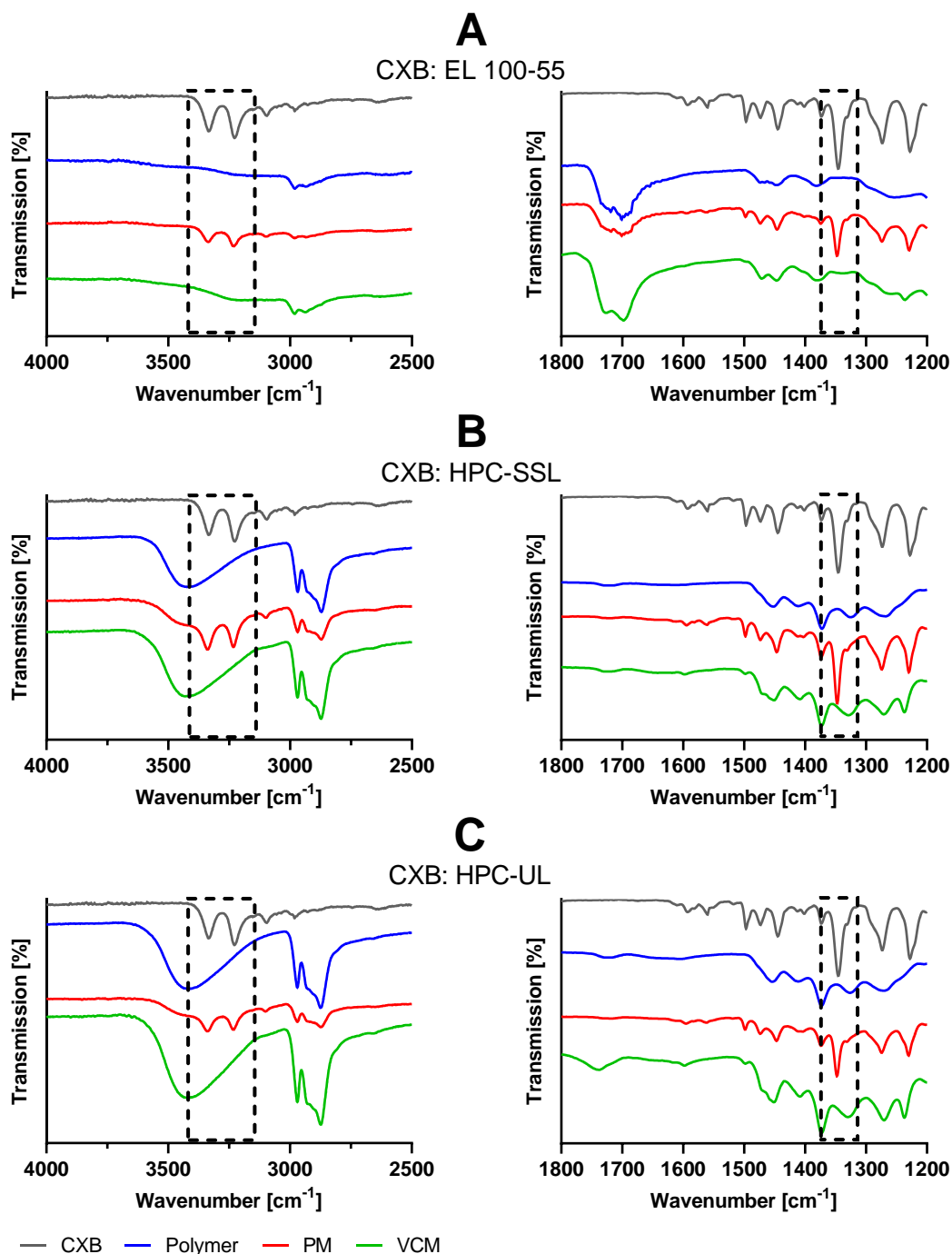


Figure 32: Fourier-transform infrared (FT-IR) spectra of the binary celecoxib (CXB) formulations: CXB: EL 100-55 (A), CXB: HPC-SSL (B) and CXB: HPC-UL (C). The ASDs are compared to neat CXB, the neat polymers and the corresponding physical mixture (PM). Framing of specific bands marks region of interests. This figure was partially adapted from Pöstges et al., 2022 [83].

Figure 33 depicts the FT-IR spectra of the differently manufactured ternary ASDs, consisting of CXB: EL 100-55: HPC-SSL (Figure 33A) and CXB: EL 100-55: HPC-UL (Figure 33B) in comparison to unprocessed raw material and the PMs.

The PM of CXB: EL 100-55: HPC-SSL revealed the sulfonamide structure of CXB (NH stretching vibrations (3337 cm^{-1} and 3231 cm^{-1}) and S=O stretching vibrations (1347 cm^{-1})), the broad OH band of HPC-SSL (around 3430 cm^{-1}), and the double band of the carboxylic acid groups (1701 cm^{-1}) and esterified carboxyl groups (1720 cm^{-1}) of EL 100-55. Comparable to the binary formulations, all ternary EL 100-55: HPC-SSL ASDs demonstrated drug-polymer interactions, involving the sulfonamide structure of the drug, as both NH stretching bands and the S=O band vanished.

Moreover, manufacturing-dependent changes in the polymer bands were observed. For the ternary VCM ASD, the broad band at 3430 cm^{-1} was still detectable, while the C=O double peak changed in shape and the peak at 1726 cm^{-1} intensified compared to the one at 1701 cm^{-1} . For the ternary ASDs with extruded polymers (CXB: EL 100-55: HPC-SSL HME extrudate (VCM) and CXB: EL 100-55: HPC-SSL (HME)) and the ternary SD ASD, the broad OH band lost strongly in intensity and the changes of the bands corresponding to carbonyl moiety were even more pronounced compared to the ones of CXB: EL 100-55: HPC-SSL VCM formulation (Figure 33A).

However, the changes in the polymer bands were attributed to the manufacturing-dependent specific polymer-polymer interactions that were observed in the FT-IR spectra of the placebo formulations (chapter 4.4.). Accordingly, further interactions between the polymers and CXB with participation of hydroxy and carbonyl moiety of the polymers could not be determined.

Similar results were obtained, investigating the ternary formulations of CXB, EL 100-55 and HPC-UL (Figure 33B). Regarding the PM of CXB: EL 100-55: HPC-UL, the functional groups of the individual components were detected again and ASD processing led to drug-polymer interactions under participation of the sulfonamide structure of CXB. Similar to the CXB: EL 100-55: HPC-SSL ASDs, further changes of the polymer bands were attributed to manufacturing-dependent polymer-polymer interactions (chapter 4.4.).

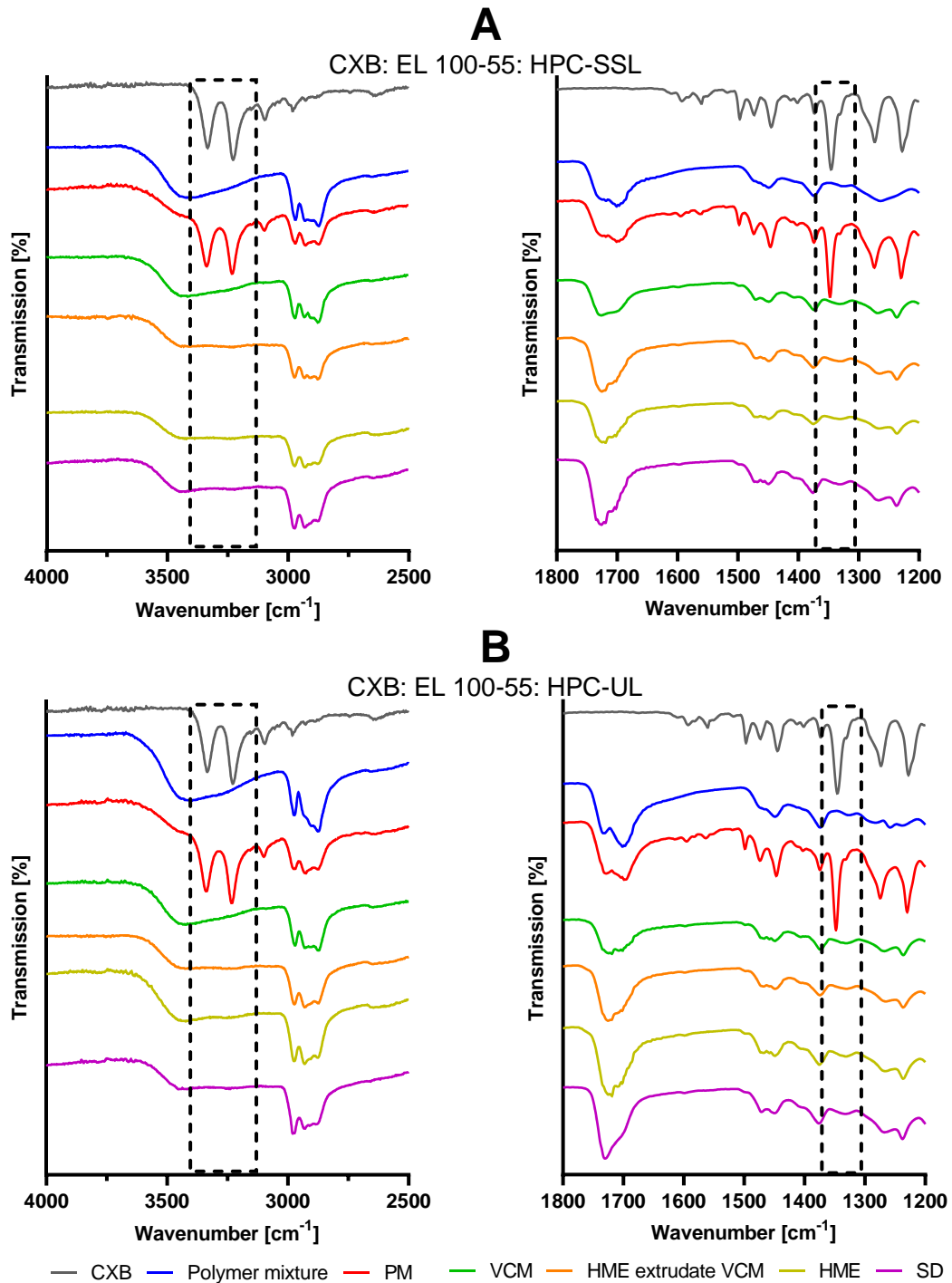


Figure 33: Fourier-transform infrared (FT-IR) spectra of the differently processed ternary celecoxib (CXB) ASDs via vacuum compression molding (VCM), polymer extrudate VCM, hot-melt extrusion (HME), and spray-drying (SD): CXB: EL 100-55: HPC-SSL (**A**) and CXB: EL 100-55: HPC-UL (**B**). The ASDs are compared to neat CXB, the corresponding unprocessed polymer mixture EL 100-55: HPC (50:50) and the corresponding physical mixture (PM) CXB: EL 100-55: HPC (10:45:45). Framing of specific bands marks region of interests. This figure was partially adapted from Pöstges et al., 2022 [83].

Figure 34 depicts the relevant FT-IR spectra ranges (from 2200 cm^{-1} to 4000 cm^{-1} on the left side, and from 1150 cm^{-1} to 1800 cm^{-1} on the right side) of the binary EFV: EL 100-55 (Figure 34A), EFV: HPC-SSL (Figure 34B) and EFV: HPC-UL (Figure 34C) ASDs, compared to the corresponding PMs and unprocessed EFV. Between 1800 cm^{-1} and 2200 cm^{-1} no relevant spectral information was revealed.

The spectrum of neat EFV demonstrated NH stretching vibrations at 3311 cm^{-1} . C=O stretching vibrations and C-O vibrations were detected at 1744 cm^{-1} and 1184 cm^{-1} , respectively. The peak at 2249 cm^{-1} was attributed to C \equiv C stretching vibrations and the unspecific C=C vibrations of the benzene ring were detected at 1600 cm^{-1} and 1494 cm^{-1} . In contrast to the PM of EFV and EL 100-55, the spectrum of the corresponding ASD did not demonstrate the NH stretching vibrations and the C-O stretching vibrations, indicating intermolecular interactions between embedded EFV and EL 100-55 under participation of these functional groups (Figure 34A). Moreover, the C \equiv C stretching vibrations and the C=C stretching vibrations of the benzene ring of processed EFV lost intensity, assuming further hydrophobic interactions between drug and EL 100-55.

The PMs of EFV: HPC-SSL and EFV: HPC-UL demonstrated the sharp NH peak of EFV (3311 cm^{-1}) in combination with the broad OH band of the HPC polymers (Figure 34B and Figure 34C). The C=O, C-O, C \equiv C, and the C=C stretching vibrations of the benzene ring that were observed in unprocessed EFV were still clearly detectable. After VCM processing, both HPC-SSL and HPC-UL executed intermolecular interactions with the NH and C-O moieties of EFV, as the corresponding peaks vanished completely. Shifts of the IR band from 1747 cm^{-1} to 1755 cm^{-1} indicated additional interactions including the C=O of EFV. In contrast to the FT-IR spectrum of the EFV: EL 100-55 ASD, the HPC ASDs demonstrated detectable C \equiv C stretching vibrations (2251 cm^{-1}) and C=C vibrations (1603 cm^{-1} and 1497 cm^{-1}). Apparently, the triple bond and the benzene structure of EFV were not involved in the intermolecular interactions with the HPC polymers. As the OH bands of the polymers did not change in shape and intensity, no indication for the participation of the OH groups of the HPC polymers in the intermolecular interactions is given.

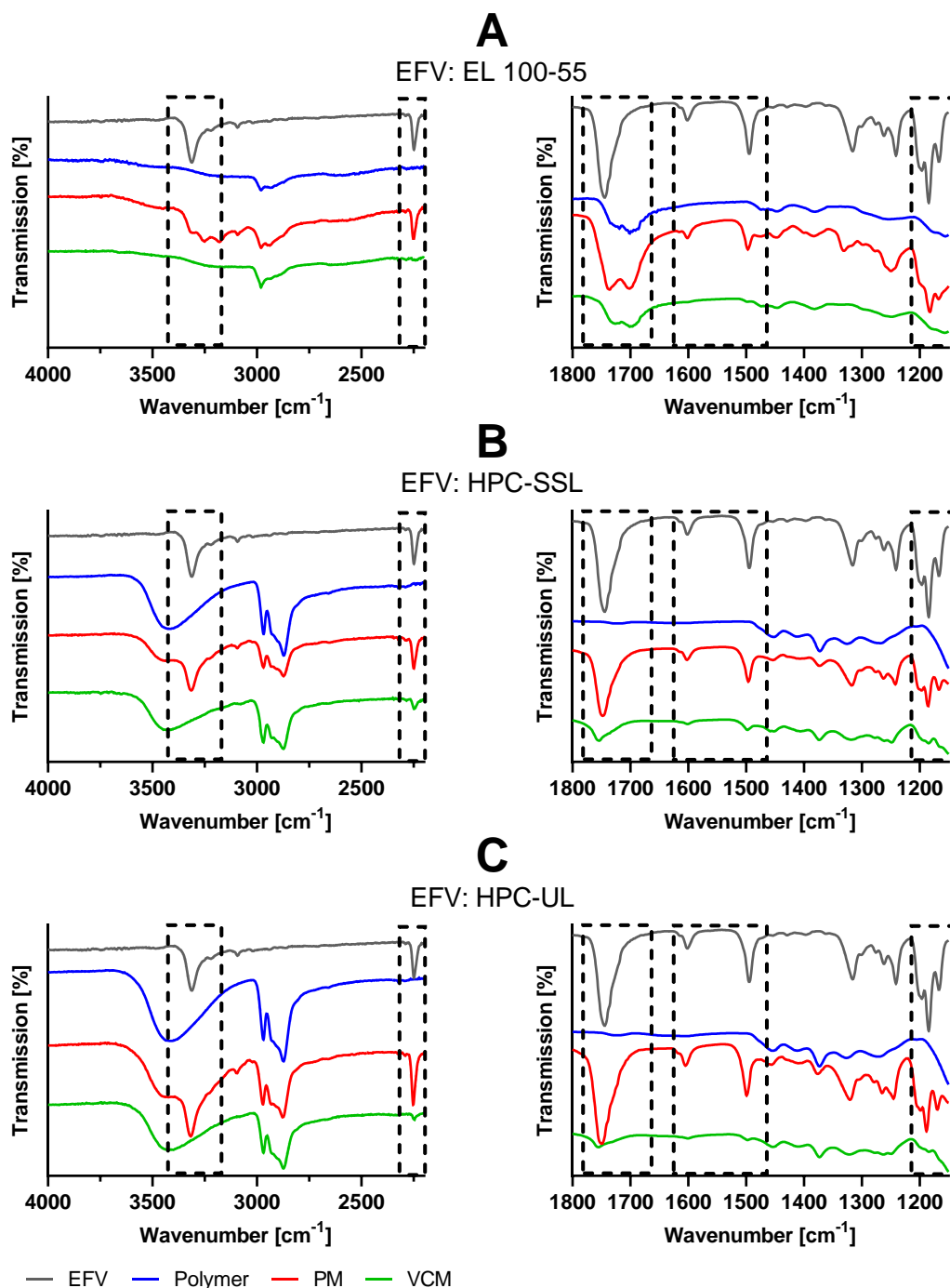


Figure 34: Fourier-transform infrared (FT-IR) spectra of the binary efavirenz (EFV) formulations: EFV: EL 100-55 (A), EFV: HPC-SSL (B) and EFV: HPC-UL (C). The ASDs are compared to neat EFV, the neat polymers and the corresponding physical mixture (PM). Framing of specific bands marks region of interests. This figure was adapted from Pöstges et al., 2023 [104].

The FT-IR spectra of the ternary EFV: EL 100-55: HPC-SSL ASDs and of the ternary EFV: EL 100-55: HPC-UL ASDs are presented in Figure 35A and Figure 35B, respectively.

Comparable to the binary ASDs, the FT-IR spectra of the ternary ASDs revealed intermolecular drug-polymer interactions. Independently of the selected manufacturing method the stretching vibrations of NH and C-O of embedded EFV were not detected and the shape of the C=O vibrations changed. The C≡C stretching vibrations and C=C vibrations of EFV were still visible, but lost decisively in intensity, revealing the participation in the solid-state interactions with the polymer mixtures. Due to the investigations of the binary ASDs, the interactions with the triple bond and the benzene structure of EFV were mainly attributed to the polymeric structure of EL 100-55. Similar to the CXB ternary ASDs, the OH bands of the polymer extrudate VCM, HME, and SD ternary ASDs revealed reduced intensity, while the VCM ASDs with untreated polymers demonstrated unchanged OH stretching vibrations. The reduction of the intensity of the OH bands and the additional manufacturing-dependent extent of changes in shape of the C=O double peak were attributed to polymer-polymer interactions between EL 100-55 and HPC (see chapter 4.4.). Further interactions between the polymers and EFV with participation of the OH groups (HPC) and carbonyl moiety (EL 100-55) of the polymers could not be detected. Connecting all FT-IR results with the corresponding DSC investigations, the impact of phase homogeneity on the formation of the solid-state interactions was revealed.

Although the FT-IR results did not show manufacturing-dependent interactions between drugs and polymers, the polymers themselves demonstrated stronger polymer-polymer interactions in case of homogeneous formation (HME and SD). Heterogeneous ternary ASDs after VCM showed weaker polymer-polymer interactions, instead.

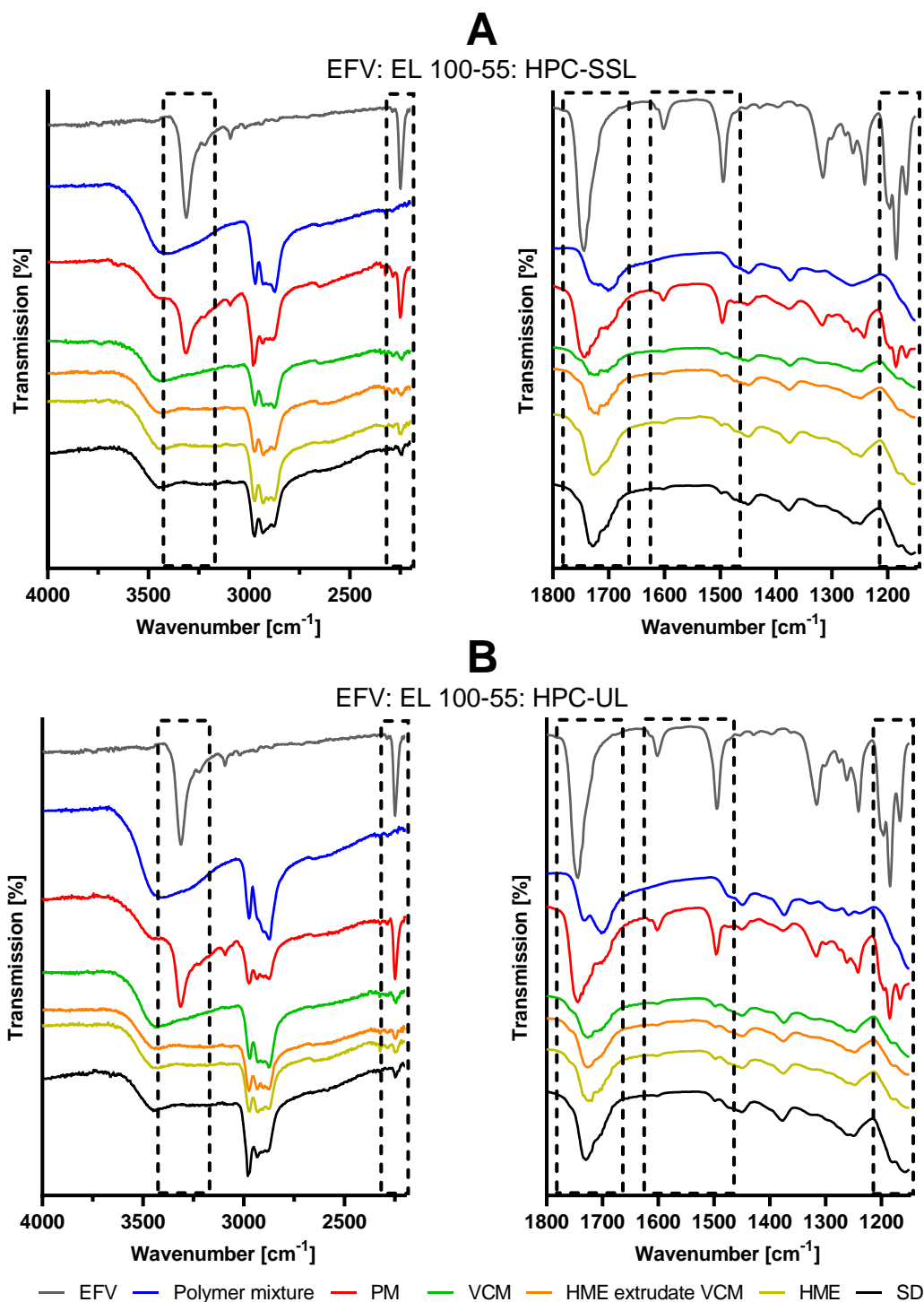


Figure 35: Fourier-transform infrared (FT-IR) spectra of the differently processed ternary efavirenz (EFV) ASDs via vacuum compression molding (VCM), polymer extrudate VCM, hot-melt extrusion (HME), and spray-drying (SD): EFV: EL 100-55: HPC-SSL (**A**) and EFV: EL 100-55: HPC-UL (**B**). The ASDs are compared to neat EFV, the corresponding unprocessed polymer mixture EL 100-55: HPC (50:50) and the corresponding physical mixture (PM) EFV: EL 100-55: HPC (10:45:45). Framing of specific bands marks region of interests. This figure was partially adapted from Pöstges et al., 2023 [104].

5.4. Mechanistical investigation of drug distribution of celecoxib and efavirenz in ternary vacuum compression molded amorphous solid dispersions

Parts of this chapter have been published in a peer-reviewed research article [104]. Each figure was created by the thesis author. Taking or adapting of figures is marked in the corresponding figure.

For a mechanistic understanding of the synergistic interactions of two polymers in respect of the dissolution performance of the drug, elucidating the drug distribution in phases of various polymer ratios is important. Although the polymer placebo investigations (chapter 4.3.) and the DSC of the ternary ASDs (chapter 5.3.) already confirmed the heterogeneous character of the ternary EL 100-55: HPC VCM formulations, the localization of the drugs within the phase separated VCM ASDs remained unknown.

Consequently, the distributions of CXB and EFV in the heterogeneous ternary ASDs were investigated via CRS. Prior to the ASD investigations, the Raman spectra of neat EFV and CXB were determined and compared to the spectra of the polymers to identify characteristic wavenumbers for distinguishing the single substances within the ASDs. Regarding EL 100-55 and HPC-SSL, the intensities at 1730 cm^{-1} and 2885 cm^{-1} were still suitable for detecting the polymers in the formulation (Figure 36A). CXB revealed a characteristic Raman shift at 1615 cm^{-1} , hence the corresponding intensity was used for identifying CXB in the polymer matrix, as indicated by the green arrow in Figure 36B. Moreover, compared to the single Raman spectra of EL 100-55 and HPC-SSL, EFV demonstrated a characteristic peak at 2250 cm^{-1} (Figure 36B). Accordingly, the distribution of EFV was determined via the extent of the intensity at 2250 cm^{-1} .

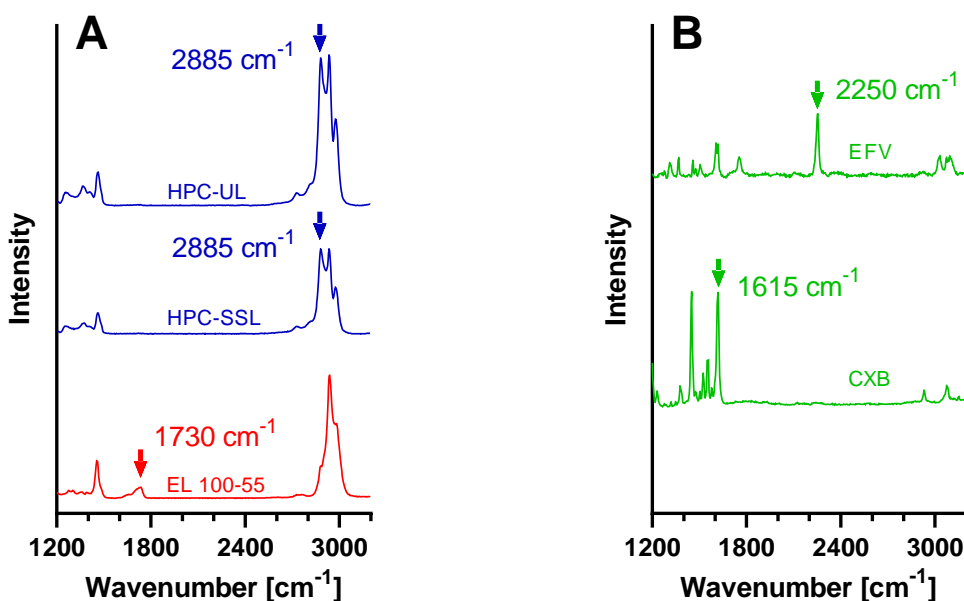


Figure 36: Single Raman spectra of the neat polymers (A) and drugs (B) for the investigations of the ternary VCM ASDs. The utilized wavenumber for detecting the presence of the corresponding substance is presented with an arrow. The spectra of the polymers are already presented in Figure 17. This figure was partially adapted from Pöstges et al., 2023 [104].

Figure 37 - Figure 40 represent the four investigated ternary VCM ASDs. In each figure the distributions of the single components are demonstrated, leading to red-colored (EL 100-55 distribution), blue-colored (HPC distribution), and green-colored (drug distribution) images. Accordingly, in each image the black color is associated to low intensity of the corresponding characteristic Raman shift, indicating lower content of the individual substance.

Figure 37 shows the CRS results of the CXB: EL 100-55: HPC-SSL (VCM) ASD. The inconsistent green color distribution as result of heterogeneous Raman intensities at 1615 cm⁻¹ indicated inconsistent distribution of the drug within the ternary ASD. Inconsistent Raman intensities were also detected by utilizing 1730 cm⁻¹ and 2885 cm⁻¹ for detecting EL 100-55 and HPC-SSL, respectively, confirming the inhomogeneous polymer distributions that were already observed in the VCM placebo formulation (chapter 4.3.). Interestingly, the colors for detecting either CXB or EL 100-55 were complementary to each other, while the distributions of the colors for revealing the presence of CXB and HPC-SSL were very comparable.

Accordingly, during the VCM melting process, CXB distributed preferably into the HPC-SSL-rich phases than into EL 100-55. The presented Raman spectra, referring to the local areas A, B, and C, underline this assumption. Figure 37, spot A revealed a local area with low content of CXB and HPC-SSL, but high content of EL 100-55. Instead Figure 37, spot C demonstrated a spot with high intensity at 2885 cm^{-1} and 1615 cm^{-1} , revealing both high presence of CXB and HPC-SSL, while the intensity of the characteristic Raman shift of EL 100-55 (1730 cm^{-1}) was very low. In Spectrum B, moderate intensities for both polymers and the drugs were obtained. Consequently, moderate distribution of CXB was detected in the polymer phases with a more balanced ratio of EL 100-55 and HPC-SSL (Figure 37C).

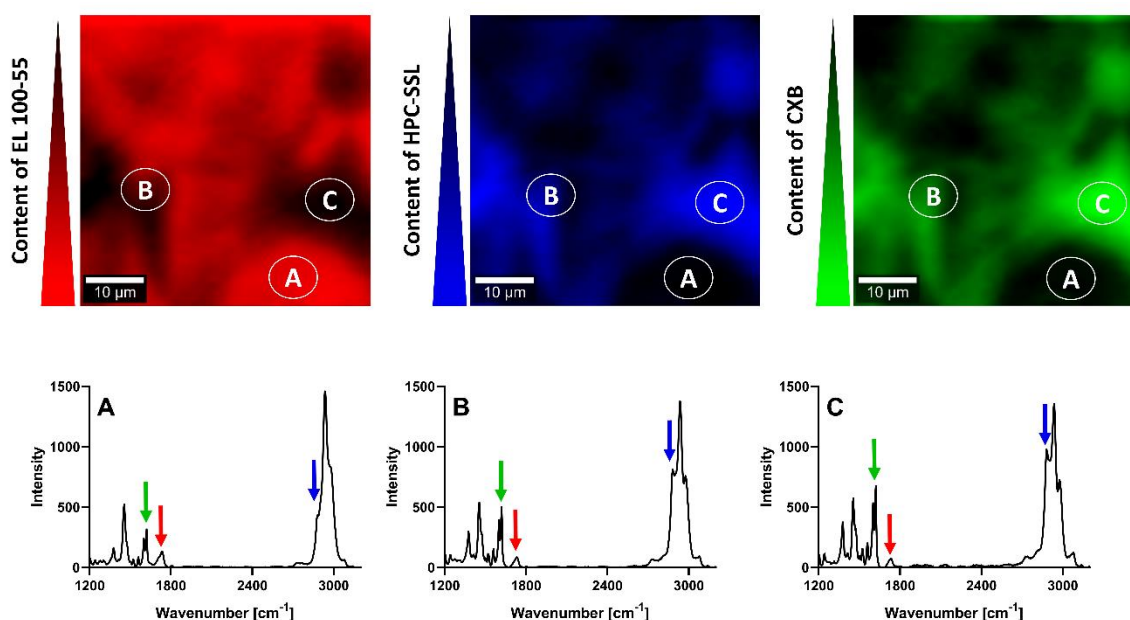


Figure 37: Confocal Raman spectroscopy (CRS) of the CXB: EL 100-55: HPC-SSL ASD (VCM), using the intensities of 1730 cm^{-1} and 2885 cm^{-1} for identifying the polymers EL 100-55 (red color) and HPC-SSL (blue color), respectively. The intensity at 1615 cm^{-1} is used for presenting the distribution of CXB (green color). The Raman spectra A, B and C refer to the spots A, B, and C of the Raman images, respectively, and represent examples of the spectral information.

Regarding the CXB: EL 100-55: HPC-UL ASD (VCM), heterogeneous distribution of both the polymers and the drug was demonstrated (Figure 38). The Raman spectrum in Figure 38, spot A depicted EL 100-55 rich phases, leading to a high intensity of the color red, while Figure 38, spot C revealed HPC-UL-rich phases with very poor red color but increased blue color, instead. A pronounced proportion of the investigated area demonstrated moderate intensity of red and blue colors (Figure 38B), indicating a more balanced

polymer distribution of EL 100-55 and HPC-SSL and a higher content of partially miscible polymer phases.

Comparable to the CXB: EL 100-55: HPC-SSL VCM ASD, higher Raman signals of CXB were associated with higher Raman signals of HPC-UL and lower signals of EL 100-55. Accordingly, CXB distributed preferably into the HPC-UL-richer phases than into the EL 100-55-richer phases.

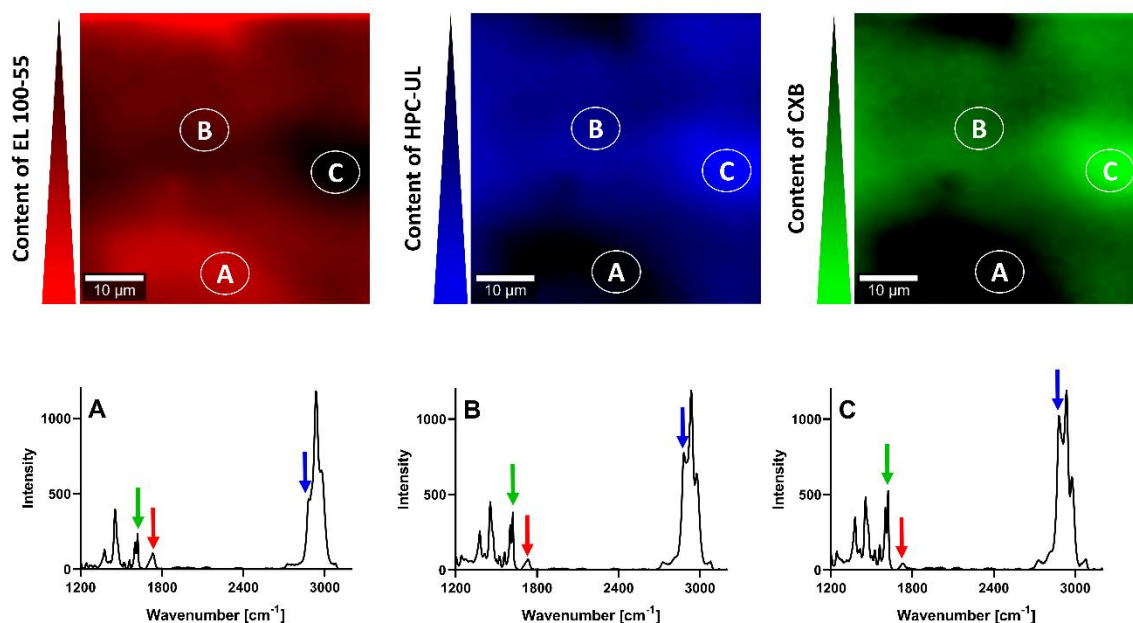


Figure 38: Confocal Raman spectroscopy (CRS) of the CXB: EL 100-55: HPC-UL ASD (VCM), using the intensities of 1730 cm^{-1} and 2885 cm^{-1} for identifying the polymers EL 100-55 (red color) and HPC-UL (blue color), respectively. The intensity at 1615 cm^{-1} is used for presenting the distribution of CXB (green color). The Raman spectra A, B and C refer to the spots A, B, and C of the Raman images, respectively, and represent examples of the spectral information.

Figure 39 and Figure 40 demonstrate the CRS investigations of the EFV: EL 100-55: HPC-SSL ASD (VCM) and of the EFV: EL 100-55: HPC-UL ASD (VCM), respectively. Comparable to the ternary CXB ASDs (VCM), the various intensities at the characteristic Raman shift of EFV (2250 cm^{-1}), represented by the intensity of the green color, clearly revealed heterogeneous distribution of EFV within the polymer matrices.

Also, in both ASDs, the inconsistent intensities of the red and blue colors disclosed a heterogeneous distribution of EL 100-55 and HPC.

Similar to the CXB ternary ASDs higher Raman intensity of the characteristic wavenumber of EFV (2250 cm^{-1}) was associated with lower Raman intensity at 1730 cm^{-1} (for detecting EL 100-55) and vice versus. Instead, increased Raman signals of EFV were detected in HPC-

rich phases (2885 cm^{-1}), leading to similar blue and green color codes images in Figure 39 and Figure 40.

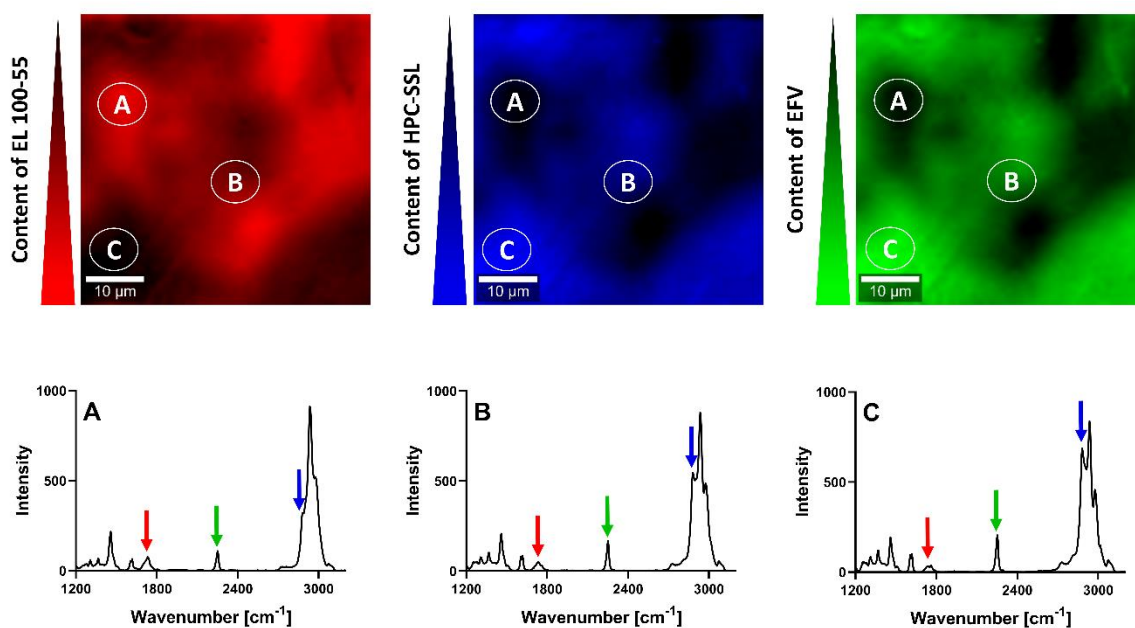


Figure 39: Confocal Raman spectroscopy (CRS) of the EFV: EL 100-55: HPC-SSL ASD (VCM), using the intensities of 1730 cm^{-1} and 2885 cm^{-1} for identifying the polymers EL 100-55 (red color) and HPC-SSL (blue color), respectively. The intensity at 2250 cm^{-1} is used for presenting the distribution of EFV (green color). The Raman spectra A, B and C refer to the spots A, B, and C of the Raman images, respectively, and represent examples of the spectral information. This figure was taken from Pöstges et al., 2023 [104].

Interactions between Eudragit® L 100-55 and hydroxypropyl cellulose in solid-state and dissolution of ternary amorphous solid dispersions using celecoxib and efavirenz as model drugs

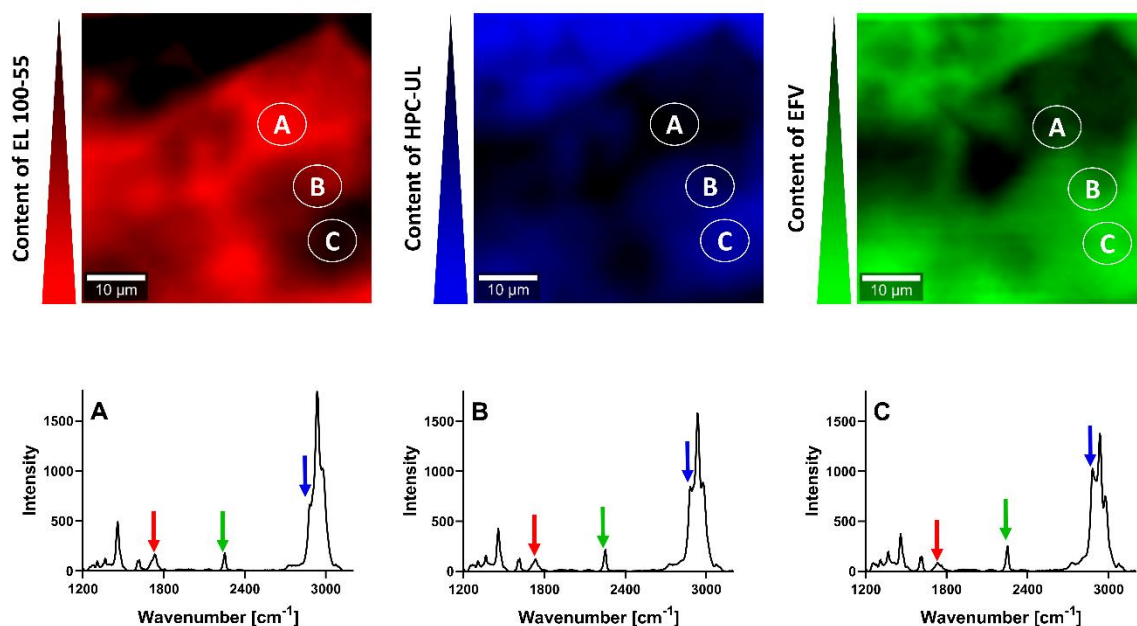


Figure 40: Confocal Raman spectroscopy (CRS) of the EFV: EL 100-55: HPC-UL ASD (VCM), using the intensities of 1730 cm^{-1} and 2885 cm^{-1} for identifying the polymers EL 100-55 (red color) and HPC-UL (blue color), respectively. The intensity at 2250 cm^{-1} is used for presenting the distribution of EFV (green color). The Raman spectra A, B and C refer to the spots A, B, and C of the Raman images, respectively, and represent examples of the spectral information. This figure was taken from Pöstges et al., 2023 [104].

In order to understand why both CXB and EFV distributed preferably into the HPC polymers than into EL 100-55, the maximum kinetic solid-state solubility of each drug in EL 100-55, HPC-SSL and HPC-UL with respect to the selected VCM processing conditions ($160\text{ }^{\circ}\text{C}$ for 15 min) were investigated via DSC. Due to the expected exceedance of the saturated solubility and the resulting instability of the amorphous state, the highly drug loaded ASDs were investigated immediately after the VCM process to prevent falsification of the results. Complete and single-phased miscibility of the drugs in the single polymers would be indicated by the absence of the drug's T_m and the detection of only one T_g . The presence of a T_m or a second T_g would indicate residual crystals and amorphous-amorphous phase separation, respectively, as results of the exceedance of the kinetic solid-state solubility. As starting drug-polymer composition, binary ASDs with a drug load of 50% were processed via VCM ($160\text{ }^{\circ}\text{C}$, 15 min) and investigated. Dependent on the obtained results, the drug load was either increased or decreased by 10% until the maximum kinetic solid-state solubility was elaborated. An overview of all processed highly drug loaded CXB and EFV ASDs with detected T_g s and T_m s is provided in Table 17.

Figure 41 presents the DSC thermograms of the highly drug loaded CXB ASDs, using EL 100-55 (Figure 41A), HPC-SSL (Figure 41B), and HPC-UL (Figure 41C) as ASD-forming polymers.

Regarding the CXB: EL 100-55 ASD (50% drug load), the DSC thermogram revealed a sharp melting peak of crystalline CXB (151.5 ± 1.0 °C), while no T_g was detected (Figure 41A). Compared to the melting point of CXB (162.0 ± 0.3 °C, determined in chapter 5.2.), the formulation exhibited a depressed melting point. The melting point depression of the drug is attributed to drug-polymer interactions, leading to a reduced chemical potential of the drug in the mixture [27,124]. Even by decreasing the drug load to 40% and to 30%, T_{ms} of CXB at 151.7 ± 0.5 °C and 149.1 ± 0.3 °C, respectively, were observed in the binary EL 100-55 ASDs. By further decreasing the drug load to 20%, the T_m of CXB was no longer detected. Instead, the appearance of one single T_g at 97.9 ± 1.0 °C showed the formation of a single-phased ASD and complete miscibility of CXB within EL 100-55.

By utilizing HPC-SSL or HPC-UL for forming binary ASDs with 50% drug load, CXB was embedded complete amorphously and homogeneously into the polymer matrix, revealing single T_g s at 53.7 ± 0.3 °C for the HPC-SSL ASD and 52.7 ± 0.2 °C for the HPC-UL ASD (Figure 41B and Figure 41C). Interestingly, in contrast to the neat HPC polymers and the ASDs with 10% drug load (chapters 4.3. and 5.3.), the higher drug content enabled the detection of pronounced step heights in the reversing heat flows at the glass transition, confirming the formation of single-phased ASDs.

First residual CXB crystallinity was observed after increasing the drug load to 60%, as T_{ms} at 137.9 ± 0.5 °C and 133.8 ± 1.1 °C were detected for the HPC-SSL ASD and the HPC-UL ASD, respectively, indicating the exceedance of the kinetic CXB solubility in the HPC polymers.

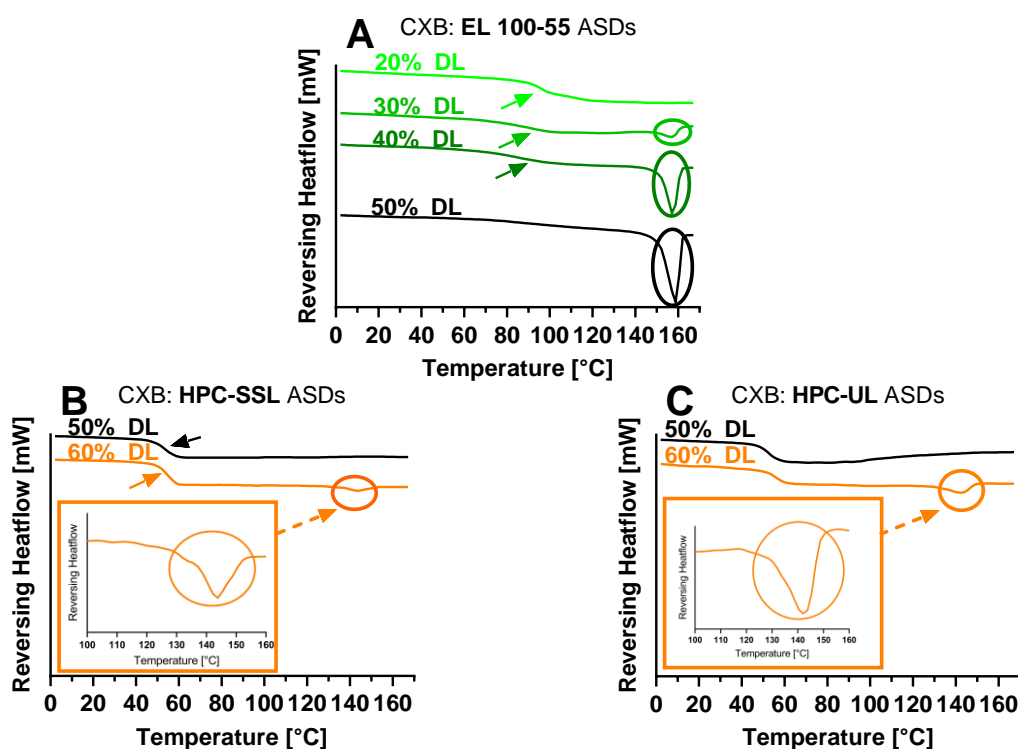


Figure 41: Differential scanning calorimetry (DSC) thermograms (exo up) of highly drug loaded CXB: EL 100-55 (A), CXB: HPC-SSL (B) and CXB: HPC-UL (C) ASDs for determining maximum kinetic solid-state solubility of the drug in each single polymer. Measurements were conducted immediately after VCM processing.

Figure 42 depicts the DSC thermograms of the highly drug loaded EFV: EL 100-55 (Figure 42A), EFV: HPC-SSL (Figure 42B), and EFV: HPC-UL ASDs (Figure 42C). Regarding the highly drug loaded binary ASDs, all processed formulations with the initial drug load of 50% showed absence of the EFV melting point and one single T_g , indicating complete miscibility of EFV in the polymers. By increasing the drug load to 60%, the kinetic solid-state solubility of EFV within EL 100-55 was exceeded, as a depressed melting point of crystalline EFV was detected (128.9 ± 0.1 °C). However, both the EFV: HPC-SSL (60% drug load) and the EFV: HPC-UL (60% drug load) demonstrated absence of the melting peak and one single T_g at 33.5 ± 0.9 °C and 32.3 ± 1.1 °C, respectively. Exceedance of the kinetic solid-state solubility was observed, by further increasing the drug load to 70%, as both ASDs revealed T_m s at 117.3 ± 1.2 °C (EFV: HPC-SSL) and 117.8 ± 0.2 °C (EFV: HPC-UL).

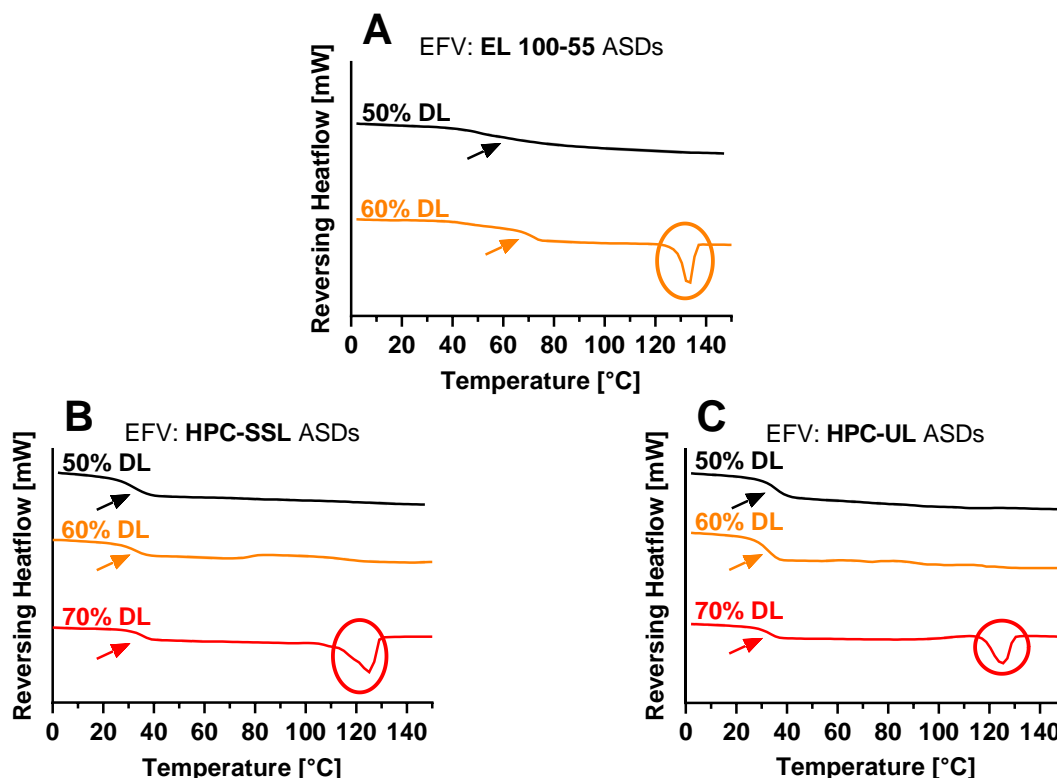


Figure 42: Differential scanning calorimetry (DSC) thermograms (exo up) of highly drug loaded EFV: EL 100-55 (A), EFV: HPC-SSL (B) and EFV: HPC-UL (C) ASDs for determining maximum kinetic solid-state solubility of the drug in each single polymer. Measurements were conducted immediately after VCM processing. This figure was taken from Pöstges et al., 2023 [104].

Apparently, as both CXB and EFV demonstrated higher solid-state solubility in the HPC polymers than in EL 100-55, the drugs distributed preferably into the HPC-richer phases during the VCM processing of the ternary mixtures. Comparable observations were reported by Yang et al. where inconsistent drug distribution of a heterogeneous ternary felodipine PVP-VA: EPO (50:50 polymer blend) ASD was observed. The authors detected higher amount of the drug in PVP-VA in which the drug also demonstrated the higher solid-state solubility [125].

Table 17: Overview of highly drug loaded binary ASDs for investigating the kinetic solid-state solubility of the drugs celecoxib (CXB) and efavirenz (EFV) in EL 100-55, HPC-SSL, and HPC-UL. The “X” shows the processed and tested formulations. The green color covers the drug loads that were within the kinetic solid-state solubility, while the color red demonstrates the exceedance of the kinetic solubility. For every tested formulation the detected glass transition temperature (T_g) and melting temperature (T_m) is provided. In case of absence of T_g or T_m the corresponding field is designated with “n/a”. The values of the thermal events of the EFV ASDs were taken from Pöstges et al., 2023 [104].

Compositions	Drug load						Thermal events [°C]		
	20%	30%	40%	50%	60%	70%	T_g	T_m	
CXB: EL 100-55	X						97.9 ± 1.0	n/a	
							X	88.4 ± 0.2	149.1 ± 0.3
							X	85.5 ± 0.6	151.7 ± 0.5
							X	n/a	151.5 ± 1.0
CXB: HPC-SSL				X			53.7 ± 0.3	n/a	
				X			54.7 ± 0.4	137.9 ± 0.5	
CXB: HPC-UL				X			52.7 ± 0.2	n/a	
				X			55.4 ± 0.4	133.8 ± 1.1	
EFV: EL 100-55				X			55.8 ± 0.2	n/a	
				X			73.1 ± 1.8	128.9 ± 0.1	
EFV: HPC-SSL				X			31.7 ± 0.9	n/a	
				X			33.5 ± 0.9	n/a	
				X			34.6 ± 0.5	117.3 ± 1.2	
EFV: HPC-UL				X			34.7 ± 0.6	n/a	
				X			32.3 ± 1.1	n/a	
				X			32.9 ± 0.1	117.8 ± 0.2	

The differences between the drug solubilities in EL 100-55 and HPC polymers are more pronounced for CXB than for EFV. Thus, for CXB higher discrepancy between the drug distribution within the phase separated polymer phases can be assumed.

Aside the solubility-based drug distribution, the different melt viscosities of EL 100-55, HPC-SSL, and HPC-UL could impact the drug localization, as lower melt viscosity would facilitate diffusion-based drug distribution [126,127]. However, this hypothesis would require lower melt viscosities of both HPC polymers compared to EL 100-55. The melt viscosities of the neat polymers for the VCM processing temperature of 160 °C were

already determined in chapter 4.3. Regarding the melt viscosities at minimal shear rate (1 rad/s) for imitating the non-shear condition of the VCM process, EL 100-55 exhibited a complex viscosity of $299,406 \pm 41,635 \text{ Pa}\cdot\text{s}$, HPC-SSL of $1,287,189 \pm 252,153 \text{ Pa}\cdot\text{s}$, and HPC-UL of $213,085 \pm 23,830 \text{ Pa}\cdot\text{s}$ (Figure 20 and Table 14 in chapter 4.3.). Therefore, as HPC-SSL demonstrated significantly higher melt viscosity at 1 rad/s compared to EL 100-55, the diffusion could not be an additional driving factor for drug distribution.

5.5. Non-sink dissolution testing of heat-based processed amorphous solid dispersions for evaluating the synergistic interactions between Eudragit® L 100-55 and hydroxypropyl cellulose on solubility enhancement and supersaturation of celecoxib and efavirenz

Parts of this chapter have been published in peer-reviewed research articles [83,104]. Each figure was created by the thesis author. Taking or adapting of figures is marked in the corresponding figure.

The non-sink dissolution aimed to investigate the potential benefit of the prepared ternary EL 100-55: HPC ASDs (10% drug load) compared to the corresponding binary ASDs (10% drug load) in terms of solubility enhancement and supersaturation stabilization of the poorly soluble drugs CXB and EFV.

As the selected manufacturing method and the selected HPC grade influenced polymer mixing and the interactions between EL 100-55 and the HPC polymers in the ternary ASDs, the impact of the different solid-states on the dissolutions of CXB and EFV was investigated. The VCM processing technique aims to represent a screening tool of new formulations for HME, thus the dissolution performances of the heat-based processed ASDs (VCM, HME extrudate VCM, HME) were compared.

Figure 43 represents the non-sink dissolution study of the binary (Figure 43A) and ternary ASDs (Figure 43B), comprising of EL 100-55 and HPC-SSL, compared to neat CXB. The poor solubility of crystalline unprocessed CXB was clearly visible, as less than 2 µg/mL of dissolved CXB was detected for the entire observation period of 180 min. Instead, the EL 100-55 ASD demonstrated fast initial release rate, as 65.8 µg/mL of dissolved CXB was detected after 3 min. However, subsequent precipitation led to complete collapse of the supersaturated state. The HPC-SSL ASD showed slower dissolution rate of CXB and a maximum solubility of 23.4 µg/mL, but the capability of maintaining the supersaturated state for the entire observation period with only a slight decrease in concentration (19.6 µg/mL after 180 min). As HPC-SSL demonstrated excellent precipitation inhibiting property for maintaining the supersaturated state of CXB, it was decided to conduct the dissolution of the binary CXB: EL 100-55 ASD together with externally added HPC-SSL. For that purpose, 1.8 mg/mL HPC-SSL was pre-dissolved in the dissolution medium. The amount of added HPC-SSL corresponded to the amount of EL 100-55 that was present within the CXB: EL 100-55 ASD. Again, the CXB: EL 100-55 revealed fast dissolving

character. However, due to the presence of HPC-SSL, the very early precipitation was prevented and the supersaturated state was stabilized up to 10 times compared to the dissolution of the EL 100-55 ASD in neat buffer. After 40 min, precipitation was observed leading to a similar concentration level compared to the binary HPC-SSL ASD after 70 min. Moreover, the dissolutions of the ternary ASDs, processed by HME and VCM of the untreated and pre-extruded polymer mixture were conducted and evaluated (Figure 43B). The ternary CXB: EL 100-55: HPC-SSL VCM ASD with the pre-extruded polymer mixture showed even further improved supersaturation and dissolution performance than the binary EL 100-55 ASD with externally added HPC-SSL, leading to a maximum CXB concentration of 92.6 µg/mL, before precipitation started. The dissolution of the ternary ASD that was solely prepared by HME demonstrated slightly reduced dissolution rate of CXB. Nevertheless, after about 30 min the same extent of supersaturation was observed and stabilized for an even longer period. After 50 min precipitation started until the concentration reached a level of approx. 29.7 µg/mL after 80 min. However, the dissolution of the CXB: EL 100-55: HPC-SSL ASD that was prepared solely by VCM, revealed a pronounced reduction of the initial CXB solubility compared to the HME and HME polymer extrudate VCM ASDs. Despite a fast dissolution rate, only 40.5 µg/mL of dissolved CXB were detected after 6 min. C_{max} of 49.8 µg/mL was obtained after 40 min, followed by precipitation to 17.4 µg/mL after 70 min.

The pronounced differences in dissolution performance of the ternary ASDs can be explained regarding the differences in the solid-state of the processed ASDs. Best performing ternary ASDs were only obtained when the polymer mixture was exposed to heat and shear forces by HME. Consequently, as only the extruded polymers demonstrated single-phased systems and strong solid-state polymer-polymer interactions, the formation of a homogeneous and intimate ASD was required for enabling the full potential of the synergistic interactions between EL 100-55 and HPC-SSL, resulting in optimal extent and stabilization of CXB supersaturation.

As CXB distributed preferably into the HPC-SSL-richer phases of the heterogeneous ternary VCM ASD, high content of the drug was located within the polymer that was demonstrated to be an excellent precipitation inhibitor, but less responsible for increasing the initial solubility of CXB. Consequently, especially the initial generation of the CXB supersaturation upon dissolution was reduced compared to the dissolutions of the homogeneous ternary

HME and HME extrudate VCM ASDs. This led to decreased supersaturation of VCM processed CXB until the precipitation started.

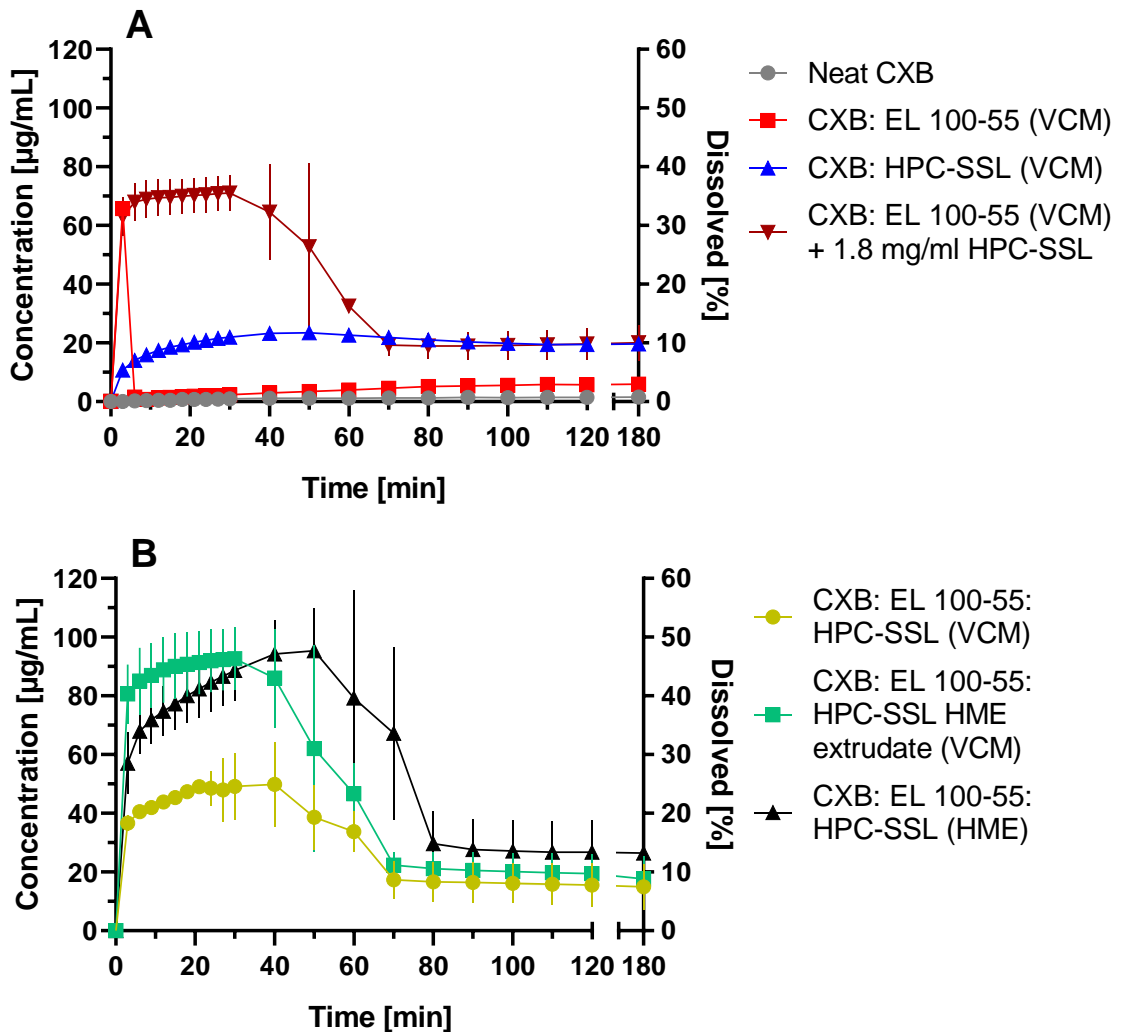


Figure 43: Non-sink dissolutions of binary celecoxib (CXB) ASDs (10% drug load) of EL 100-55, HPC-SSL, EL 100-55 in presence of 1.8 mg/mL pre-dissolved HPC-SSL, processed via vacuum compression molding (VCM) (A) and ternary CXB ASDs (10% drug load), comprising of EL 100-55: HPC-SSL (50:50), processed via hot-melt extrusion (HME) and/or VCM (B). The dissolution was performed in 20 mL pH 6.8 medium (0.05 M phosphate buffer) at 37 °C and 75 rpm paddle speed. This figure was partially adapted from Pöstges et al., 2022 [83].

By using HPC-UL instead of HPC-SSL, the binary CXB: HPC-UL ASD demonstrated continuously increasing dissolution for the first 120 min, leading to a maximum concentration of 47.7 $\mu\text{g/mL}$, followed by a slight decrease to 44.5 $\mu\text{g/mL}$ as final concentration (Figure 44A).

Compared to externally added HPC-SSL, pre-dissolving 1.8 mg/mL HPC-UL as precipitation inhibitor for the fast-dissolving CXB: EL 100-55 led to earlier collapse of the supersaturated system, as the concentration plummeted to less than 27.0 µg/mL after 24 min. Nevertheless, the synergistic interplay between EL 100-55 and HPC-UL for the solubility boost of CXB became already apparent after a few minutes of the dissolution. In contrast to pre-dissolved HPC-SSL, HPC-UL did not only prevent immediate precipitation, but also enabled higher extent of maximum solubility enhancement to 112.7 µg/mL. Earlier precipitation in comparison to externally added HPC-SSL might be due to the higher initial supersaturated state and thereof higher pressure to precipitate.

The dissolutions of the ternary CXB: EL 100-55: HPC-UL ASDs revealed superiority in terms of supersaturation generation and stabilization compared to the binary formulations (Figure 44B). Interestingly, all ternary ASDs showed comparable release of processed CXB, leading to maximum concentrations of 84.8 µg/mL after 40 min (HME ASD), 80.6 µg/mL after 30 min (HME polymer extrudate VCM ASD), and 84.7 µg/mL after 30 min (VCM ASD). Slight differences were only observed in terms of supersaturation stabilization time. For the CXB: EL 100-55: HPC-UL HME extrudate VCM ASD, first precipitation was detected after 40 min while the VCM and HME ASDs maintained the supersaturated state for more than 50 min.

Consequently, the dissolution performances of the ternary CXB: EL 100-55: HPC-UL ASDs were less dependent on the preparation method compared to the ternary CXB: EL 100-55: HPC-SSL ASDs. The solid-state investigations of the VCM processed placebo and ASD formulations revealed higher partial mixing of EL 100-55 and HPC-UL compared to EL 100-55 and HPC-SSL (chapters 4.3. and 5.3.). Apparently, the higher content of miscible polymer phases within the inhomogeneous ternary CXB: EL 100-55: HPC-UL VCM ASD were sufficient for enabling comparable extent of synergistic interactions in terms of dissolution enhancement, compared to the single-phased and extruded polymers.

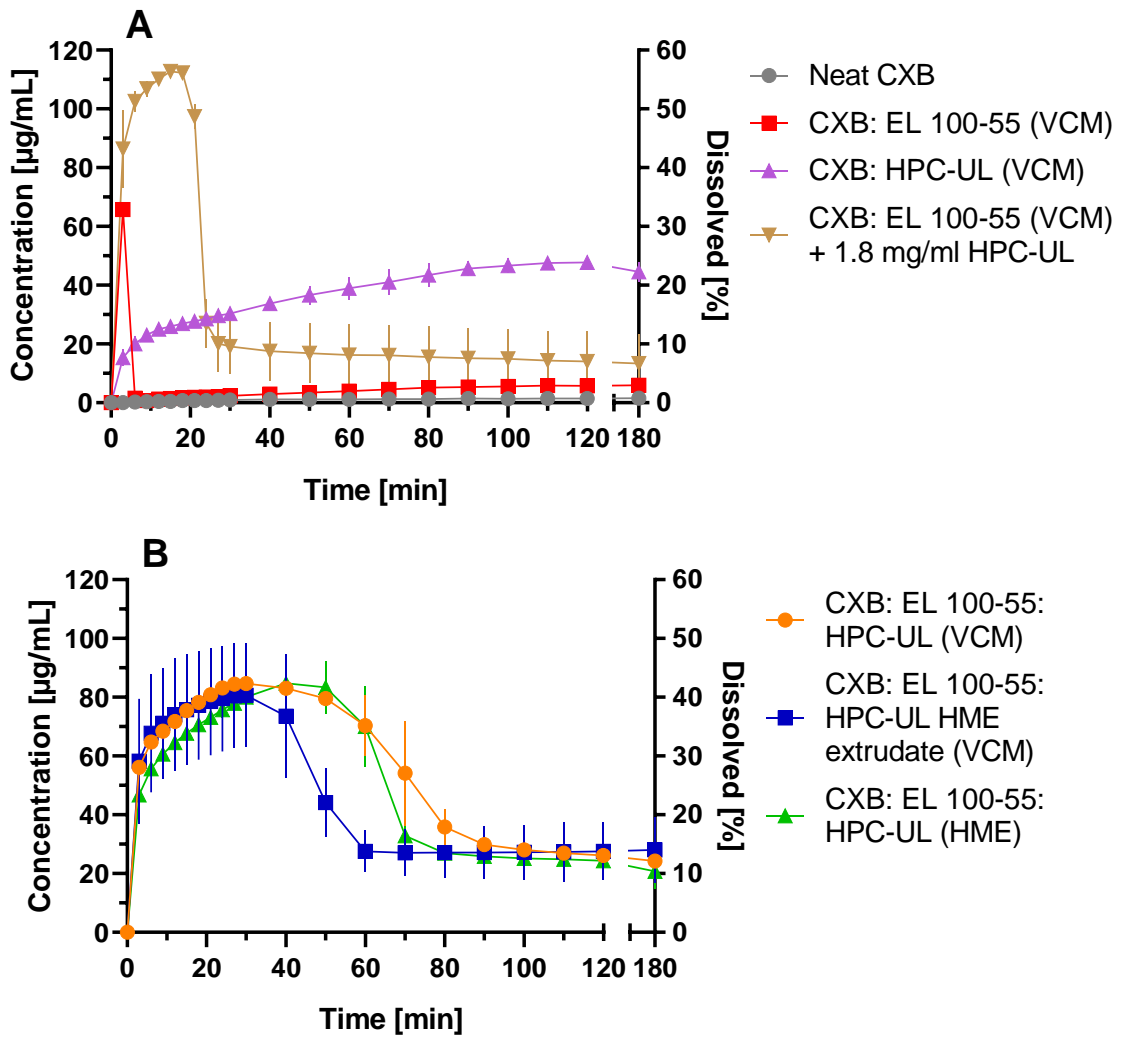


Figure 44: Non-sink dissolutions of binary celecoxib (CXB) ASDs (10% drug load) of EL 100-55, HPC-UL, EL 100-55 in presence of 1.8 mg/mL pre-dissolved HPC-UL, processed via vacuum compression molding (VCM) (A) and ternary CXB ASDs (10% drug load), comprising of EL 100-55: HPC-UL (50:50), processed via hot-melt extrusion (HME) and/or VCM (B). The dissolution was performed in 20 mL pH 6.8 medium (0.05 M phosphate buffer) at 37 °C and 75 rpm paddle speed. Figure A was partially adapted from Pöstges et al., 2022 [83].

Figure 45 demonstrates the non-sink dissolution results of the binary and ternary EFV ASDs, processed via VCM and/ or HME, compared to the neat drug. Due to the poor solubility of crystalline EFV, a maximum concentration of 10.4 µg/mL of dissolved drug was determined during the entire observation period (Figure 45A).

Comparable to the CXB: EL 100-55 ASD, the dissolution of the EFV: EL 100-55 ASD led to a high initial drug release rate, resulting in an EFV concentration of 90.7 µg/mL after 6 min. In contrast to the CXB formulation, the concentration did not plummet immediately, but

increased slightly to 101.6 µg/mL after 21 min, before precipitation started, leading to a final concentration of 54.0 µg/mL after 180 min.

Instead, HPC-SSL showed only low impact on the solubility enhancement of processed EFV, but a slight increase of dissolved drug to 27.8 µg/mL until the end of the observation period.

By pre-dissolving 1.8 mg/mL HPC-SSL for the dissolution of the binary EFV: EL 100-55 ASD, precipitation of dissolved EFV was prevented for the entire observation period. The synergistic interactions between EL 100-55 and HPC-SSL enabled a constant increase of EFV, leading to a final concentration of 164.4 µg/mL.

Regarding the three ternary EFV: EL 100-55: HPC-SSL ASDs, all ASDs showed superior dissolutions compared to the corresponding binary formulations, independent on the manufacturing method (Figure 45B).

However, the HME ASD revealed the most promising dissolution, as the HME ASD demonstrated the fasted drug release rate and a maximum EFV concentration of 156.2 µg/mL after 140 min. This concentration was maintained for the entire dissolution with only small decrease in concentration, leading to a final concentration of 146.1 µg/mL after 180 min. In contrast, the dissolution of the ternary ASD that was solely processed via VCM demonstrated decreased initial dissolution rate, as 73.5 µg/mL were detected after 15 min. Although precipitation was prevented for the entire dissolution, the initial reduced extent of EFV supersaturation led to a decreased final concentration of 117.7 µg/mL after 180 min. Compared to the EFV: EL 100-55: HPC-SSL VCM ASD, the EFV: EL 100-55: HPC-SSL HME extrudate VCM ASD showed a slightly enhanced initial dissolution rate of EFV, leading to 91.3 µg/mL after 15 min. However, after 40 min of dissolution time the HME extrudate VCM ASD exhibited similar concentrations compared to the ASD that was solely prepared via VCM.

Similar to the ternary CXB: EL 100-55: HPC-SSL ASDs, differences in the dissolution performances can be explained by the solid-state of the ASDs. Regarding the heterogeneous ternary VCM ASD, higher content of EFV distributed into the HPC-SSL-rich phases during the melting phase of the preparation. Consequently, higher content of the drug was located within the polymer that did not reveal promising initial solubility enhancement as single polymer. This led to reduced initial dissolution enhancement compared to homogeneous HME and HME polymer extrudate VCM ASDs.

However, in contrast to the ternary CXB: EL 100-55: HPC-SSL formulations, the differences in the dissolutions of the ternary EFV: EL 100-55: HPC-SSL ASDs were less pronounced. Especially comparing the VCM ASD and the HME polymer extrudate VCM ASD, the differences were only observed for the first 30 min of the dissolutions. The kinetic solid-state solubility study (chapter 5.4.) revealed higher difference between the maximum solubility of CXB in EL 100-55 (20% drug load) and in HPC-SSL (50% drug load) compared to EFV (50% drug load for EL 100-55 and 60% drug load for HPC-SSL). As the solid-state solubility was demonstrated to be the driving factor for drug distribution, a more balanced drug distribution within the heterogeneous polymer phases of the ternary EFV VCM ASD can be expected, leading to less pronounced differences between the VCM and HME processed ASDs.

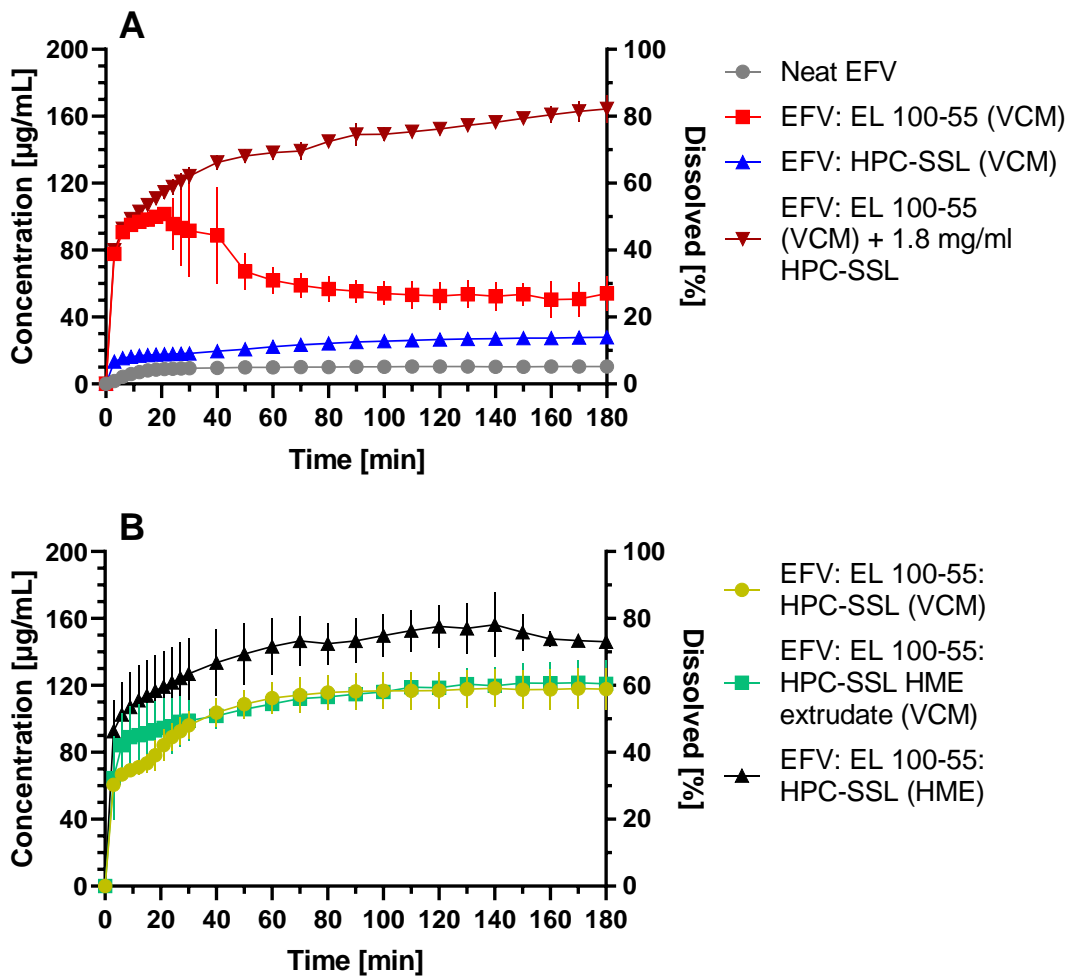


Figure 45: Non-sink dissolutions of binary efavirenz (EFV) ASDs (10% drug load) of EL 100-55, HPC-SSL, EL 100-55 in presence of 1.8 mg/mL pre-dissolved HPC-SSL, processed via vacuum compression molding (VCM) (A) and ternary EFV ASDs (10% drug load), comprising of EL 100-55: HPC-SSL (50:50), processed via hot-melt extrusion (HME) and/or VCM (B). The dissolution was performed in 20 mL pH 6.8 medium (0.05 M phosphate buffer) at 37 °C and 75 rpm paddle speed. This figure was partially adapted from Pöstges et al., 2023 [104].

Figure 46 depicts the dissolution performances of the binary and ternary EFV ASDs, comprising of EL 100-55 and HPC-UL, and of the neat drug. Similar to HPC-SSL, HPC-UL was not suitable to generate a promising supersaturated EFV solution, as the ASD showed only slight enhanced dissolution compared to crystalline EFV (Figure 46A). However, by pre-dissolving 1.8 mg/mL HPC-UL, the EFV: EL 100-55 ASD exhibited an even faster dissolution rate compared to the respective dissolution in neat buffer. Moreover, the addition of external HPC-UL prevented precipitation for the entire dissolution, leading to

an approx. 3-fold higher final concentration (167.6 µg/mL) compared to the dissolution of EFV: EL 100-55 without pre-dissolved HPC-UL (54.0 µg/mL).

Similar to the ternary ASDs with HPC-SSL, the supersaturated solutions that were generated upon dissolutions of the ternary EFV: EL 100-55: HPC-UL ASDs were stabilized for the entire observation period (Figure 46B). Noticeably, the dissolution rates of all ternary ASDs were comparable for the first 60 min, followed by superior dissolution of the ASD that was solely processed via HME. While the HME ASD revealed a final concentration of 153.1 µg/mL, the dissolutions of the VCM ASD and the HME extrudate VCM ASD ended with concentrations of 111.0 µg/mL and 121.9 µg/mL, respectively.

Similar to the CXB: EL 100-55: HPC-UL VCM ASD, the solid-state analysis disclosed higher partial mixing of VCM processed EL 100-55 and HPC-UL (chapters 4.3. and 5.3.). Apparently, the higher content of miscible phases in the inhomogeneous VCM formulation led to comparable synergistic interactions of the polymers in terms of EFV dissolution enhancement, compared to the polymer extruded formulations.

Interactions between Eudragit® L 100-55 and hydroxypropyl cellulose in solid-state and dissolution of ternary amorphous solid dispersions using celecoxib and efavirenz as model drugs

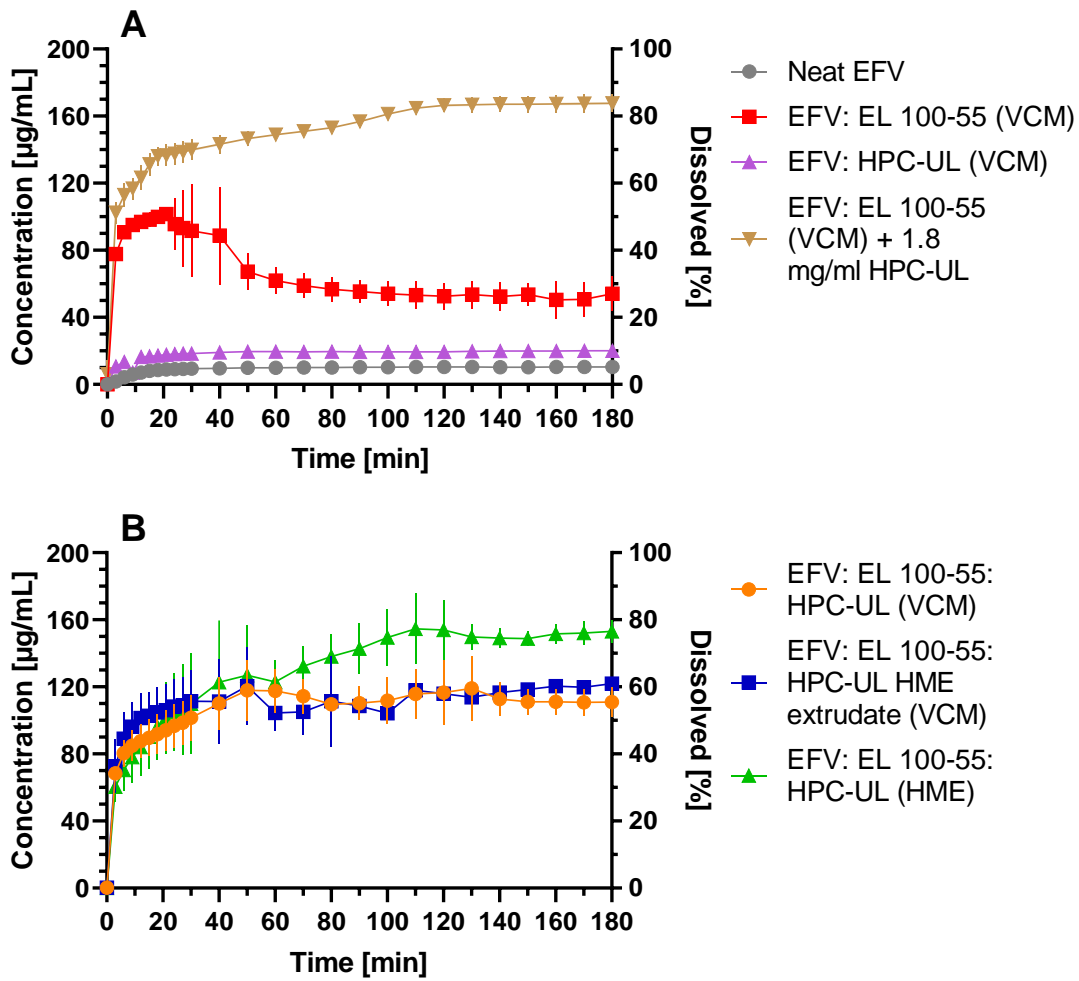


Figure 46: Non-sink dissolutions of binary efavirenz (EFV) ASDs (10% drug load) of EL 100-55, HPC-UL, EL 100-55 in presence of 1.8 mg/mL pre-dissolved HPC-UL, processed via vacuum compression molding (VCM) (**A**) and ternary EFV ASDs (10% drug load), comprising of EL 100-55: HPC-UL (50:50), processed via hot-melt extrusion (HME) and/or VCM (**B**). The dissolution was performed in 20 mL pH 6.8 medium (0.05 M phosphate buffer) at 37 °C and 75 rpm paddle speed. This figure was partially adapted from Pöstges et al., 2023 [104].

5.6. Non-sink dissolution testing of spray-dried ternary amorphous solid dispersions

Due to general differences between heat-based and SD processed ASDs (smaller particle sizes and larger particle surface area of SD formulations) [128,129], the dissolutions of the EL 100-55: HPC SD ASDs (10% drug load) were evaluated, separately.

The small size of the SD particles was confirmed by the laser diffractometer. The particle size distributions and the corresponding d_{10} , d_{50} and d_{90} values [μm] are presented in Figure 47.

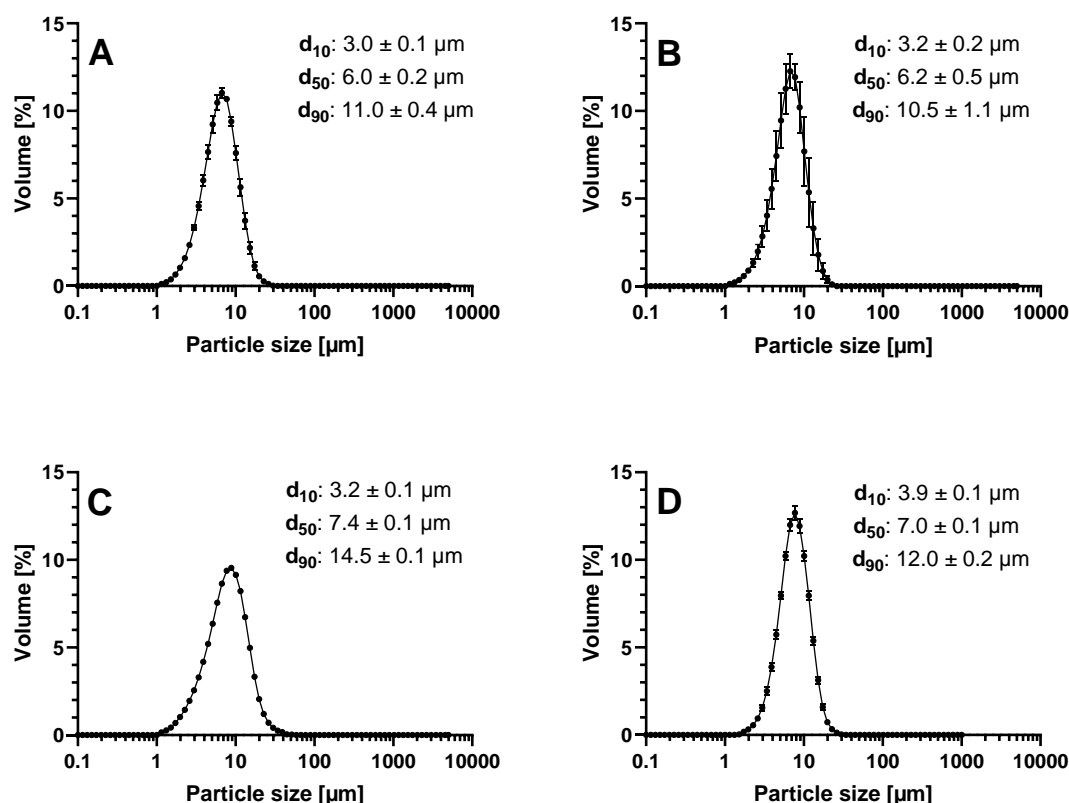


Figure 47: Particle size distribution of ternary spray-dried (SD) ASDs, including the presentation of the respective d_{10} , d_{50} , d_{90} values [μm]: CXB: EL 100-55: HPC-SSL (SD) (A), CXB: EL 100-55: HPC-UL (SD) (B), EFV: EL 100-55: HPC-SSL (SD) (C), EFV: EL 100-55: HPC-UL (SD) (D).

Figure 48 demonstrates the dissolutions of the CXB: EL 100-55: HPC-SSL SD ASD and of the CXB: EL 100-55: HPC-UL SD ASD. Neither the initial dissolution rate, nor the stabilization time of the CXB supersaturated state was influenced by the selection of the HPC grade, as both dissolution performances were very comparably. The small particles of the ternary

SD formulations provided high surface area upon dissolution, enabling maximum concentrations of almost 140 µg/mL after 40 min, immediately before the supersaturated states collapsed.

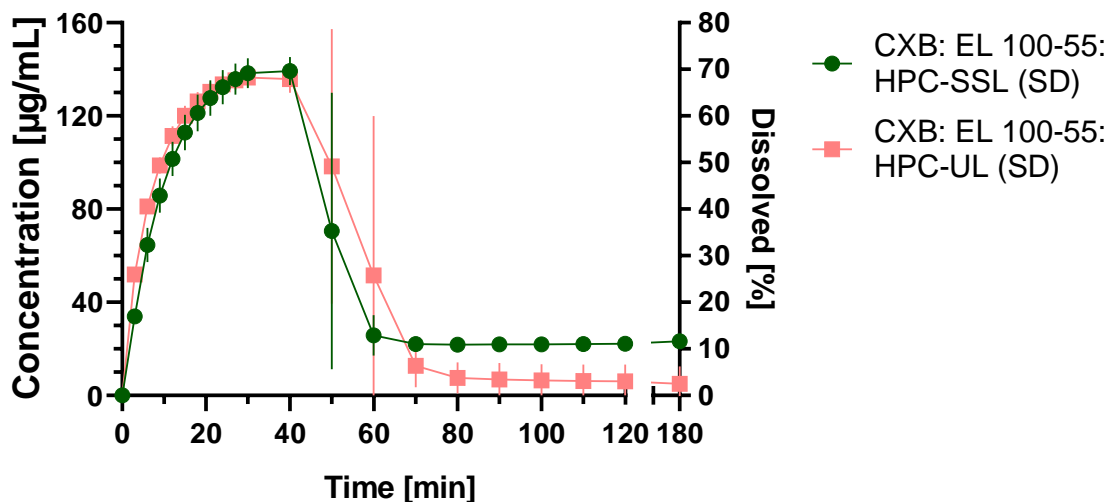


Figure 48: Non-sink dissolutions of ternary celecoxib (CXB) ASDs (10% drug load) processed via spray-drying (SD), comprising of EL 100-55 and HPC-SSL (50:50) or EL 100-55 and HPC-UL (50:50). The dissolution was performed in 20 mL pH 6.8 medium (0.05 M phosphate buffer) at 37 °C and 75 rpm paddle speed.

The dissolutions of the ternary SD ASDs, comprising of EFV, EL 100-55 and HPC are presented in Figure 49. For the first 40 min of dissolutions both ASDs demonstrated comparable dissolution rates, leading to concentrations of approx. 140 µg/mL. While the EFV: EL 100-55: HPC-UL ASD exhibited slight reduction of the concentration, the EFV: EL 100-55: HPC-SSL ASD maintained the maximum concentrations for 80 min. However, after 100 min of testing time, both ASDs revealed similar dissolution of EFV, ending in final concentrations of approx. 128 µg/mL.

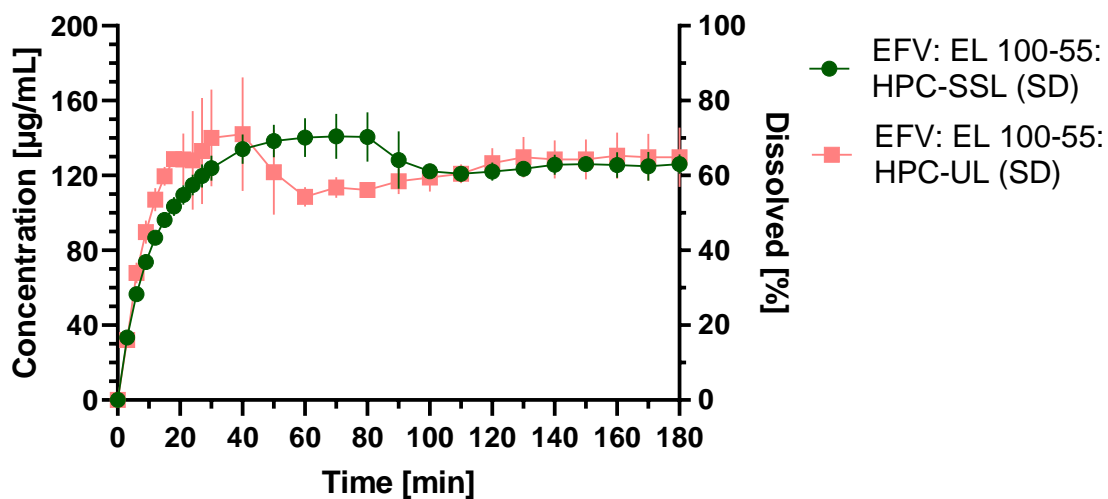


Figure 49: Non-sink dissolutions of ternary efavirenz (EFV) ASDs (10% drug load) processed via spray-drying (SD), comprising of EL 100-55 and HPC-SSL (50:50) or EL 100-55 and HPC-UL (50:50). The dissolution was performed in 20 mL pH 6.8 medium (0.05 M phosphate buffer) at 37 °C and 75 rpm paddle speed.

5.7. Conclusion

In this chapter, the insights of the supersaturation potential of the EL 100-55: HPC polymer blends were combined with the insights of the manufacturing-dependent solid-state characteristics, by preparing binary and ternary CXB and EFV ASDs (10% drug load) via VCM, HME, and SD. All processed formulations led to complete conversion of the crystalline drugs into the amorphous state. However, while HME and SD enabled homogeneously embedding of the drugs, inhomogeneous drug distributions were observed in the heterogeneous ASDs that were prepared solely via VCM. Due to higher kinetic solid-state solubility of both CXB and EFV in HPC compared to EL 100-55, the drugs distributed preferably into the HPC-richer phases of the phase separated VCM ASDs. Subsequently, the influences of the selected manufacturing method and selection of the HPC grade on the dissolution performance were investigated. While neither EL 100-55, nor the HPCs alone demonstrated promising dissolution performances, the synergistic interactions resulted in pronounced enhancement of solubility and supersaturation stabilization of CXB and EFV. The formation of the maximum synergistic interplay between the two polymers and the drugs required miscible polymer phases that were obtained independently on the utilized HPC grade within the single-phased HME polymer extrudate VCM, HME, and SD processed ternary ASDs.

Consequently, for the heat-based processed EL 100-55: HPC-SSL ternary ASDs, the HME ASDs outperformed the phase separated ASDs that were prepared solely via VCM.

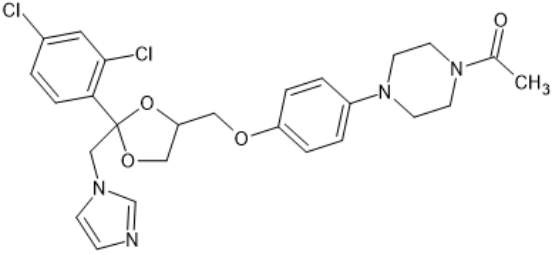
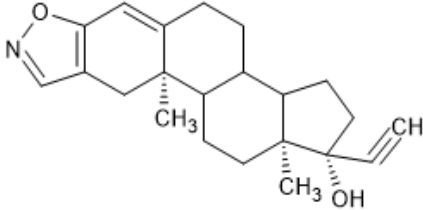
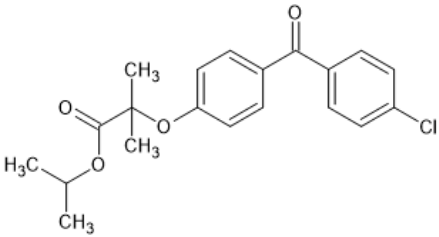
However, the ternary ASDs, consisting of HPC-UL as HPC grade, revealed promising dissolution results, independently on the selected manufacturing method. As the formation of partially miscible polymer phases via VCM was facilitated by using the lower melt viscosity HPC grade -UL (chapter 4.), comparable synergistic interactions enabled comparable dissolutions between the solely VCM and HME processed ASDs.

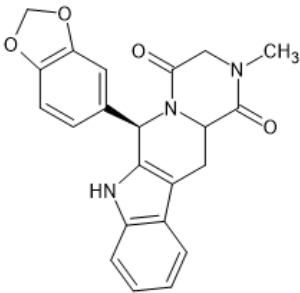
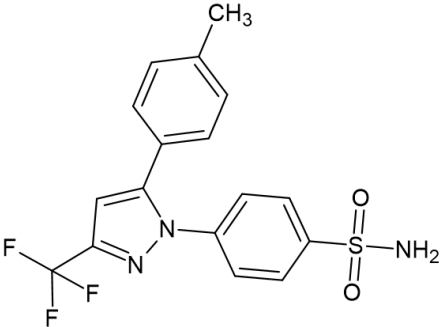
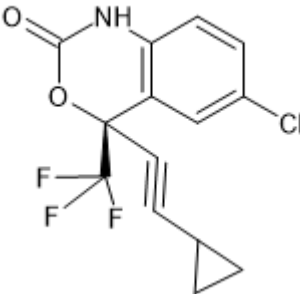
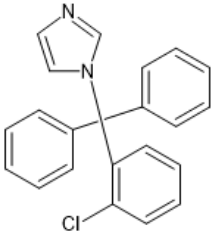
6. Materials and methods

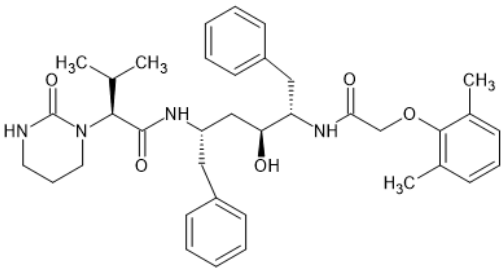
6.1. Materials

6.1.1. Drug substances

Table 18: Chemical structures, information about the supplier/manufacturer, and relevant physicochemical properties of the investigated drugs. Except the molecular weight (MW), the physicochemical properties refer to predicted values, obtained from DrugBank [130].

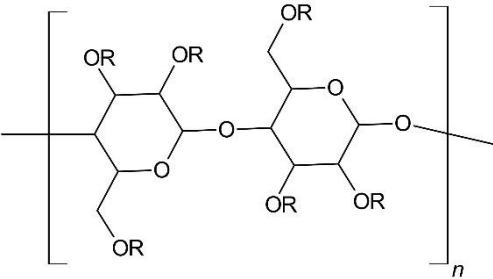
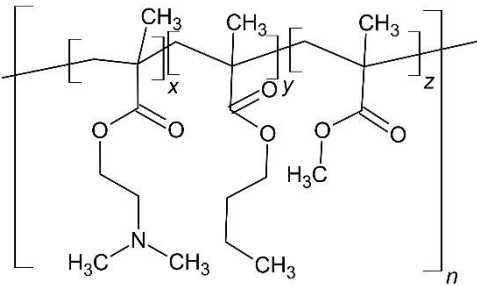
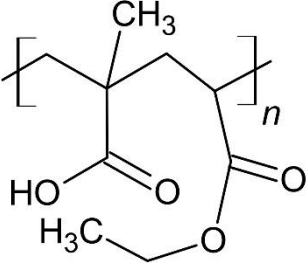
<p style="text-align: center;">Ketoconazole (KTZ)</p> 	<p>Supplier or manufacturer: Thermo Fisher (Kandel) GmbH, Kandel, Germany</p> <p>Physicochemical properties [131]: MW: 531.4 g/mol Acid/ base/ neutral: Weak base pKa(s): 6.42 Hydrogen acceptor count: 6 Hydrogen donor count: 0</p> <p>BCS class: II [52]</p>
<p style="text-align: center;">Danazol (DNZ)</p> 	<p>Supplier or manufacturer: BASF SE, Ludwigshafen, Germany</p> <p>Physicochemical properties [132]: MW: 337.5 g/mol Acid/ base/ neutral: Neutral pKa(s): 17.59 (acidic) and 0.25 (basic) Hydrogen acceptor count: 2 Hydrogen donor count: 1</p> <p>BCS class: II [133]</p>
<p style="text-align: center;">Fenofibrate (FEN)</p> 	<p>Supplier or manufacturer: Sigma Aldrich Chemie GmbH, Taufkirchen, Germany</p> <p>Physicochemical properties [134]: MW: 360.8 g/mol Acid/ base/ neutral: Neutral pKa(s): -4.9 (basic) Hydrogen acceptor count: 3 Hydrogen donor count: 0</p> <p>BCS class: II [135]</p>

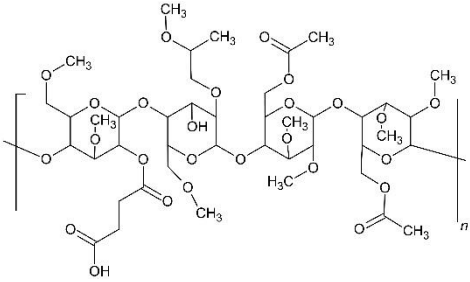
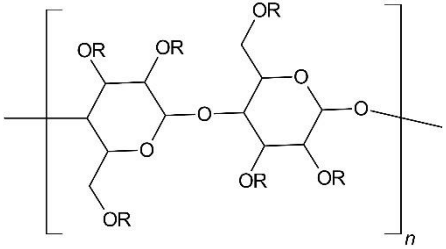
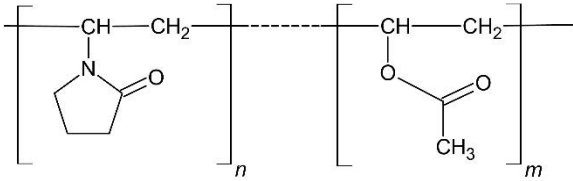
<p style="text-align: center;">Tadalafil (TDL)</p> 	<p>Supplier or manufacturer: Acros Organic BV, Geel, Belgium</p> <p>Physicochemical properties [136]: MW: 389.4 g/mol Acid/ base/ neutral: Neutral pKa(s): 15.17 (acidic) and -4.2 (basic) Hydrogen acceptor count: 4 Hydrogen donor count: 1</p> <p>BCS class: II [137]</p>
<p style="text-align: center;">Celecoxib (CXB)</p> 	<p>Supplier or manufacturer: Swapnroop Drugs&Pharmaceuticals, Aurangabad, India</p> <p>Physicochemical properties [138]: MW: 381.4 g/mol Acid/ base/ neutral: Weak acid pKa(s): 10.6 (acidic) and -0.41 (basic) Hydrogen acceptor count: 3 Hydrogen donor count: 1</p> <p>BCS class: II [139]</p>
<p style="text-align: center;">Efavirenz (EFV)</p> 	<p>Supplier or manufacturer: Swapnroop Drugs&Pharmaceuticals, Aurangabad, India</p> <p>Physicochemical properties [140]: MW: 315.7 g/mol Acid/ base/ neutral: Weak acid pKa(s): 12.52 (acidic) and -1.5 (basic) Hydrogen acceptor count: 2 Hydrogen donor count: 1</p> <p>BCS class: II/ IV [141]</p>
<p style="text-align: center;">Clotrimazole (CLT)</p> 	<p>Supplier or manufacturer: TCI Europe N.V., Zwijndrecht, Belgium</p> <p>Physicochemical properties [142]: MW: 344.8 g/mol Acid/ base/ neutral: Weak base pKa(s): 6.26 Hydrogen acceptor count: 1 Hydrogen donor count: 0</p> <p>BCS class: II [143]</p>

<p style="text-align: center;">Lopinavir (LPV)</p> 	<p>Supplier or manufacturer: Acros Organic BV, Geel, Belgium</p> <p>Physicochemical properties [144]: MW: 628.8 g/mol Acid/ base/ neutral: Weak acid pKa(s): 13.39 (acidic) and -1.5 (basic) Hydrogen acceptor count: 5 Hydrogen donor count: 4</p> <p>BCS class: IV [145]</p>
---	---

6.1.2. Polymer substances

Table 19: Molecular structures, information about the supplier/ manufacturer, and relevant physicochemical properties of utilized polymers.

<p>Hydroxypropyl cellulose (HPC)- L, -SSL, -UL</p>  <p style="text-align: center;">R= -H, $-(\text{-CH}_2\text{-CH}(\text{CH}_3)\text{-O})_m\text{H}$, m= 1-5</p>	<p>Supplier or manufacturer: Nippon Soda Co., Ltd., Tokyo, Japan</p> <p>Physicochemical properties [84]: MW (HPC-L): 140,000 g/mol MW (HPC-SSL): 40,000 g/mol MW (HPC-UL): 20,000 g/mol Aqueous solubility: pH-independent soluble</p>
<p>Basic butylated methacrylate copolymer (Eudragit® EPO, EPO)</p> 	<p>Supplier or manufacturer: Evonik, Darmstadt, Germany</p> <p>Physicochemical properties [146]: MW: 47,000 g/mol Aqueous solubility: Soluble below pH 5.0, permeable above pH 5.0</p>
<p>Methacrylic acid-ethyl acrylate copolymer (1:1) (Eudragit® L 100-55, EL 100-55)</p> 	<p>Supplier or manufacturer: Evonik, Darmstadt, Germany</p> <p>Physicochemical properties [85]: MW: 320,000 g/mol Aqueous solubility: Soluble above pH 5.5</p>

<p>Hydroxypropyl methylcellulose acetate succinate (HPMCAS) M</p> 	<p>Supplier or manufacturer: Shin-Etsu Chemical, Tokyo, Japan</p> <p>Physicochemical properties: MW: 17,000 [147] Aqueous solubility: Soluble above pH 6.0 [148]</p>
<p>Hydroxypropyl methylcellulose (HPMC) HME 15 LV</p>  <p>R= -H, -CH₃, -CH₂-CHOH-CH₃</p>	<p>Supplier or manufacturer: DuPont Pharma & Nutrition, Luzern, Switzerland</p> <p>Physicochemical properties [117]: MW: 84,400 g/mol Aqueous solubility: pH-independent soluble</p>
<p>Vinylpyrrolidone-vinyl acetate copolymer (Kollidon® VA 64, VA 64)</p> 	<p>Supplier or manufacturer: BASF SE, Ludwigshafen, Germany</p> <p>Physicochemical properties [85]: MW: 45,000 – 70,000 g/mol Aqueous solubility: pH-independent soluble</p>

6.1.3. Additional chemical substances

Table 20: Overview of additional chemical substances that were used for performing the experiments of the thesis.

Excipient/ Chemical	Supplier or manufacturer
Dimethyl sulfoxide (DMSO)	Fisher Scientific, Geel, Belgium
Di-sodium hydrogen phosphate dihydrate	Th. Geyer, Renningen, Germany
Sodium dihydrogen phosphate dihydrate	Th. Geyer, Renningen, Germany
Ethanol 96% (v/v) (technical use)	VWR International GmbH, Darmstadt, Germany
n-Hexane	VWR International S.A.S., Rosny-sous-Bois, France
Sorbitan monoleate (Span® 80)	Croda Iberica SA Mevisa, Fogars de la Selva, Spain

6.2. Supersaturation assay as fast-screening method

The influence of various polymers on supersaturation extent and supersaturation stabilization of in total eight different drugs were investigated, by implementing a supersaturation screening apparatus. The utilized polymers were freshly pre-dissolved at a concentration of 1.25 mg/mL in 0.05 M phosphate buffer (pH 6.8 medium). As EPO is described to be a pH-dependent soluble polymer (pH < 5.0), the polymer was suspended 48 h before performing the supersaturation assay. In order to compare not only the polymers in relation to each other, but also to evaluate the absolute impact of the polymers on supersaturation, a data set in neat buffer without polymer addition was collected, additionally.

For each single measurement a volume of 10 mL polymer solution was filled into a glass vial (\varnothing 26 x 70 mm). In case of the investigations of the polymer mixture EL 100-55: HPC-SSL (50:50), 5 mL of each polymer solution was added into the sample vial, leading to a total polymer concentration of 1.25 mg/mL. The vials were placed into a tempered water bath (37 °C) on a multi-position magnetic stirrer and stirred using PTFE stirring bars (cylindrical, 12 x 4.5 mm). The stirring speed was set to 240 rpm for enabling high hydrodynamic conditions but without forming a funnel.

The drugs were dissolved completely in dimethyl sulfoxide (DMSO) at concentrations of 40 mg/mL. In case of LPV and CLT, ethanol was used instead of DMSO, as the UV/VIS cut off of DMSO interfered with the UV/VIS absorption maxima of these drugs.

The supersaturation testing was started by adding 50 μ L of the organic drug stock solution into the pre-tempered polymer solutions. Thereby, only a minimal amount of DMSO/ethanol was utilized to prevent solubility enhancement due to the cosolvent effect. The polymer concentrations (1.25 mg/mL) and the maximum potential drug concentrations (0.2 mg/mL=100%) were selected based on a realistic drug- polymer ratio for ASD processing (10 to 20% drug load), resulting in a theoretical drug load of 14%.

After 30 or 60 min, the vials were removed from the water bath and the samples were filtered through 0.2 μ m polyethersulfone (PES) membrane syringe filter. As for some drug-polymer combinations high content of small-sized precipitate was expected, a glass fiber filter with a pore size of 0.7 μ m was installed before the PES membrane filter to prevent blocking of the filter system. To exclude adsorption of the drugs to the membrane, the filters were sufficiently pre-saturated before the filtrate was collected. Immediately after

the filtration process, the amounts of dissolved drugs were measured using an 8453 UV/VIS spectrophotometer (Agilent, Waldbronn, Germany). The utilized wavelength for calculating the concentrations of the individual drugs in the supersaturation screening are depicted in Table 21.

Table 21: Overview of the utilized wavelengths of the drugs for calculation of the dissolved amounts in the supersaturation screening (Chapter 2.).

Drug	Wavelength for calculation of dissolved drug [cm⁻¹]
Ketoconazole (KTZ)	243 nm
Danazol (DNZ)	287 nm
Fenofibrate (FEN)	289 nm
Tadalafil (TDL)	284 nm
Celecoxib (CXB)	254 nm
Efavirenz (EFV)	248 nm
Clotrimazole (CLT)	227 nm (First derivative of absorption)
Lopinavir (LPV)	220 nm (First derivative of absorption)

6.3. Supersaturation assay using the MiniDissolution apparatus

The impact of the single polymers EL 100-55, HPC-L, HPC-SSL, HPC-UL, and of corresponding polymer mixtures on supersaturation extent and supersaturation stabilization of the poorly soluble drug CXB was investigated for 180 min, utilizing a miniaturized USP dissolution apparatus II (MiniDissolution apparatus) [149]. The paddle speed and the temperature were set to 75 rpm and 37 °C, respectively. The investigated polymers and polymer mixtures were freshly pre-dissolved at a total polymer concentration of 1.25 mg/mL in 0.05 M phosphate buffer (pH 6.8). DMSO stock solutions were obtained by dissolving CXB at a concentration of 40 mg/mL. By adding 100 µL of the DMSO stock solution into 20 mL of the pre-warmed polymeric phosphate buffer (corresponding to a potential drug concentration of 0.2 mg/mL), the experiments were initiated. Additionally, data set of the supersaturation behavior of neat CXB in absence of pre-dissolved polymers was collected. Concentrations of the dissolved drug were measured online via an 8453 UV/VIS spectrophotometer (Agilent, Waldbronn, Germany), including scattering correction for undissolved particles.

6.4. Preparation of formulations via hot-melt extrusion (HME)

The placebo extrudates and the ternary extruded ASDs (10% drug load) with 50:50 polymer mass ratio of EL 100-55 and HPC were prepared via HME, utilizing a 12 mm co-rotating twin screw extruder ZE 12 (Three-Tec GmbH, Seon, Switzerland) with a functional length of 25:1 L/D, a fixed screw configuration which is presented in Figure 50, and a 2 mm die. The five heating zones of the extruder were set to 40/75/150/150/150 °C.

Prior to the extrusion process, homogeneous PMs were prepared by using a Turbula® mixer (Willy A. Bachofen AG Maschinenfabrik, Switzerland) for 10 min, setting the rotation speed to 50 rpm. Subsequently, the homogeneous mixtures were fed constantly into the twin screw extruder with a rate of 2 g/min and processed with a screw speed of 100 rpm. The obtained extrudates were milled utilizing a MM400 ball mill (Retsch GmbH, Haan, Germany) with a frequency of 30 Hz. Milled extrudates with a size > 355 µm were removed by sieving and excluded from further analysis.

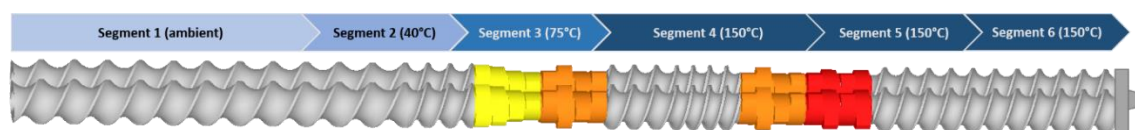


Figure 50: Fixed screw configuration of the twin screw extruder ZE 12 for preparing the HME placebo formulations and the ternary HME ASDs. The conveying elements (grey color) demonstrated 9, 12, and 18 mm pitches. The used kneading elements showed staggering angles of 30° (yellow color), 60° (orange color), and 90° (red color). The temperatures of the segments were selected to be of ambient temperature (segment 1), 40 °C (segment 2), 75 °C (segment 3), 150 °C (segment 4, 5 and 6). This figure was taken from Pöstges et al., 2023 [104].

6.5. Preparation of formulations via vacuum compression molding (VCM)

Prior to VCM processing, PMs were obtained by blending the components 3 x 5 min using a MM400 ball mill (Retsch GmbH, Haan, Germany), setting the frequency to 30 Hz.

Approx. 500 mg of the homogeneously milled PMs were loaded into the VCM device with a 20 mm disc geometry (MeltPrep GmbH, Graz, Austria). Subsequently, VCM discs were prepared by heating the mixtures for a pre-defined annealing temperature and annealing time under complete vacuum. While for the HME process (chapter 6.4.), generation of additional heat via the shear forces of the kneading elements was assumed, viscous

dissipation was not expected for the non-shear VCM process. Consequently, the VCM processing temperature was intensified by 10 °C, resulting in an annealing temperature of 160 °C for 15 min. After cooling for 10 min, the received ASD discs were milled using the MM400 ball mill (Retsch GmbH, Haan, Germany) at 30 Hz and passed through a sieve (mesh size 355 µm). To standardize the particle size for further investigations, larger particles were excluded.

6.6. Preparation of formulations via spray-drying (SD)

The components for placebo and ASD processing (10% drug load) with 50:50 polymer mass ratio of EL 100-55 and HPC were dissolved in ethanol 96% (v/v) and spray-dried utilizing a B290 mini spray dryer (BÜCHI, Essen, Germany), connected to an Inert Loop B-295 and a dehumidifier B-296 (BÜCHI, Flawil, Switzerland). The process was conducted by setting the inlet temperature to 90 °C, the spray gas flow of the inert drying gas nitrogen to 40 mm (473 L/h), the aspirator rate to 100% (35 m³/h), and the pump rate of the ethanolic solution to 5 mL/min.

After the SD process, the obtained powder was placed into a vacuum oven (Binder GmbH, Tuttlingen, Germany) to dry under vacuum for 24 h at 40 °C for removing residual ethanol.

6.7. Thermogravimetric analysis (TGA)

Thermostability investigations of raw materials were carried out using a TGA 7 (Perkin Elmer, Waltham, MA, USA), equipped with nitrogen as purge gas (20 mL/min). Approx. 5 mg of the samples were weighted into platinum crucibles and exposed to heat according to the selected temperature program.

The thermal stability of EL 100-55, HPC-SSL, HPC-UL, CXB, and EFV were investigated with respect to the VCM processing conditions of chapter 6.5. (160 °C, 15 min), as these processing conditions provided the highest heat stress on these substances in this thesis. Consequently, after heating the samples to 160 °C (10 °C/min), the weight loss [%] during a holding time of 15 min was determined.

6.8. Differential scanning calorimetry (DSC)

DSC analyses of the raw materials and of the processed formulations were carried out by utilizing a DSC 2 instrument (Mettler-Toledo, Gießen, Germany), equipped with nitrogen

as purge gas. To enable low starting temperatures a nitrogen cooling system was installed. Approx. 10 mg of the investigated samples were weighted accurately into an aluminum pan that was sealed with a pierced lid. The neat drugs were examined using a conventional method, consisting of a heating range from 0 to 200 °C for CXB and from 0 to 170 °C for EFV with a constant temperature rising of 10 °C/ min. For enhanced visualization of the glass transitions, the polymers and the ASDs were investigated in TOPEM-mode, a multi-frequency temperature-modulated program, setting the heating rate and the amplitude of the temperature pulse to 2 °C/ min and ± 0.5 , respectively. By applying temperature-modulated DSC, the heat flow can be split into the reversing and the non-reversing heat flow. Frequency-dependent effects (e.g., glass transitions) are visible in the reversing heat flow and can be easily distinguished from frequency-independent effects (e.g., loss of moisture) that would be present in the non-reversing heat flow. Consequently, potentially overlapping or interfering of frequency-independent effects for the detection of the glass transition can be prevented.

The neat polymers, the placebo formulations and the CXB formulations were investigated applying a heating range from 0 to 170 °C. For the EFV formulations, the end temperature of the TOPEM run was reduced to 150 °C.

The DSC investigations of the solid dispersions were carried out immediately after processing.

6.9. Confocal Raman spectroscopy (CRS)

Polymer mixing of the HME and VCM processed placebo formulations and the drug distributions within the VCM processed ternary ASDs were investigated via CRS using an alpha 300R confocal Raman microscope (WiTec, Ulm, Germany), equipped with a 532 nm excitation laser, an UHTS 300 spectrometer, a DV401-BV CCD camera and a 40x 0.6 NA objective. Before analyzing the formulations, Raman spectra of the neat substances were collected with an integration time of 2 s to identify characteristic Raman intensities and peak shapes for distinguishing the individual components in the formulations. The laser power was set to 25 mW for the neat polymers and CXB while it was reduced to 10 mW for neat EFV.

As a compromise between a sufficient sample size for investigating the solid-state of the polymers and drugs and an appropriate measuring time, the scanning cutout of the VCM

discs was selected to be 50 μm x 50 μm . To obtain a disc with uniform surface the milled HME placebo extrudates were processed to VCM discs using the same processing conditions, as described in chapter 6.5. Investigations of the VCM discs were conducted using the autofocus and setting the integration time to 0.5 s and the laser power to 25 mW. Color code images for the individual substances were created by measuring 50 points per line and 50 lines per image. Based on the intensities of the selected and representative wavenumbers, the distribution of the components within the investigated formulations (red color for the presence of EL 100-55, blue color for the presence of the HPC polymers, and green color for the presence of the drugs) was demonstrated. Accordingly, low color intensities/ black color revealed low content of the corresponding substance.

6.10. Melt rheology of neat polymers

Small amplitude oscillatory shear rheology of the neat polymers EL 100-55, HPC-SSL and HPC-UL were conducted utilizing a HAAKE MARS III (Thermo Scientific, Karlsruhe, Germany), installed with a 20 mm plate-plate geometry. VCM discs of the neat polymers were prepared, using the processing conditions as described in chapter 6.5. Before performing the experiments, the VCM discs were equilibrated at 160 °C for 10 min. Amplitude sweeps were conducted at 160 °C to determine amplitudes within the linear viscoelastic ranges for the subsequent frequency sweeps, leading to suitable amplitudes of 1.0% and 0.05% for EL 100-55 and the HPC polymers, respectively. The frequency sweeps were performed from 10 Hz (62.83 rad/s) to 0.1 Hz (0.63 rad/s) at 160 °C and the complex viscosities at 1 rad/s were calculated.

6.11. Fourier-transform infrared spectroscopy (FT-IR)

To examine the solid-state interactions (polymer-polymer and drug-polymer interactions) FT-IR measurements were conducted, using a Spectrum Two FT-IR spectrometer (PerkinElmer, Waltham, MA, USA). Spectra of the raw materials, PMs, and ASDs (10% drug load) were collected in a spectral range of 450- 4000 cm^{-1} .

6.12. X-Ray powder diffraction (XRPD)

The molecular structure (crystallinity or amorphousness) of the neat drugs and the investigated ASDs (10% drug load) were investigated via XRPD using an X' Pert MRD Pro

(PANalytical, Almelo, Netherlands). The investigations were conducted in reflection mode at 45 kV and 40 mA, using nickel-filtered CuK α 1 radiation and an X'Celerator detector. The diffractograms were collected in a 4- 45 ° 2 θ range with a step size of 0.017 ° 2 θ .

6.13. Non-sink dissolution study

The non-sink dissolution studies were performed for 180 min in 0.05 M phosphate buffer (pH 6.8) at 37 °C, setting the paddle speed to 75 rpm. Due to the small sample size of the VCM processed ASDs, the testing was carried out using the miniaturized USP dissolution apparatus II (MiniDissolution apparatus) with 20 mL dissolution medium for each vessel [149]. To enable high non-sink conditions for optimal evaluation of the dissolutions of the ASDs, a sample size related to 4 mg drug amount was chosen, leading to a theoretical concentration of 0.2 mg/mL in case of complete dissolution. The concentrations of dissolved drugs were measured online utilizing an 8453 UV/VIS spectrophotometer (Agilent, Waldbronn, Germany), considering correction in case of scattering.

6.14. Laser diffraction analysis

The particle size distributions of the ternary ASDs that were processed via SD were investigated using a Horiba LA-960 laser diffractometer (Horiba, Kyoto, Japan). Approx. 15 mL n-hexane with 0.1% Span 80 was filled into the quartz cuvette. The SD powders were suspended under stirring, followed by subsequent measurements of the particle sizes. A red laser diode with 650 nm wavelength (5 mW) and a blue light emitting diode with 405 nm wavelength (3 mW) were utilized as light sources.

7. Summary and outlook

The majority of newly developed drugs suffer from poor water solubility, resulting in only limited oral bioavailability. One promising principle to enhance oral exposure is the manufacturing of ASDs, where the drug is incorporated amorphously into a polymer matrix. An optimal ASD-forming polymer should prevent recrystallization of the amorphous drug within the solid dispersion, enable satisfied dissolution rate, and inhibit precipitation of the thermodynamic metastable supersaturated drug solution. However, both the stabilization of the amorphous drug in solid-state and in liquid-state depend on specific drug-polymer interactions, thus the correct ASD-forming polymer needs to be selected, carefully.

Focusing on the liquid-state interactions, the supersaturation testing illustrated the variability and diversity of precipitation inhibiting effects of different polymers on individual drugs. Next to EPO, no superior polymer that outperformed the alternatives for all investigated drugs was found. Mechanistically, the use of EPO was very interesting, as the amino groups of the polymer seemed to provide great interaction site for stabilizing the polymers. However, the actual insoluble character in pH 6.8 would lead to low concentration values upon dissolution of solid formulations, thus chemical adaption of the polymer to increase the solubility of EPO would be required. In order to extend the possibilities of promising supersaturation polymers, commercially available polymers can be combined. The potential of polymer blends was demonstrated, performing the supersaturation assay with polymer mixtures of EL 100-55 and HPC for CXB, EFV, and CLT. Although the single polymers alone showed only limited capability of stabilizing the supersaturated solutions, the polymer mixtures led to remarkable drug solubilities. Using CXB as drug substance, the main role of each polymer for the synergistic interplay in liquid-state was assigned, revealing EL 100-55 as responsible polymer for maximum solubility extent and HPC as precipitation inhibitor.

To continue designing supersaturating formulations, polymer placebo formulations (EL 100-55: HPC-SSL 50:50 and EL 100-55: HPC-UL 50:50) and ternary ASDs, comprising of either CXB or EFV as drug component (10% drug load), were prepared via VCM, HME, or SD. As VCM is regarded to be a tool for formulation screening of HME ASDs, the solid-states and dissolutions of the VCM and HME processed formulations were compared.

Manufacturing-dependent differences in phase homogeneity and solid-state interactions were demonstrated, resulting in single-phased formulations (HME) or in heterogeneous/phase separated formulations (VCM). Apparently, the missing shear forces during the VCM process prevented complete polymer mixing. Instead, EL 100-55-richer phases and HPC-richer phases were created, whereby higher kinetic solid-state solubility of the drugs within the HPC polymers compared to EL 100-55 led to higher drug distributions within the HPC-richer phases. Additionally, slight differences in extent of heterogeneity in the ternary VCM formulations were observed in dependence on the selected HPC grade. As HPC-UL exhibited decisive smaller melt viscosity under the VCM processing conditions than HPC-SSL, the formation of partially miscible phases between EL 100-55 and HPC-UL was facilitated.

As homogeneously mixed polymer phases were required for optimal extent of solubility improvement, the ternary HME ASDs consisting of EL 100-55: HPC-SSL outperformed the corresponding VCM formulations. However, the higher degree of partially miscible phases in the ternary VCM formulations using HPC-UL led to no or only negligible manufacturing-dependent dissolution differences.

Consequently, in case of processing of shear sensitive drugs, the selection of the lower melt viscosity HPC grade -UL is favorable, as higher degree of polymer mixing with EL 100-55 using lower shear rates can be achieved.

Nevertheless, although VCM provides easy and fast HME screening, the potential differences in solid-state with respect to two polymers/ ternary ASDs must be considered. In case of early formulation development and limited drug supply, VCM might be the only applicable preparation method. In this context it is important to emphasize that pre-extrusion of the polymers and subsequent embedding of the drug via VCM also led to single-phased ternary ASDs and “extrusion-like” dissolution results.

In addition to the heat-based manufacturing techniques, SD represented a solvent-based processing method to prepare ternary ASDs. Similar to the HME ASDs, the SD formulations demonstrated homogeneous and single-phased systems with pronounced polymer-polymer interactions. The dissolutions revealed promising supersaturation of CXB and EFV, independently on the selected HPC grade. Further downstream process (e.g., granulation) would be required for final conclusion and evaluation of the process.

Overall, this work clearly demonstrated the potential of polymer mixtures for developing supersaturating formulations.

Since the synergistic interplay between EL 100-55 and HPC was the main focus of this thesis, additional polymer combinations should be investigated to discover further unknown potential of already commercially available polymers.

References

1. Williams, H.D.; Trevaskis, N.L.; Charman, S.A.; Shanker, R.M.; Charman, W.N.; Pouton, C.W.; Porter, C.J.H. Strategies to Address Low Drug Solubility in Discovery and Development. *Pharmacol. Rev.* **2013**, *65*, 315–499, doi:10.1124/pr.112.005660.
2. Helen Chan, O.; Stewart, B.H. Physicochemical and Drug-Delivery Considerations for Oral Drug Bioavailability. *Drug Discov. Today* **1996**, *1*, 461–473, doi:10.1016/1359-6446(96)10039-8.
3. Pade, V.; Stavchansky, S. Link between Drug Absorption Solubility and Permeability Measurements in Caco-2 Cells. *J. Pharm. Sci.* **1998**, *87*, 1604–1607, doi:10.1021/js980111k.
4. Yan, Y.; Chen, J.-M.; Lu, T.-B. Simultaneously Enhancing the Solubility and Permeability of Acyclovir by Crystal Engineering Approach. *CrystEngComm* **2013**, *15*, 6457–6460, doi:10.1039/C3CE41017J.
5. Papich, M.G.; Martinez, M.N. Applying Biopharmaceutical Classification System (BCS) Criteria to Predict Oral Absorption of Drugs in Dogs: Challenges and Pitfalls. *AAPS J.* **2015**, *17*, 948–964, doi:10.1208/s12248-015-9743-7.
6. Amidon, G.L.; Lennernäs, H.; Shah, V.P.; Crison, J.R. A Theoretical Basis for a Biopharmaceutic Drug Classification: The Correlation of in Vitro Drug Product Dissolution and in Vivo Bioavailability. *Pharm. Res.* **1995**, *12*, 413–420, doi:10.1023/a:1016212804288.
7. Boyd, B.J.; Bergström, C.A.S.; Vinarov, Z.; Kuentz, M.; Brouwers, J.; Augustijns, P.; Brandl, M.; Bernkop-Schnürch, A.; Shrestha, N.; Prémat, V.; et al. Successful Oral Delivery of Poorly Water-Soluble Drugs Both Depends on the Intraluminal Behavior of Drugs and of Appropriate Advanced Drug Delivery Systems. *Eur. J. Pharm. Sci.* **2019**, *137*, 104967, doi:10.1016/j.ejps.2019.104967.
8. Hancock, B.C.; Parks, M. What Is the True Solubility Advantage for Amorphous Pharmaceuticals? *Pharm. Res.* **2000**, *17*, 397–404, doi:10.1023/a:1007516718048.
9. Singh, A.; Van den Mooter, G. Spray Drying Formulation of Amorphous Solid Dispersions. *Adv. Drug Deliv. Rev.* **2016**, *100*, 27–50, doi:10.1016/j.addr.2015.12.010.
10. Gupta, P.K. Non-Crystalline Solids: Glasses and Amorphous Solids. *J. Non-Cryst. Solids* **1996**, *195*, 158–164, doi:10.1016/0022-3093(95)00502-1.
11. Sun, Y.; Zhu, L.; Wu, T.; Cai, T.; Gunn, E.M.; Yu, L. Stability of Amorphous Pharmaceutical Solids: Crystal Growth Mechanisms and Effect of Polymer Additives. *AAPS J.* **2012**, *14*, 380–388, doi:10.1208/s12248-012-9345-6.
12. Bhujbal, S.V.; Pathak, V.; Zemlyanov, D.Y.; Taylor, L.S.; Zhou, Q.T. Physical Stability and Dissolution of Lumefantrine Amorphous Solid Dispersions Produced by Spray Anti-Solvent Precipitation. *J. Pharm. Sci.* **2021**, *110*, 2423–2431, doi:10.1016/j.xphs.2020.12.033.
13. Bookwala, M.; Wildfong, P.L.D. The Implications of Drug-Polymer Interactions on the Physical Stability of Amorphous Solid Dispersions. *Pharm. Res.* **2023**, doi:10.1007/s11095-023-03547-4.
14. Mohapatra, S.; Samanta, S.; Kothari, K.; Mistry, P.; Suryanarayanan, R. Effect of Polymer Molecular Weight on the Crystallization Behavior of Indomethacin

- Amorphous Solid Dispersions. *Cryst. Growth Des.* **2017**, *17*, 3142–3150, doi:10.1021/acs.cgd.7b00096.
15. Tao, J.; Sun, Y.; Zhang, G.G.Z.; Yu, L. Solubility of Small-Molecule Crystals in Polymers: D-Mannitol in PVP, Indomethacin in PVP/VA, and Nifedipine in PVP/VA. *Pharm. Res.* **2009**, *26*, 855–864, doi:10.1007/s11095-008-9784-z.
 16. Monschke, M.; Kayser, K.; Wagner, K.G. Processing of Polyvinyl Acetate Phthalate in Hot-Melt Extrusion—Preparation of Amorphous Solid Dispersions. *Pharmaceutics* **2020**, *12*, 337, doi:10.3390/pharmaceutics12040337.
 17. Wolbert, F.; Nikoleit, K.; Steinbrink, M.; Luebbert, C.; Sadowski, G. The Shelf Life of ASDs: 1. Measuring the Crystallization Kinetics at Humid Conditions. *Mol. Pharm.* **2022**, *19*, 2483–2494, doi:10.1021/acs.molpharmaceut.2c00188.
 18. Luebbert, C.; Real, D.; Sadowski, G. Choosing Appropriate Solvents for ASD Preparation. *Mol. Pharm.* **2018**, *15*, 5397–5409, doi:10.1021/acs.molpharmaceut.8b00892.
 19. Pandi, P.; Bulusu, R.; Kommineni, N.; Khan, W.; Singh, M. Amorphous Solid Dispersions: An Update for Preparation, Characterization, Mechanism on Bioavailability, Stability, Regulatory Considerations and Marketed Products. *Int. J. Pharm.* **2020**, *586*, 119560, doi:10.1016/j.ijpharm.2020.119560.
 20. Bhujbal, S.V.; Mitra, B.; Jain, U.; Gong, Y.; Agrawal, A.; Karki, S.; Taylor, L.S.; Kumar, S.; Zhou, Q.T. Pharmaceutical Amorphous Solid Dispersion: A Review of Manufacturing Strategies. *Acta Pharm. Sin. B* **2021**, *11*, 2505–2536, doi:10.1016/j.apsb.2021.05.014.
 21. Hwang, I.; Kang, C.-Y.; Park, J.-B. Advances in Hot-Melt Extrusion Technology toward Pharmaceutical Objectives. *J. Pharm. Investig.* **2017**, *47*, 123–132, doi:10.1007/s40005-017-0309-9.
 22. Crowley, M.M.; Zhang, F.; Repka, M.A.; Thumma, S.; Upadhye, S.B.; Kumar Battu, S.; McGinity, J.W.; Martin, C. Pharmaceutical Applications of Hot-Melt Extrusion: Part I. *Drug Dev. Ind. Pharm.* **2007**, *33*, 909–926, doi:10.1080/03639040701498759.
 23. Huang, D.; Xie, Z.; Rao, Q.; Lamas, E.; Pan, P.; Guan, S.; Zhang, Z.J.; Lu, M.; Li, Q. Hot Melt Extrusion of Heat-Sensitive and High Melting Point Drug: Inhibit the Recrystallization of the Prepared Amorphous Drug during Extrusion to Improve the Bioavailability. *Int. J. Pharm.* **2019**, *565*, 316–324, doi:10.1016/j.ijpharm.2019.04.064.
 24. Zecevic, D.E.; Evans, R.C.; Paulsen, K.; Wagner, K.G. From Benchtop to Pilot Scale—Experimental Study and Computational Assessment of a Hot-Melt Extrusion Scale-up of a Solid Dispersion of Dipyridamole and Copovidone. *Int. J. Pharm.* **2018**, *537*, 132–139, doi:10.1016/j.ijpharm.2017.12.033.
 25. Moseson, D.E.; Taylor, L.S. The Application of Temperature-Composition Phase Diagrams for Hot Melt Extrusion Processing of Amorphous Solid Dispersions to Prevent Residual Crystallinity. *Int. J. Pharm.* **2018**, *553*, 454–466, doi:10.1016/j.ijpharm.2018.10.055.
 26. Shah, S.; Maddineni, S.; Lu, J.; Repka, M.A. Melt Extrusion with Poorly Soluble Drugs. *Int. J. Pharm.* **2013**, *453*, 233–252, doi:10.1016/j.ijpharm.2012.11.001.
 27. Mathers, A.; Hassouna, F.; Malinová, L.; Merna, J.; Růžička, K.; Fulem, M. Impact of Hot-Melt Extrusion Processing Conditions on Physicochemical Properties of

- Amorphous Solid Dispersions Containing Thermally Labile Acrylic Copolymer. *J. Pharm. Sci.* **2020**, *109*, 1008–1019, doi:10.1016/j.xphs.2019.10.005.
28. Censi, R.; Gigliobianco, M.R.; Casadidio, C.; Di Martino, P. Hot Melt Extrusion: Highlighting Physicochemical Factors to Be Investigated While Designing and Optimizing a Hot Melt Extrusion Process. *Pharmaceutics* **2018**, *10*, 89, doi:10.3390/pharmaceutics10030089.
 29. Monschke, M.; Kayser, K.; Wagner, K.G. Influence of Particle Size and Drug Load on Amorphous Solid Dispersions Containing pH-Dependent Soluble Polymers and the Weak Base Ketoconazole. *AAPS PharmSciTech* **2021**, *22*, 44, doi:10.1208/s12249-020-01914-7.
 30. Evans, R.C.; Bochmann, E.S.; Kyeremateng, S.O.; Gryczke, A.; Wagner, K.G. Holistic QbD Approach for Hot-Melt Extrusion Process Design Space Evaluation: Linking Materials Science, Experimentation and Process Modeling. *Eur. J. Pharm. Biopharm.* **2019**, *141*, 149–160, doi:10.1016/j.ejpb.2019.05.021.
 31. Ayoub, A.; Treasure, T.; Hansen, L.; Nypelö, T.; Jameel, H.; Khan, S.; Chang, H.; Hubbe, M.A.; Venditti, R.A. Effect of Plasticizers and Polymer Blends for Processing Softwood Kraft Lignin as Carbon Fiber Precursors. *Cellulose* **2021**, *28*, 1039–1053, doi:10.1007/s10570-020-03571-2.
 32. Patil, H.; Tiwari, R.V.; Repka, M.A. Hot-Melt Extrusion: From Theory to Application in Pharmaceutical Formulation. *AAPS PharmSciTech* **2015**, *17*, 20–42, doi:10.1208/s12249-015-0360-7.
 33. Dauer, K.; Wagner, K.G. Micro-Scale Vacuum Compression Molding as a Predictive Screening Tool of Protein Integrity for Potential Hot-Melt Extrusion Processes. *Pharmaceutics* **2023**, *15*, 723, doi:10.3390/pharmaceutics15030723.
 34. Shadambikar, G.; Kipping, T.; Di-Gallo, N.; Elia, A.-G.; Knüttel, A.-N.; Treffer, D.; Repka, M.A. Vacuum Compression Molding as a Screening Tool to Investigate Carrier Suitability for Hot-Melt Extrusion Formulations. *Pharmaceutics* **2020**, *12*, 1019, doi:10.3390/pharmaceutics12111019.
 35. Pöstges, F.; Kayser, K.; Appelhaus, J.; Monschke, M.; Gütschow, M.; Steinebach, C.; Wagner, K.G. Solubility Enhanced Formulation Approaches to Overcome Oral Delivery Obstacles of PROTACs. *Pharmaceutics* **2023**, *15*, 156, doi:10.3390/pharmaceutics15010156.
 36. Treffer, D.; Troiss, A.; Khinast, J. A Novel Tool to Standardize Rheology Testing of Molten Polymers for Pharmaceutical Applications. *Int. J. Pharm.* **2015**, *495*, 474–481, doi:10.1016/j.ijpharm.2015.09.001.
 37. Kayser, K.; Monschke, M.; Wagner, K.G. ASD Formation Prior to Material Characterization as Key Parameter for Accurate Measurements and Subsequent Process Simulation for Hot-Melt Extrusion. *AAPS PharmSciTech* **2022**, *23*, 176, doi:10.1208/s12249-022-02331-8.
 38. Szabó, E.; Démuth, B.; Galata, D.L.; Vass, P.; Hirsch, E.; Csontos, I.; Marosi, G.; Nagy, Z.K. Continuous Formulation Approaches of Amorphous Solid Dispersions: Significance of Powder Flow Properties and Feeding Performance. *Pharmaceutics* **2019**, *11*, 654, doi:10.3390/pharmaceutics11120654.
 39. Baumann, J.M.; Adam, M.S.; Wood, J.D. Engineering Advances in Spray Drying for Pharmaceuticals. *Annu. Rev. Chem. Biomol. Eng.* **2021**, *12*, 217–240, doi:10.1146/annurev-chembioeng-091720-034106.

40. Li, N.; Cape, J.L.; Mankani, B.R.; Zemlyanov, D.Y.; Shepard, K.B.; Morgen, M.M.; Taylor, L.S. Water-Induced Phase Separation of Spray-Dried Amorphous Solid Dispersions. *Mol. Pharm.* **2020**, *17*, 4004–4017, doi:10.1021/acs.molpharmaceut.0c00798.
41. Szabó, E.; Záhonyi, P.; Brecska, D.; Galata, D.L.; Mészáros, L.A.; Madarász, L.; Csorba, K.; Vass, P.; Hirsch, E.; Szafraniec-Szczęsny, J.; et al. Comparison of Amorphous Solid Dispersions of Spironolactone Prepared by Spray Drying and Electrospinning: The Influence of the Preparation Method on the Dissolution Properties. *Mol. Pharm.* **2021**, *18*, 317–327, doi:10.1021/acs.molpharmaceut.0c00965.
42. Schönfeld, B.; Westedt, U.; Wagner, K.G. Vacuum Drum Drying – A Novel Solvent-Evaporation Based Technology to Manufacture Amorphous Solid Dispersions in Comparison to Spray Drying and Hot Melt Extrusion. *Int. J. Pharm.* **2021**, *596*, 120233, doi:10.1016/j.ijpharm.2021.120233.
43. Shepard, K.B.; Dower, A.M.; Ekdahl, A.M.; Morgen, M.M.; Baumann, J.M.; Vodak, D.T. Solvent-Assisted Secondary Drying of Spray-Dried Polymers. *Pharm. Res.* **2020**, *37*, 156, doi:10.1007/s11095-020-02890-0.
44. Jain, S.; Patel, N.; Lin, S. Solubility and Dissolution Enhancement Strategies: Current Understanding and Recent Trends. *Drug Dev. Ind. Pharm.* **2015**, *41*, 875–887, doi:10.3109/03639045.2014.971027.
45. Budiman, A.; Lailasari, E.; Nurani, N.V.; Yunita, E.N.; Anastasya, G.; Aulia, R.N.; Lestari, I.N.; Subra, L.; Aulifa, D.L. Ternary Solid Dispersions: A Review of the Preparation, Characterization, Mechanism of Drug Release, and Physical Stability. *Pharmaceutics* **2023**, *15*, 2116, doi:10.3390/pharmaceutics15082116.
46. Box, K.J.; Völgyi, G.; Baka, E.; Stuart, M.; Takács-Novák, K.; Comer, J.E.A. Equilibrium versus Kinetic Measurements of Aqueous Solubility, and the Ability of Compounds to Supersaturate in Solution—a Validation Study. *J. Pharm. Sci.* **2006**, *95*, 1298–1307, doi:10.1002/jps.20613.
47. López Mármol, Á.; Denninger, A.; Touzet, A.; Dauer, K.; Becker, T.; Pöstges, F.; Pellequer, Y.; Lamprecht, A.; Wagner, K.G. The Relevance of Supersaturation and Solubilization in the Gastrointestinal Tract for Oral Bioavailability: An in Vitro vs. in Vivo Approach. *Int. J. Pharm.* **2021**, *603*, 120648, doi:10.1016/j.ijpharm.2021.120648.
48. Brouwers, J.; Brewster, M.E.; Augustijns, P. Supersaturating Drug Delivery Systems: The Answer to Solubility-Limited Oral Bioavailability? *J. Pharm. Sci.* **2009**, *98*, 2549–2572, doi:10.1002/jps.21650.
49. Fong, S.Y.K.; Bauer-Brandl, A.; Brandl, M. Oral Bioavailability Enhancement through Supersaturation: An Update and Meta-Analysis. *Expert Opin. Drug Deliv.* **2017**, *14*, 403–426, doi:10.1080/17425247.2016.1218465.
50. Gan, Y.; Baak, J.P.A.; Chen, T.; Ye, H.; Liao, W.; Lv, H.; Wen, C.; Zheng, S. Supersaturation and Precipitation Applied in Drug Delivery Systems: Development Strategies and Evaluation Approaches. *Molecules* **2023**, *28*, 2212, doi:10.3390/molecules28052212.
51. Yang, M.; Gong, W.; Wang, Y.; Shan, L.; Li, Y.; Gao, C. Bioavailability Improvement Strategies for Poorly Water-Soluble Drugs Based on the Supersaturation Mechanism: An Update. *J. Pharm. Pharm. Sci.* **2016**, *19*, 208–225, doi:10.18433/J3W904.

52. Neuwirth, M.; Kappes, S.K.; Hartig, M.U.; Wagner, K.G. Amorphous Solid Dispersions Layered onto Pellets—An Alternative to Spray Drying? *Pharmaceutics* **2023**, *15*, 764, doi:10.3390/pharmaceutics15030764.
53. Price, D.J.; Ditzinger, F.; Koehl, N.J.; Jankovic, S.; Tsakiridou, G.; Nair, A.; Holm, R.; Kuentz, M.; Dressman, J.B.; Saal, C. Approaches to Increase Mechanistic Understanding and Aid in the Selection of Precipitation Inhibitors for Supersaturating Formulations - a PEARRL Review. *J. Pharm. Pharmacol.* **2019**, *71*, 483–509, doi:10.1111/jphp.12927.
54. Raina, S.A.; Van Eerdenbrugh, B.; Alonzo, D.E.; Mo, H.; Zhang, G.G.Z.; Gao, Y.; Taylor, L.S. Trends in the Precipitation and Crystallization Behavior of Supersaturated Aqueous Solutions of Poorly Water-Soluble Drugs Assessed Using Synchrotron Radiation. *J. Pharm. Sci.* **2015**, *104*, 1981–1992, doi:10.1002/jps.24423.
55. Warren, D.B.; Benameur, H.; Porter, C.J.H.; Pouton, C.W. Using Polymeric Precipitation Inhibitors to Improve the Absorption of Poorly Water-Soluble Drugs: A Mechanistic Basis for Utility. *J. Drug Target.* **2010**, *18*, 704–731, doi:10.3109/1061186X.2010.525652.
56. Lindfors, L.; Forssén, S.; Westergren, J.; Olsson, U. Nucleation and Crystal Growth in Supersaturated Solutions of a Model Drug. *J. Colloid Interface Sci.* **2008**, *325*, 404–413, doi:10.1016/j.jcis.2008.05.034.
57. Guzmán, H.R.; Tawa, M.; Zhang, Z.; Ratanabanangkoon, P.; Shaw, P.; Gardner, C.R.; Chen, H.; Moreau, J.; Almarsson, Ö.; Remenar, J.F. Combined Use of Crystalline Salt Forms and Precipitation Inhibitors to Improve Oral Absorption of Celecoxib from Solid Oral Formulations. *J. Pharm. Sci.* **2007**, *96*, 2686–2702, doi:10.1002/jps.20906.
58. Gao, P.; Akrami, A.; Alvarez, F.; Hu, J.; Li, L.; Ma, C.; Surapaneni, S. Characterization and Optimization of AMG 517 Supersaturatable Self-Emulsifying Drug Delivery System (S-SEDDS) for Improved Oral Absorption. *J. Pharm. Sci.* **2009**, *98*, 516–528, doi:10.1002/jps.21451.
59. Ziller, K.H.; Rupprecht, H. Control of Crystal Growth in Drug Suspensions: 1) Design of a Control Unit and Application to Acetaminophen Suspensions). *Drug Dev. Ind. Pharm.* **1988**, *14*, 2341–2370, doi:10.3109/03639048809152019.
60. Ilevbare, G.A.; Taylor, L.S. Liquid–Liquid Phase Separation in Highly Supersaturated Aqueous Solutions of Poorly Water-Soluble Drugs: Implications for Solubility Enhancing Formulations. *Cryst. Growth Des.* **2013**, *13*, 1497–1509, doi:10.1021/cg301679h.
61. Indulkar, A.S.; Gao, Y.; Raina, S.A.; Zhang, G.G.Z.; Taylor, L.S. Exploiting the Phenomenon of Liquid–Liquid Phase Separation for Enhanced and Sustained Membrane Transport of a Poorly Water-Soluble Drug. *Mol. Pharm.* **2016**, *13*, 2059–2069, doi:10.1021/acs.molpharmaceut.6b00202.
62. Suzuki, K.; Kawakami, K.; Fukiage, M.; Oikawa, M.; Nishida, Y.; Matsuda, M.; Fujita, T. Relevance of Liquid–Liquid Phase Separation of Supersaturated Solution in Oral Absorption of Albendazole from Amorphous Solid Dispersions. *Pharmaceutics* **2021**, *13*, 220, doi:10.3390/pharmaceutics13020220.
63. Indulkar, A.S.; Box, K.J.; Taylor, R.; Ruiz, R.; Taylor, L.S. pH-Dependent Liquid–Liquid Phase Separation of Highly Supersaturated Solutions of Weakly Basic Drugs. *Mol. Pharm.* **2015**, *12*, 2365–2377, doi:10.1021/acs.molpharmaceut.5b00056.

64. Hirlak, O.; Dieluweit, S.; Merkel, R.; Wagner, K.G. Polymer-Mediated Drug Supersaturation – A Spotlight on the Interplay between Phase-Separated Amorphous Drug Colloids and Dissolved Molecules. *J. Colloid Interface Sci.* **2021**, *603*, 370–379, doi:10.1016/j.jcis.2021.06.089.
65. Monschke, M.; Wagner, K.G. Impact of HPMCAS on the Dissolution Performance of Polyvinyl Alcohol Celecoxib Amorphous Solid Dispersions. *Pharmaceutics* **2020**, *12*, 541, doi:10.3390/pharmaceutics12060541.
66. Ueda, K.; Higashi, K.; Moribe, K. Mechanistic Elucidation of Formation of Drug-Rich Amorphous Nanodroplets by Dissolution of the Solid Dispersion Formulation. *Int. J. Pharm.* **2019**, *561*, 82–92, doi:10.1016/j.ijpharm.2019.02.034.
67. Plum, J.; Bavnhøj, C.G.; Eliassen, J.N.; Rades, T.; Müllertz, A. Comparison of Induction Methods for Supersaturation: Amorphous Dissolution versus Solvent Shift. *Eur. J. Pharm. Biopharm.* **2020**, *152*, 35–43, doi:10.1016/j.ejpb.2020.04.017.
68. Sun, D.D.; Wen, H.; Taylor, L.S. Non-Sink Dissolution Conditions for Predicting Product Quality and In Vivo Performance of Supersaturating Drug Delivery Systems. *J. Pharm. Sci.* **2016**, *105*, 2477–2488, doi:10.1016/j.xphs.2016.03.024.
69. Qin, Y.; Xiao, C.; Li, X.; Huang, J.; Si, L.; Sun, M. Enteric Polymer-Based Amorphous Solid Dispersions Enhance Oral Absorption of the Weakly Basic Drug Nintedanib via Stabilization of Supersaturation. *Pharmaceutics* **2022**, *14*, 1830, doi:10.3390/pharmaceutics14091830.
70. Hirai, D.; Tsunematsu, H.; Kimura, S.; Itai, S.; Fukami, T.; Iwao, Y. Theoretical Evaluation of Supersaturation of Amorphous Solid Dispersion Formulations with Different Drug/Polymer Combinations Using Mathematical Modeling. *Int. J. Pharm.* **2022**, *625*, 122110, doi:10.1016/j.ijpharm.2022.122110.
71. Higashi, K.; Ueda, K.; Moribe, K. Intermolecular Interactions between Drugs and Aminoalkyl Methacrylate Copolymer in Solution to Enhance the Concentration of Poorly Water-Soluble Drugs. *Chem. Pharm. Bull. (Tokyo)* **2019**, *67*, 906–914, doi:10.1248/cpb.c18-00849.
72. Lee, D.; Ha, E.-S.; Ha, D.-H.; Sim, W.-Y.; Choi, J.-E.; Kim, M.-S.; Cho, C.-W.; Hwang, S.-J. Effect of Polymer Type on the Dissolution Profile of a Solid Dispersion of Cilostazol. *Bull. Korean Chem. Soc.* **2019**, *40*, 370–373, doi:10.1002/bkcs.11683.
73. Yoshida, T.; Kurimoto, I.; Yoshihara, K.; Umejima, H.; Ito, N.; Watanabe, S.; Sako, K.; Kikuchi, A. Effect of Aminoalkyl Methacrylate Copolymer E/ HCl on in Vivo Absorption of Poorly Water-Soluble Drug. *Drug Dev. Ind. Pharm.* **2013**, *39*, 1698–1705, doi:10.3109/03639045.2012.730525.
74. Yoshida, T.; Kurimoto, I.; Umejima, H.; Watanabe, S.; Sako, K.; Kikuchi, A. Effects of Dissolved State of Aminoalkyl Methacrylate Copolymer E/HCl on Solubility Enhancement Effect for Poorly Water-Soluble Drugs. *Colloid Polym. Sci.* **2013**, *291*, 1191–1199, doi:10.1007/s00396-012-2848-y.
75. Yoshida, T.; Kurimoto, I.; Yoshihara, K.; Umejima, H.; Ito, N.; Watanabe, S.; Sako, K.; Kikuchi, A. Aminoalkyl Methacrylate Copolymers for Improving the Solubility of Tacrolimus. I: Evaluation of Solid Dispersion Formulations. *Int. J. Pharm.* **2012**, *428*, 18–24, doi:10.1016/j.ijpharm.2012.02.041.
76. Miller, D.A.; DiNunzio, J.C.; Yang, W.; McGinity, J.W.; Williams III, R.O. Enhanced In Vivo Absorption of Itraconazole via Stabilization of Supersaturation Following Acidic-to-Neutral pH Transition. *Drug Dev. Ind. Pharm.* **2008**, *34*, 890–902, doi:10.1080/03639040801929273.

77. Niederquell, A.; Stoyanov, E.; Kuentz, M. Hydroxypropyl Cellulose for Drug Precipitation Inhibition: From the Potential of Molecular Interactions to Performance Considering Microrheology. *Mol. Pharm.* **2022**, *19*, 690–703, doi:10.1021/acs.molpharmaceut.1c00832.
78. Ilevbare, G.A.; Liu, H.; Edgar, K.J.; Taylor, L.S. Maintaining Supersaturation in Aqueous Drug Solutions: Impact of Different Polymers on Induction Times. *Cryst. Growth Des.* **2013**, *13*, 740–751, doi:10.1021/cg301447d.
79. Ilevbare, G.A.; Liu, H.; Edgar, K.J.; Taylor, L.S. Understanding Polymer Properties Important for Crystal Growth Inhibition—Impact of Chemically Diverse Polymers on Solution Crystal Growth of Ritonavir. *Cryst. Growth Des.* **2012**, *12*, 3133–3143, doi:10.1021/cg300325p.
80. Ayrancı, E.; Büyüktaş, B.Ş.; Çetin, E.E. The Effect of Molecular Weight of Constituents on Properties of Cellulose-Based Edible Films. *LWT - Food Sci. Technol.* **1997**, *30*, 101–104, doi:10.1006/fstl.1996.0140.
81. Song, Y.; Wang, L.; Yang, P.; Wenslow Jr., R.M.; Tan, B.; Zhang, H.; Deng, Z. Physicochemical Characterization of Felodipine-Kollidon VA64 Amorphous Solid Dispersions Prepared by Hot-Melt Extrusion. *J. Pharm. Sci.* **2013**, *102*, 1915–1923, doi:10.1002/jps.23538.
82. Chen, Y.; Pui, Y.; Chen, H.; Wang, S.; Serno, P.; Tonnis, W.; Chen, L.; Qian, F. Polymer-Mediated Drug Supersaturation Controlled by Drug–Polymer Interactions Persisting in an Aqueous Environment. *Mol. Pharm.* **2019**, *16*, 205–213, doi:10.1021/acs.molpharmaceut.8b00947.
83. Pöstges, F.; Kayser, K.; Stoyanov, E.; Wagner, K.G. Boost of Solubility and Supersaturation of Celecoxib via Synergistic Interactions of Methacrylic Acid-Ethyl Acrylate Copolymer (1:1) and Hydroxypropyl Cellulose in Ternary Amorphous Solid Dispersions. *Int. J. Pharm. X* **2022**, *4*, 100115, doi:10.1016/j.ijpx.2022.100115.
84. Luebbert, C.; Stoyanov, E.; Sadowski, G. Phase Behavior of ASDs Based on Hydroxypropyl Cellulose. *Int. J. Pharm. X* **2020**, *3*, 100070, doi:10.1016/j.ijpx.2020.100070.
85. Monschke, M.; Wagner, K.G. Amorphous Solid Dispersions of Weak Bases with pH-Dependent Soluble Polymers to Overcome Limited Bioavailability Due to Gastric pH Variability – An in-Vitro Approach. *Int. J. Pharm.* **2019**, *564*, 162–170, doi:10.1016/j.ijpharm.2019.04.034.
86. Sakamoto, N.; Stoyanov, E. Differential Analysis of O-(2- Hydroxypropyl) Cellulose by Using Two-Dimensional ¹H-NMR Spectroscopy. *Arch. Biomed. Sci. Eng.* **2020**, *6*, 010–015, doi:10.17352/abse.000015.
87. Paul, D.R.; Barlow, J.W. Polymer Blends. *J. Macromol. Sci. Part C* **1980**, *18*, 109–168, doi:10.1080/00222358008080917.
88. Olabisi, O. Interpretations of Polymer-Polymer Miscibility. *J. Chem. Educ.* **1981**, *58*, 944, doi:10.1021/ed058p944.
89. S. Muzata, T.; P. L, J.; Bose, S. Nanoparticles Influence Miscibility in LCST Polymer Blends: From Fundamental Perspective to Current Applications. *Phys. Chem. Chem. Phys.* **2020**, *22*, 20167–20188, doi:10.1039/D0CP01814G.
90. Parameswaranpillai, J.; Thomas, S.; Grohens, Y. Polymer Blends: State of the Art, New Challenges, and Opportunities (Eds Thomas, S.; Grohens, Y.; Jyotishkumar, P.). *Charact. Polym. Blends* **2014**, 1–6, doi:10.1002/9783527645602.ch01.

91. Lyu, S.-P.; Sparer, R.; Hobot, C.; Dang, K. Adjusting Drug Diffusivity Using Miscible Polymer Blends. *J. Controlled Release* **2005**, *102*, 679–687, doi:10.1016/j.jconrel.2004.11.007.
92. Higgins, J.S.; Lipson, J.E.G.; White, R.P. A Simple Approach to Polymer Mixture Miscibility. *Philos. Transact. A Math. Phys. Eng. Sci.* **2010**, *368*, 1009–1025, doi:10.1098/rsta.2009.0215.
93. Muthuraj, R.; Hajee, M.; Horrocks, A.R.; Kandola, B.K. Biopolymer Blends from Hardwood Lignin and Bio-Polyamides: Compatibility and Miscibility. *Int. J. Biol. Macromol.* **2019**, *132*, 439–450, doi:10.1016/j.ijbiomac.2019.03.142.
94. Thakral, S.; Thakral, N.K. Prediction of Drug–Polymer Miscibility through the Use of Solubility Parameter Based Flory–Huggins Interaction Parameter and the Experimental Validation: PEG as Model Polymer. *J. Pharm. Sci.* **2013**, *102*, 2254–2263, doi:10.1002/jps.23583.
95. Sarpal, K.; Tower, C.W.; Munson, E.J. Investigation into Intermolecular Interactions and Phase Behavior of Binary and Ternary Amorphous Solid Dispersions of Ketoconazole. *Mol. Pharm.* **2020**, *17*, 787–801, doi:10.1021/acs.molpharmaceut.9b00970.
96. Butreddy, A. Hydroxypropyl Methylcellulose Acetate Succinate as an Exceptional Polymer for Amorphous Solid Dispersion Formulations: A Review from Bench to Clinic. *Eur. J. Pharm. Biopharm.* **2022**, *177*, 289–307, doi:10.1016/j.ejpb.2022.07.010.
97. Nyamweya, N.; Hoag, S.W. Assessment of Polymer-Polymer Interactions in Blends of HPMC and Film Forming Polymers by Modulated Temperature Differential Scanning Calorimetry. *Pharm. Res.* **2000**, *17*, 625–631, doi:10.1023/A:1007585403781.
98. Fekete, E.; Földes, E.; Pukánszky, B. Effect of Molecular Interactions on the Miscibility and Structure of Polymer Blends. *Eur. Polym. J.* **2005**, *41*, 727–736, doi:10.1016/j.eurpolymj.2004.10.038.
99. Luebbert, C.; Klanke, C.; Sadowski, G. Investigating Phase Separation in Amorphous Solid Dispersions via Raman Mapping. *Int. J. Pharm.* **2018**, *535*, 245–252, doi:10.1016/j.ijpharm.2017.11.014.
100. Breitenbach, J.; Schrof, W.; Neumann, J. Confocal Raman-Spectroscopy: Analytical Approach to Solid Dispersions and Mapping of Drugs. *Pharm. Res.* **1999**, *16*, 1109–1113, doi:10.1023/A:1018956304595.
101. Thabet, Y.; Lunter, D.; Breitzkreutz, J. Continuous Manufacturing and Analytical Characterization of Fixed-Dose, Multilayer Orodispersible Films. *Eur. J. Pharm. Sci.* **2018**, *117*, 236–244, doi:10.1016/j.ejps.2018.02.030.
102. Wei, D.; Chen, S.; Liu, Q. Review of Fluorescence Suppression Techniques in Raman Spectroscopy. *Appl. Spectrosc. Rev.* **2015**, *50*, 387–406, doi:10.1080/05704928.2014.999936.
103. Doherty, C.; York, P. Evidence for Solid- and Liquid-State Interactions in a Furosemide-Polyvinylpyrrolidone Solid Dispersion. *J. Pharm. Sci.* **1987**, *76*, 731–737, doi:10.1002/jps.2600760912.
104. Pöstges, F.; Lenhart, J.; Stoyanov, E.; Lunter, D.J.; Wagner, K.G. Phase Homogeneity in Ternary Amorphous Solid Dispersions and Its Impact on Solubility, Dissolution and Supersaturation – Influence of Processing and Hydroxypropyl Cellulose Grade. *Int. J. Pharm. X* **2023**, *6*, 100222, doi:10.1016/j.ijpx.2023.100222.

105. Xu, X.; Chen, J.; An, L. Shear Thinning Behavior of Linear Polymer Melts under Shear Flow via Nonequilibrium Molecular Dynamics. *J. Chem. Phys.* **2014**, *140*, 174902, doi:10.1063/1.4873709.
106. Alsulays, B.B.; Park, J.-B.; Alshehri, S.M.; Morott, J.T.; Alshahrani, S.M.; Tiwari, R.V.; Alshetaili, A.S.; Majumdar, S.; Langley, N.; Kolter, K.; et al. Influence of Molecular Weight of Carriers and Processing Parameters on the Extrudability, Drug Release, and Stability of Fenofibrate Formulations Processed by Hot-Melt Extrusion. *J. Drug Deliv. Sci. Technol.* **2015**, *29*, 189–198, doi:10.1016/j.jddst.2015.07.011.
107. Thumma, S.; Majumdar, S.; ElSohly, M.A.; Gul, W.; Repka, M.A. Preformulation Studies of a Prodrug of Δ^9 -Tetrahydrocannabinol. *AAPS PharmSciTech* **2008**, *9*, 982–990, doi:10.1208/s12249-008-9136-7.
108. Shi, Y.; Li, Z.; Sun, H.; Huang, S.; Zeng, F. Effect of the Properties of the Polymer Materials on the Quality of Selective Laser Sintering Parts. *Proc. Inst. Mech. Eng. Part J. Mater. Des. Appl.* **2004**, *218*, 247–252, doi:10.1177/146442070421800308.
109. He, Y.; Ho, C. Amorphous Solid Dispersions: Utilization and Challenges in Drug Discovery and Development. *J. Pharm. Sci.* **2015**, *104*, 3237–3258, doi:10.1002/jps.24541.
110. Wlodarski, K.; Zhang, F.; Liu, T.; Sawicki, W.; Kipping, T. Synergistic Effect of Polyvinyl Alcohol and Copovidone in Itraconazole Amorphous Solid Dispersions. *Pharm. Res.* **2018**, *35*, 16, doi:10.1007/s11095-017-2313-1.
111. Sun, D.D.; Lee, P.I. Evolution of Supersaturation of Amorphous Pharmaceuticals: The Effect of Rate of Supersaturation Generation. *Mol. Pharm.* **2013**, *10*, 4330–4346, doi:10.1021/mp400439q.
112. Müller, M.; Wiedey, R.; Hoheisel, W.; Serno, P.; Breitzkreutz, J. Impact of Co-Administered Stabilizers on the Biopharmaceutical Performance of Regorafenib Amorphous Solid Dispersions. *Eur. J. Pharm. Biopharm.* **2021**, *169*, 189–199, doi:10.1016/j.ejpb.2021.10.012.
113. Xie, T.; Taylor, L.S. Dissolution Performance of High Drug Loading Celecoxib Amorphous Solid Dispersions Formulated with Polymer Combinations. *Pharm. Res.* **2016**, *33*, 739–750, doi:10.1007/s11095-015-1823-y.
114. Xie, T.; Gao, W.; Taylor, L.S. Impact of Eudragit EPO and Hydroxypropyl Methylcellulose on Drug Release Rate, Supersaturation, Precipitation Outcome and Redissolution Rate of Indomethacin Amorphous Solid Dispersions. *Int. J. Pharm.* **2017**, *531*, 313–323, doi:10.1016/j.ijpharm.2017.08.099.
115. Xie, T.; Taylor, L.S. Improved Release of Celecoxib from High Drug Loading Amorphous Solid Dispersions Formulated with Polyacrylic Acid and Cellulose Derivatives. *Mol. Pharm.* **2016**, *13*, 873–884, doi:10.1021/acs.molpharmaceut.5b00798.
116. Bachmaier, R.D.; Monschke, M.; Faber, T.; Krome, A.K.; Pellequer, Y.; Stoyanov, E.; Lamprecht, A.; Wagner, K.G. In Vitro and in Vivo Assessment of Hydroxypropyl Cellulose as Functional Additive for Enabling Formulations Containing Itraconazole. *Int. J. Pharm. X* **2021**, *3*, 100076, doi:10.1016/j.ijpx.2021.100076.
117. Kapote, D.N.; Wagner, K.G. Influence of Shellac on the Improvement of Solubility and Supersaturation of Loratadine Amorphous Solid Dispersion Using a New Grade of HPMC. *J. Drug Deliv. Sci. Technol.* **2021**, *61*, 102116, doi:10.1016/j.jddst.2020.102116.

118. Van Ngo, H.; Nguyen, P.K.; Van Vo, T.; Duan, W.; Tran, V.-T.; Tran, P.H.-L.; Tran, T.T.-D. Hydrophilic-Hydrophobic Polymer Blend for Modulation of Crystalline Changes and Molecular Interactions in Solid Dispersion. *Int. J. Pharm.* **2016**, *513*, 148–152, doi:10.1016/j.ijpharm.2016.09.017.
119. Baghel, S.; Cathcart, H.; O'Reilly, N.J. Investigation into the Solid-State Properties and Dissolution Profile of Spray-Dried Ternary Amorphous Solid Dispersions: A Rational Step toward the Design and Development of a Multicomponent Amorphous System. *Mol. Pharm.* **2018**, *15*, 3796–3812, doi:10.1021/acs.molpharmaceut.8b00306.
120. Butreddy, A.; Sarabu, S.; Almutairi, M.; Ajjarapu, S.; Kolimi, P.; Bandari, S.; Repka, M.A. Hot-Melt Extruded Hydroxypropyl Methylcellulose Acetate Succinate Based Amorphous Solid Dispersions: Impact of Polymeric Combinations on Supersaturation Kinetics and Dissolution Performance. *Int. J. Pharm.* **2022**, *615*, 121471, doi:10.1016/j.ijpharm.2022.121471.
121. Zecevic, D.E.; Meier, R.; Daniels, R.; Wagner, K.-G. Site Specific Solubility Improvement Using Solid Dispersions of HPMC-AS/HPC SSL – Mixtures. *Eur. J. Pharm. Biopharm.* **2014**, *87*, 264–270, doi:10.1016/j.ejpb.2014.03.018.
122. Prasad, D.; Chauhan, H.; Atef, E. Amorphous Stabilization and Dissolution Enhancement of Amorphous Ternary Solid Dispersions: Combination of Polymers Showing Drug–Polymer Interaction for Synergistic Effects. *J. Pharm. Sci.* **2014**, *103*, 3511–3523, doi:10.1002/jps.24137.
123. Guo, Z.; Lu, M.; Li, Y.; Pang, H.; Lin, L.; Liu, X.; Wu, C. The Utilization of Drug–Polymer Interactions for Improving the Chemical Stability of Hot-Melt Extruded Solid Dispersions. *J. Pharm. Pharmacol.* **2014**, *66*, 285–296, doi:10.1111/jphp.12145.
124. Li, Y.; Pang, H.; Guo, Z.; Lin, L.; Dong, Y.; Li, G.; Lu, M.; Wu, C. Interactions between Drugs and Polymers Influencing Hot Melt Extrusion. *J. Pharm. Pharmacol.* **2014**, *66*, 148–166, doi:10.1111/jphp.12183.
125. Yang, Z.; Nollenberger, K.; Albers, J.; Craig, D.; Qi, S. Microstructure of an Immiscible Polymer Blend and Its Stabilization Effect on Amorphous Solid Dispersions. *Mol. Pharm.* **2013**, *10*, 2767–2780, doi:10.1021/mp400209w.
126. Donnelly, C.; Tian, Y.; Potter, C.; Jones, D.S.; Andrews, G.P. Probing the Effects of Experimental Conditions on the Character of Drug-Polymer Phase Diagrams Constructed Using Flory-Huggins Theory. *Pharm. Res.* **2015**, *32*, 167–179, doi:10.1007/s11095-014-1453-9.
127. Hempel, N.-J.; Dao, T.; Knopp, M.M.; Berthelsen, R.; Löbmann, K. The Influence of Temperature and Viscosity of Polyethylene Glycol on the Rate of Microwave-Induced In Situ Amorphization of Celecoxib. *Molecules* **2021**, *26*, 110, doi:10.3390/molecules26010110.
128. Davis, M.T.; Potter, C.B.; Walker, G.M. Downstream Processing of a Ternary Amorphous Solid Dispersion: The Impacts of Spray Drying and Hot Melt Extrusion on Powder Flow, Compression and Dissolution. *Int. J. Pharm.* **2018**, *544*, 242–253, doi:10.1016/j.ijpharm.2018.04.038.
129. Mahmah, O.; Tabbakh, R.; Kelly, A.; Paradkar, A. A Comparative Study of the Effect of Spray Drying and Hot-Melt Extrusion on the Properties of Amorphous Solid Dispersions Containing Felodipine. *J. Pharm. Pharmacol.* **2014**, *66*, 275–284, doi:10.1111/jphp.12099.

130. Wishart, D.S.; Knox, C.; Guo, A.C.; Shrivastava, S.; Hassanali, M.; Stothard, P.; Chang, Z.; Woolsey, J. DrugBank: A Comprehensive Resource for in Silico Drug Discovery and Exploration. *Nucleic Acids Res.* **2006**, *34*, D668–D672, doi:10.1093/nar/gkj067.
131. Ketoconazole: DrugBank Online. Available online: <https://go.drugbank.com/drugs/DB01026> (accessed on 28 July 2023).
132. Danazol: DrugBank Online. Available online: <https://go.drugbank.com/drugs/DB01406> (accessed on 28 July 2023).
133. Kumar, S.; Jog, R.; Shen, J.; Zolnik, B.; Sadrieh, N.; Burgess, D.J. Formulation and Performance of Danazol Nano-Crystalline Suspensions and Spray Dried Powders. *Pharm. Res.* **2015**, *32*, 1694–1703, doi:10.1007/s11095-014-1567-0.
134. Fenofibrate: DrugBank Online. Available online: <https://go.drugbank.com/drugs/DB01039> (accessed on 28 July 2023).
135. Yousaf, A.M.; Kim, D.W.; Oh, Y.-K.; Yong, C.S.; Kim, J.O.; Choi, H.-G. Enhanced Oral Bioavailability of Fenofibrate Using Polymeric Nanoparticulated Systems: Physicochemical Characterization and in Vivo Investigation. *Int. J. Nanomedicine* **2015**, *10*, 1819–1830, doi:10.2147/IJN.S78895.
136. Tadalafil: DrugBank Online. Available online: <https://go.drugbank.com/drugs/DB00820> (accessed on 28 July 2023).
137. Choi, J.-S.; Park, J.-S. Design of PVP/VA S-630 Based Tadalafil Solid Dispersion to Enhance the Dissolution Rate. *Eur. J. Pharm. Sci.* **2017**, *97*, 269–276, doi:10.1016/j.ejps.2016.11.030.
138. Celecoxib: DrugBank Online. Available online: <https://go.drugbank.com/drugs/DB00482> (accessed on 28 July 2023).
139. Ding, Z.; Wang, L.; Xing, Y.; Zhao, Y.; Wang, Z.; Han, J. Enhanced Oral Bioavailability of Celecoxib Nanocrystalline Solid Dispersion Based on Wet Media Milling Technique: Formulation, Optimization and In Vitro/In Vivo Evaluation. *Pharmaceutics* **2019**, *11*, 328, doi:10.3390/pharmaceutics11070328.
140. Efavirenz: DrugBank Online. Available online: <https://go.drugbank.com/drugs/DB00625> (accessed on 28 July 2023).
141. Cristofaletti, R.; Nair, A.; Abrahamsson, B.; Groot, D.W.; Kopp, S.; Langguth, P.; Polli, J.E.; Shah, V.P.; Dressman, J.B. Biowaiver Monographs for Immediate Release Solid Oral Dosage Forms: Efavirenz. *J. Pharm. Sci.* **2013**, *102*, 318–329, doi:10.1002/jps.23380.
142. Clotrimazole: DrugBank Online. Available online: <https://go.drugbank.com/drugs/DB00257> (accessed on 28 July 2023).
143. Madgulkar, A.; Bandivadekar, M.; Shid, T.; Rao, S. Sugars as Solid Dispersion Carrier to Improve Solubility and Dissolution of the BCS Class II Drug: Clotrimazole. *Drug Dev. Ind. Pharm.* **2016**, *42*, 28–38, doi:10.3109/03639045.2015.1024683.
144. Lopinavir: DrugBank Online. Available online: <https://go.drugbank.com/drugs/DB01601> (accessed on 28 July 2023).
145. Madgulkar, A.R.; Bhalekar, M.R.; Kadam, A.A. Improvement of Oral Bioavailability of Lopinavir Without Co-Administration of Ritonavir Using Microspheres of Thiolated Xyloglucan. *AAPS PharmSciTech* **2018**, *19*, 293–302, doi:10.1208/s12249-017-0834-x.

References

146. Liu, H.; Zhu, L.; Wang, P.; Zhang, X.; Gogos, C.G. Effects of Screw Configuration on Indomethacin Dissolution Behavior in Eudragit E PO. *Adv. Polym. Technol.* **2012**, *31*, 331–342, doi:10.1002/adv.20256.
147. Fukasawa, M.; Obara, S. Molecular Weight Determination of Hypromellose Acetate Succinate (HPMCAS) Using Size Exclusion Chromatography with a Multi-Angle Laser Light Scattering Detector. *Chem. Pharm. Bull. (Tokyo)* **2004**, *52*, 1391–1393, doi:10.1248/cpb.52.1391.
148. Friesen, D.T.; Shanker, R.; Crew, M.; Smithey, D.T.; Curatolo, W.J.; Nightingale, J.A.S. Hydroxypropyl Methylcellulose Acetate Succinate-Based Spray-Dried Dispersions: An Overview. *Mol. Pharm.* **2008**, *5*, 1003–1019, doi:10.1021/mp8000793.
149. Zecevic, D.E.; Wagner, K.G. Rational Development of Solid Dispersions via Hot-Melt Extrusion Using Screening, Material Characterization, and Numeric Simulation Tools. *J. Pharm. Sci.* **2013**, *102*, 2297–2310, doi:10.1002/jps.23592.